Field-Sweep Control in Magnetic Resonance and k-space Analysis

by

Júlia Amorós Binefa

A thesis
presented to the University of Waterloo
in fulfillment of the
thesis requirement for the degree of
Masters of Science
in
Physics (Quantum Information)

Waterloo, Ontario, Canada, 2019

Author's declaration

I hereby declare that I am the sole author of this thesis. This is a true copy of the thesis, including any required final revisions, as accepted by my examiners.

I understand that my thesis may be made electronically available to the public.

Abstract

In a general magnetic resonance experiment, resonant radiofrequency or microwave fields are applied to an ensemble of electron or nuclear spins to determine their magnetic interactions with their local environment. These interactions cause a wide range of frequencies to be present in the excitation response of the spin system. Characterizing the frequency spectrum of the response reveals detailed information about the physical and magnetic structure of the spin sample, allowing a diverse range of applications, including chemical process monitoring, molecular structure determination, imaging, and quantum information processing.

In most applications, a broadband resonator is used to excite and detect the spin response to reconstruct the spectrum in an unbiased way. Recently, however, there has been an increased interest in enhancing detection sensitivity by using narrowband (high Q) resonators. Many samples of interest have a spectral breath that exceeds the bandwidth of high Q resonators, making efficient excitation and detection of the spectrum challenging. In this thesis we propose the addition of a z-control field to perform a single-shot measurement of broad spectra. With a thorough numerical and experimental analysis, we show how sweeping the z-control during both a Hahn echo sequence and the detection of the resulting echo, allows accurate and efficient spectral reconstruction even in the presence of bandwidth limitations.

Moreover, the k-space formalism widely used in NMR and MRI is extended to describe the evolution of magnetization under the effects of any type of inhomogeneous broadening. In particular, a set of coupled recursive equations characterizing the action of soft multipulse sequences on the evolution of the magnetization is derived. We relate it to the k-space grating or reciprocal picture, and perform an order analysis of the paths. By then taking the limit of pulse length to zero, non-linear response theory is retrieved.

Acknowledgements

As these three years come to an end, I can't but feel extremely grateful to my supervisor Prof. David Cory for giving me the opportunity of joining his group, for his guidance, mentorship, and support.

I also want to thank my collaborators: Dr. Troy Borneman and Rahul Desphande. Troy, thank you for taking me under your wing the moment I arrived, for telling me it was all going to be OK, for many lengthy discussions and for proof-reading this thesis many many times. Rahul, you know I could not have done this without you. I mean it. Thank you for putting up with me, for truly listening to me and for always answering with honesty and clarity.

A heartfelt thanks goes to my lab buddy Peter Sprenger. Peter, your daily optimism, cheerfulness and passion for learning gives me hope that is possible not to grow up to be a cynic in this world. Thank you for all the help with the NMR experiments, I wouldn't have known where to start if it was not for you.

I also want to give a shout-out to my officemate Romain. I still remember how scared I was the first weeks I got to Waterloo, and how reassuring and supporting you were. We made it through this together! I will also be forever grateful to George. Thank you so much for helping me adapt into this city, for picking me up for group meetings when it was -20ºC outside, and specially for bringing Islay into our lives. And last but not least, the best fab scientist the world has ever seen: Saba! I am so glad I got to meet you before I left Waterloo. Your friendship is one of the best things that has happened to me in these three years. RAC2 would be a very sad place without you. To the rest of the Corylab group, Holger, Dima, Madelaine, Maryam, Razieh, Alex, Ian, Dusan, thank you for making me feel so welcome from the very beginning. It meant a lot.

It takes a village to make it through graduate school, and I know I would had probably lost my mind if it weren't for my family here in Waterloo. There are many people I have come to love and whose friendship I hope will stay strong even after I cross the pond: Maria, Irene, Aditya, Jeremy, Allison, Naye, Edu, Pipo, Almendra, Morgan, Stef, Sebastian, Silke, Cliff, Nachi, Arash, Nikhil, Pavel, Dainy, Abel, Vic, Alvaro, Alex, Noch (cutest dog in the

world) and many, many more! I would like to say a few words about all of you and how much your friendship means to me, but it would take too much space. I will make sure I say it in person before I move away.

Finally, I want to send an enormous hug to my family in Bell-lloc. Thank you uncle Josep, aunt Montse, Gemma, Cèlia, Ferran, Aitor, Aina i Pau, for all the love you have given me over the years. Also, to my parents, Rosaura and Josep Maria, thank you for all your support. It is so much easier to move from country to country when you know you always have a place you can call home. And last but not least, I also want to thank my lovely grandma Pilar. Grandma, I have never met a single person kinder or more generous than you. Your love inspires me everyday to be a better person. Thank you for educating, feeding and taking care of me, all the cousins, my mum and my uncle.

Dedication

To my grandma Pilar

Table of Contents

List of Figures

List of Tables

Chapter 1

Introduction

1.1 Introduction and thesis outline

Since the first measurement of a magnetic resonance signal in 1938 [1], magnetic resonance has become a widely used tool in many scientific disciplines such as chemistry, biology, material science, medicine, and quantum information.

All these fields, at some point, study a group of nearly-identical spins whose precession frequencies vary across the quantum ensemble. Such a dependence, typically manifested through a broadening of the spectra of the sample, commonly arises due to inhomogeneities in the strong magnetic field, externally applied field gradients, and/or differences in the chemical or electronic environment [2].

In quantum information processing, these variations are usually a nuisance and hence, we seek to design robust control sequences [3–5]. However, in other disciplines such as chemistry, material science or medicine, they can constitute an asset. For instance, inhomogeneous effects intrinsic to different materials can provide valuable structural and chemical information of a sample when performing spectroscopy [6]. Another example would be the introduction of artificial field gradients in Magnetic Resonance Imaging (MRI), to label different parts of the sample with different precession frequencies for the purposes of spatially-selective imaging [7].

In this thesis, we will focus on the control, detection and analysis of these types of ensembles, whose spins precess at a frequency $\delta\omega$ with an associated probability distribution.

Chapter 2 highlights the difficulties of controlling and detecting a broad spectra with a bandwidth-limited device, such as a superconducting high-Q resonator [8]. The use of this type of resonators in pulsed ESR pushes the limits of sensitivity [9], allowing for detection of progressively smaller samples, while presenting several challenges. The main obstacle tackled in this work is the bandwidth limitation of the control and detection device, which arises from its high quality factor [10, 11]. The addition of a control field perpendicular to the standard $x - y$ controls allow us to overcome this particular obstacle. In this same chapter, we present and discuss the pulse sequence we employ, as well as simulations and experiments supporting our argument.

In Chapter 3, we introduce the k-space formalism, mainly used in Nuclear Magnetic Resonance (NMR) and MRI to describe the evolution of spatially dependent magnetization in a variety of experiments. This analytical and visual description has been mostly studied for gradient fields and hard RF pulses. We make use of key tools and formulae, such as the Fourier basis decomposition of the magnetization and the k-space grating introduced by Mansfield, Hennig and others [12–14], to expand on the existing theory. We first add a z-control field into the analysis, so we can use this formalism to describe the case presented in Chapter 2. We then derive a set of coupled recursive equations characterizing the evolution of magnetization under the action of soft multipulse sequences. By taking the limit of the pulse length approaching zero and performing an order analysis of the paths in the reciprocal space, we retrieve non-linear response theory (Volterra series) for continuous and arbitrarily shaped pulses [15–17].

1.2 Mathematical Treatment of an Ensemble

Typically, magnetic resonance spectroscopy is an expectation value measurement of an ensemble of systems with quantized spin angular momentum. Examples of such systems are electron spins or the nuclei of atoms, with their resonance frequencies typically falling in the microwave and radio frequency regions, respectively. In many instances, such as in liquid-state NMR or dilute solid-state samples, these systems or molecules are taken to be non-interacting.

Thus, it is sufficiently accurate to assume we work with an ensemble of N non-interacting spins, with a Hamiltonian describing its dynamics written as

$$H_T(t) = \sum_{k=1}^{N} \mathbb{1}^{\otimes(k-1)} \otimes H_k(t) \otimes \mathbb{1}^{\otimes(N-k)} = \bigoplus_{k=1}^{N} H_k(t), \tag{1.1}$$

where $H_k(t)$ represents the Hamiltonian for the kth spin and the symbol $\oplus$ denotes the Kronecker sum.

The state of the system is characterized by a density operator $\rho(t)$, which at time $t = 0$ is assumed to have thermalized to an initial state

$$\rho_T(0) = \rho_0^{\otimes N}. \tag{1.2}$$

Time evolution of the density operator, assuming no interaction with the environment, obeys the Liouville-Von Neuman equation of motion

$$\dot{\rho}_T(t) = -i[H_T(t), \rho_T(t)], \tag{1.3}$$

whose formal solution is written as

$$\rho_T(t) = U_T(t)\rho_T(0)U_T^\dagger(t), \tag{1.4}$$

where

$$U_T(t) \equiv \mathcal{T}\left\{e^{-i\int_0^t H_T(\tau)d\tau}\right\}. \tag{1.5}$$

The symbol $\mathcal{T}$ denotes the time-ordered product of operators, an operation which we define in the appendix section A.1 and accounts for the non-commutativity of the time-dependent Hamiltonian at different times. Note that $\hbar$ has been set to one all through this thesis.

As shown in the appendix section A.2, the total evolution of the system can be factorized into the tensor product of the individual spin evolutions. Namely,

$$U_T(t) = \bigotimes_{k=1}^{N} U_k(t), \tag{1.6}$$

where $U_k(t) \equiv \mathcal{T}\left\{e^{-i\int_0^t H_k(\tau)d\tau}\right\}$ is the time-evolution operator for the kth particle. It follows that the total state of the system can also be decomposed into the individual state $\rho_k(t)$ of each particle k,

$$\rho_T(t) = \bigotimes_{k=1}^{N} \rho_k(t). \tag{1.7}$$

The traditional magnetic resonance observables $\mathcal{S}_X$, $\mathcal{S}_Y$ and $\mathcal{S}_Z$ for the whole non-interacting ensemble are also defined with respect to the individual spin operators as,

$$\mathcal{S}_i = \sum_{k=1}^{N} \mathbb{1}^{\otimes(k-1)} \otimes S_i^k \otimes \mathbb{1}^{\otimes(N-k)} = \bigoplus_{k=1}^{N} S_i, \quad \text{where } i = X, Y, \text{ or } Z. \tag{1.8}$$

It follows that the total magnetic resonance signal is the sum of the individual signals induced by each spin in the sample,

$$\langle \mathcal{S}_i \rangle(t) = \sum_{k=1}^{N} tr\left[\rho_k(t) S_i\right] = \sum_{k=1}^{N} \langle S_i \rangle_k(t). \tag{1.9}$$

The step-by-step derivation is also included in the appendix section A.2.

1.2.1 Distributions of Hamiltonian Parameters

So far, every spin in the ensemble has been labelled with an index k, highlighting that particles in the sample are distinguishable.

Indeed, it is common in magnetic resonance for phenomena such as inhomogeneities in the strong magnetic field, differences in the chemical or electronic environment, and/or artificially applied gradients to cause parameters in the internal Hamiltonian to vary over the ensemble, thus effectively labeling each spin in frequency,

$$H_k(t) = H_{int_k} + H_{contr}(t). \tag{1.10}$$

The variation of the parameters of the internal Hamiltonian over the sample is, in most cases, a continuous function acting on a large ensemble of the order of $\sim 10^{10} - 10^{20}$ particles. For these reasons, we drop the discrete label $()_k$ and write

$$H_k(t) \quad \longrightarrow \quad H(t;\delta\omega) = H_{int}(\delta\omega) + H_{contr}(t) \tag{1.11}$$

to denote that the internal Hamiltonian (and hence the total Hamiltonian) is conditional on a parameter $\delta\omega$. It follows that the time-evolution as well as the state of each particle also depend on the continuous variable $\delta\omega$,

$$\begin{aligned} U_k(t) \quad &\longrightarrow \quad U(t;\delta\omega) \\ \rho_k(t) \quad &\longrightarrow \quad \rho(t;\delta\omega) \end{aligned}$$

To model the experimental distribution introduced by the phenomena described above, we parametrize the variable $\delta\omega$ with an associated probability density function $p(\delta\omega)$. This $p(\delta\omega)$ is physically understood as the spectrum of the sample.

The spectrum of a sample is retrieved from the detected signal $\langle \mathcal{S}_+ \rangle(t) = \langle \mathcal{S}_X \rangle(t) + i\,\langle \mathcal{S}_Y \rangle(t)$ by taking its Fourier Transform. Namely,

$$p(\delta\omega) \equiv \mathcal{W}(\delta\omega) = \mathcal{F}\Big\{\, \langle \mathcal{S}_X \rangle(t) + i\,\langle \mathcal{S}_Y \rangle(t) \Big\}. \tag{1.12}$$

Accordingly, the expected values for the observables as well as the state of the system are obtained by averaging over the distribution $p(\delta\omega)$,

$$\langle \mathcal{S}_i \rangle(t) = \int p(\delta\omega)\,\mathrm{Tr}\left[\rho(t;\delta\omega) S_i\right]\,\mathrm{d}\delta\omega = \int p(\delta\omega)\,\langle S_i \rangle(t;\delta\omega)\,\mathrm{d}\delta\omega, \tag{1.13}$$

and,

$$\rho(t) = \int p(\delta\omega)\,U(t;\delta\omega)\rho_0 U^\dagger(t;\delta\omega)\,\mathrm{d}\delta\omega \tag{1.14}$$

Hence, the problem of controlling and detecting a non-interacting spin-1/2 ensemble under the effects of inhomogeneous broadening, is equivalent to the problem of manipulating a single spin-1/2 whose internal Hamiltonian depends on a parameter $\delta\omega$ associated to a probability density function $p(\delta\omega)$.

1.3 Fundamentals of Quantum Mechanics for a Single Spin in Magnetic Resonance

1.3.1 Hamiltonians

In magnetic resonance, a large and static magnetic field $\mathbf{B}_0$ polarizes the sample and sets the quantization axis along the direction of $\mathbf{B}_0$, commonly taken to define the z-axis. The interaction energy of this field with each spin in the sample is given by the Zeeman Hamiltonian

$$H_0 = -\boldsymbol{\mu}\ \mathbf{B}_0 = -\gamma B_0 S_Z, \tag{1.15}$$

where S_Z represents the spin angular momentum operator along the z direction and γ is the gyromagnetic ratio. For the case of a spin-1/2, the representation of operators S_X, S_Y, and S_Z is given by the Pauli matrices

$$S_X = \frac{1}{2}\sigma_X = \frac{1}{2}\begin{pmatrix} 0 & 1 \\ 1 & 0 \end{pmatrix}, \quad S_Y = \frac{1}{2}\sigma_Y = \frac{1}{2}\begin{pmatrix} 0 & -i \\ i & 0 \end{pmatrix}, \quad \text{and} \quad S_Z = \frac{1}{2}\sigma_Z = \frac{1}{2}\begin{pmatrix} 1 & 0 \\ 0 & -1 \end{pmatrix}. \tag{1.16}$$

Then, the Zeeman Hamiltonian becomes

$$H_0 = \frac{1}{2}\omega_0\ \sigma_Z, \tag{1.17}$$

where $\omega_0 = -\gamma B_0$.

To manipulate the state of the spins, a small oscillating magnetic field $p_X(t)$ is applied in the plane transverse to the quantizing field $\mathbf{B}_0$, in an orthogonal direction labeled as $\hat{x}$. A resonant circuit applies this control pulse and also picks up the response signal generated by the precessing spins: $\langle \mathcal{S}_+ \rangle = \langle \mathcal{S}_X \rangle + i \langle \mathcal{S}_Y \rangle$. The interaction of this field with a single spin is given by the control Hamiltonian

$$H_{contr} = p_X(t)\ S_X. \tag{1.18}$$

The field $p_X(t)$ is generally a linearly oscillating function in the lab frame,

$$p_X(t) = 2\omega_1(t)\cos\left(\omega_t t + \phi(t)\right), \tag{1.19}$$

where ω_t is the transmitter frequency and $\omega_1(t) = \gamma B_1(t)$. Since the frequency ω_t is typically very high and we are not interested in dynamics at this scale, it is convenient to do a transformation to a rotating frame. The details of going into the rotating frame of ω_t and performing a rotating wave approximation can be found in the appendix section A.3. The resulting Hamiltonian for the case of a spin-1/2 is,

$$H^R(t;\delta\omega) = H^R_{int}(\delta\omega) + H^R_{contr}(t), \tag{1.20}$$

which has an internal term

$$H^R_{int}(\delta\omega) = \frac{1}{2}\delta\omega\ \sigma_Z, \tag{1.21}$$

where $\delta\omega = \omega_0 - \omega_t$, and also a control term

$$H^R_{contr}(t) = \frac{1}{2}\omega_1(t)\cos\phi(t)\ \sigma_X + \frac{1}{2}\omega_1(t)\sin\phi(t)\ \sigma_Y = \sum_{j=1}^{2} p^R_j(t) S_j. \tag{1.22}$$

From now on, we will only work in the rotating frame of ω_t and thus, it is not necessary to keep the notation $(\cdot)^R$.

1.3.2 Thermal initial state

At equilibrium, the state of an ensemble of spins 1/2 at a temperature T and in the presence of a static field $B_0\hat{z}$ is given by a Boltzmann distribution. Namely,

$$\rho_T(0) = \frac{e^{-\beta H_0}}{\mathcal{Z}} = \frac{1}{\mathcal{Z}}\bigotimes_{k=1}^{N} e^{-\beta\omega_0 S_Z} = \rho_0^{\otimes N}, \tag{1.23}$$

where H_0 is the Zeeman Hamiltonian $H_0 = \bigoplus_{k=1}^{N}\omega_0 S_Z$. The partition function is

$$\mathcal{Z} = \mathrm{Tr}\,(e^{-\beta H_0}) = \prod_{k=1}^{N}\mathrm{Tr}\,e^{-\beta\omega_0 S_Z}, \tag{1.24}$$

where the coefficient β is the Boltzmann constant $\beta = \frac{1}{k_b T}$ and k_0 the normalization constant.

In a typical NMR experiment with a Zeeman frequency of $\omega_0 = 400$ MHz and a temperature of $T = 300$K, the factor $\beta\omega_0$ is of the order of 10^{-4}. It is valid to then take the approximation,

$$\rho_0 = \frac{1}{\mathcal{Z}}e^{-\beta\omega_0 S_Z} \approx \frac{1}{2}(\mathbb{1} + \epsilon_0\sigma_Z) \tag{1.25}$$

where $\epsilon_0 = \beta\omega_0$ [18].

1.3.3 Ensemble Measurement Operators

As stated in section 1.3.1, in a typical magnetic resonance setup, the pick-up coil transverse to the Zeeman field $\mathbf{B}_0$ generates the control fields as well as detects the response signal from the spins. Classically, this response signal is referred as the magnetization $\mathbf{M}(t)$, whose precession induces a voltage in the coil

$$\varepsilon = -N\frac{d\phi}{dt} = -N\frac{d}{dt}\int_V \mathbf{M}\cdot\left(\frac{\mathbf{B}_1}{i_1}\right)dV, \tag{1.26}$$

where the integration is weighted by the normalized field $\mathbf{B}_1/i_1$ [19].

In the semi-classical approach followed in this thesis, the spin ensemble is treated quantum mechanically and the coil classically. The magnetization $\mathbf{M}(t) = (M_X(t), M_Y(t), M_Z(t))$ is defined as the expected value of the collective spin angular momentum operators $\mathcal{S}_X$, $\mathcal{S}_Y$ and $\mathcal{S}_Z$,

$$M_X(t) = \langle\mathcal{S}_X\rangle(t), \qquad M_Y(t) = \langle\mathcal{S}_Y\rangle(t), \qquad \text{and} \qquad M_Z(t) = M_{long}(t) = \langle\mathcal{S}_Z\rangle(t). \tag{1.27}$$

Thus, for the case of an ensemble of non-interacting spins 1/2, the detected transverse magnetization is,

$$M_{trans}(t) = \langle\mathcal{S}_X\rangle(t) + i\,\langle\mathcal{S}_Y\rangle(t) = \int p(\delta\omega)\,\mathrm{Tr}\left[U(t;\delta\omega)\rho_0 U^\dagger(t;\delta\omega)(S_X + iS_Y)\right]\,\mathrm{d}\delta\omega. \tag{1.28}$$

1.3.4 Numerical simulation of the time-evolution of the observables.

In order to study the dynamics of a single spin under the action of different time-continuous pulses $\mathbf{p}(t) = (p_X(t), p_Y(t), p_Z(t))$, we need to solve

$$U(t;\delta\omega) = \mathcal{T}\left\{e^{-i\int_0^t H(\tau;\delta\omega)d\tau}\right\}. \tag{1.29}$$

Doing so analytically is often impossible, unless $H(t;\delta\omega)$ is a time-independent function. To compute the unitary evolution for time-dependent pulses, we can resort to time-slicing.

For each isochromat $\boldsymbol{\delta\omega}$, time is discretized in slices of $\Delta t = t/n$. For small enough Δt, we can safely assume control amplitudes $p_X(t), p_Y(t)$ and $p_Z(t)$ to be constant at each time-step such that they become discrete functions $p_X[n]$, $p_Y[n]$, and $p_Z[n]$.

This approximation allows us to avoid the computation of time-ordered exponentials by writing the time evolution propagator at each step n as,

$$U[n,m] = \exp\left(-\frac{i\Delta t}{2}\left(m\Delta\Omega\;\sigma_Z + \sum_{i=1}^{3} p_i[n]\;\sigma_i\right)\right), \tag{1.30}$$

where we have also discretized the spectrum $p(\delta\omega) \to p[m]$, with $\delta\omega = m\Delta\Omega$.

The discrete time evolution for each isochromat m then becomes,

$$\rho[n,m] = U[n,m]\ldots U[1,m]\ \rho_0\ U^\dagger[1,m]\ldots U^\dagger[n,m]. \tag{1.31}$$

such that the time evolution averaged over the ensemble, for each observable S_X, S_Y and S_Z, is

$$\langle S_i\rangle[n] = \sum_{m=-M}^{M} p[m]\ \mathrm{Tr}\left(\frac{1}{2}\rho[n,m]\sigma_i\right), \tag{1.32}$$

for $i = X, Y, Z$ and $M = \delta\omega_{max}/\Delta\Omega$.

The software of choice in this thesis was *Mathematica 11*, and the simulations were run using the package *Quantum Utils* [20].

1.4 Relaxation times T_1, T_2 and T_2^*

The decay of a magnetic resonance signal is generally described in terms of three relaxation constants, T_1, T_2 and T_2^*.

Both T_1 and T_2 are intrinsic properties of the sample and depend on the lattice structure and local environment. The relaxation constant T_1 is responsible for the magnetization decay to thermal equilibrium due to various relaxation mechanisms where spins exchange energy with their environment (for this reason it is also known as spin-lattice relaxation) [2, 18]. On the other hand, T_2 can be phenomenologically understood as the rate of decay of the transverse magnetization. Possible mechanisms triggering this decay can be random local fluctuations of the magnetic field that lead to a loss in phase coherence of the spins, and in turn, a broadening of the spectrum [2, 18].

External factors such as inhomogeneities in the magnetic field or differences in the chemical environment of the spins also contribute to signal decay due to apparent dephasing: each particle in the sample experiences a different field and thus, a different Larmor frequency. This difference translates into a dispersion of the magnetic vector phase of each spin, such that when averaging over the ensemble, the net result is the disappearance of the transverse magnetization. The time constant T_2^* describes this phenomena,

$$\frac{1}{T_2^*} = \frac{1}{T_2} + \frac{1}{T_{2\,inhom}}. \tag{1.33}$$

As with T_2, it causes the spectra of the sample to broaden [2]. Note that it is not a "true" relaxation mechanism *per se*, since the signal can be recovered by performing a spin-echo experiment.

1.5 Spin echo

As explained in section 1.4, the signal induced by a spin ensemble after applying an excitation pulse decays mainly due to two reasons: spin relaxation and inhomogeneous effects. Inhomogeneous broadening, unlike broadening due to intrinsic T_2 (homogeneous) effects, can be refocused by a Hahn echo experiment [21], as depicted in figure 1.1.

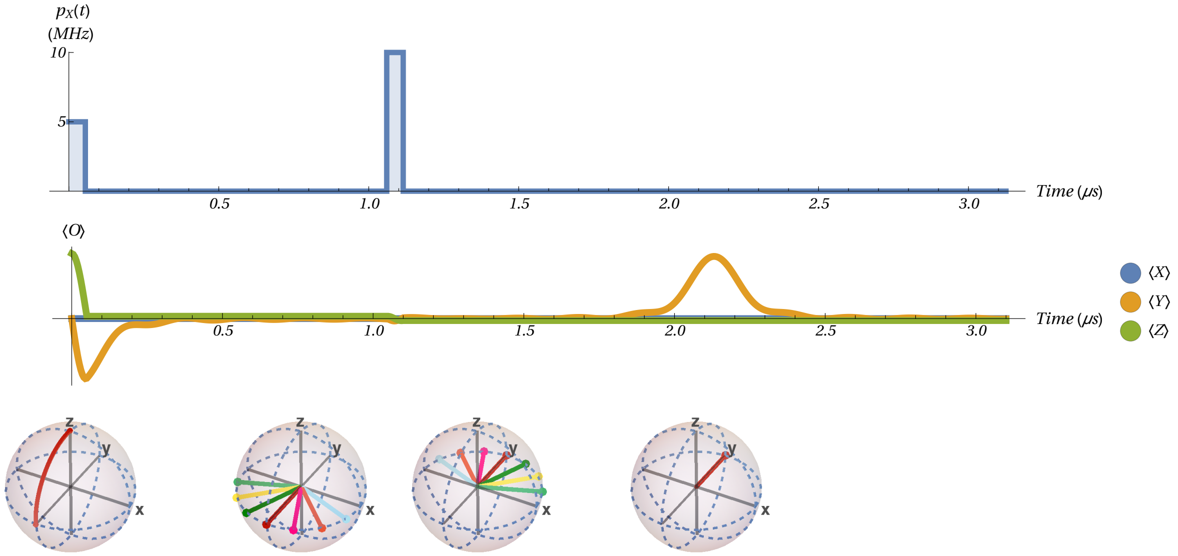

Figure 1.1: In this figure we show the pulse profile $p_X(t)$ applied along x, the corresponding observable evolution $\langle O\rangle(t)$ and some Bloch plots depicting how the isochromats are affected by the internal and control Hamiltonians at different times in the pulse sequence.

Generally, since the initial state of the magnetization is along the z axis and detection occurs in the transverse plane, we first need to bring the magnetization vector to this plane by applying a $\pi/2$ pulse along either the $\hat{x}$ or $\hat{y}$ axis. Once the magnetization vector has been tipped away from the $\hat{z}$ axis, each isochromat starts to precess at a different frequency due to the inhomogeneities, inducing phase dispersion between the magnetization vector of each isochromat. The response signal begins to decay, since it is an average of dephased magnetization vectors. If after a time τ of inhomogeneous evolution we apply a π pulse, the time evolution is effectively inverted, allowing the magnetization phases to refocus at time 2τ, creating an echo of the free induction decay.

For samples with a particularly broad inhomogeneous spectrum (i.e. $T_2^* \ll T_2$), such as the ones of interest to this work, it is common to perform echo detection instead of direct detection of the free induction decay.

Chapter 2

Bandwidth-limited control and detection

2.1 Introduction

Electron spin resonance (ESR) is widely used in chemistry and biology to detect and characterize paramagnetic samples [22]. It has also recently served as an important test-bed for control in quantum information processing [23–25]. Both ESR and other spectroscopic techniques, such as nuclear magnetic resonance (NMR), rely on inductive coupling of a resonator circuit to a spin ensemble for control and detection of its magnetic response [2]. In particular, pulsed ESR spectroscopy probes a sample coupled to a resonator by applying a series of microwave pulses that induce a spin response in the form of a free induction decay or a spin-echo [26]. From either of these signals, the dynamics and spectra of the sample can be extracted.

Given recent advances in nanofabrication, it is becoming common to substitute traditional ESR cavities with high-Q cavities, such as superconducting thin-film resonators [8, 27, 28]. Employing such a resonator for control and detection increases the signal-to-noise ratio (SNR), improving measurement sensitivity [9].

However, the use of such resonators presents an inherent challenge: a limited bandwidth to control and detect the sample due to the inverse relation between the Q factor and the resonator bandwidth (BW). There are two direct consequences:

1. First, the pulses we apply to the sample through the resonator are effectively filtered. This distortion can be modelled as a convolution of a kernel $h(t) = \mathcal{L}^{-1}\{H(s)\}$ with pulses $p_X(t)$ and $p_Y(t)$. The filter $H(s)$ alters the shape of the pulses by acting as a band-pass filter to the pulse frequency components, making it difficult to uniformly

control a broad spectrum without optimization. Even if an optimal pulse sequence is found, the narrow bandwidth will always limit the efficiency that can be achieved with our control.

2. Second, often the spectrum of spin species we aim to measure has a linewidth broader than the bandwidth of the high-Q resonator. Hence, the resonator filters out part of the signal we are aiming to measure in such a way that only a portion of the spectra can be recovered with a single measurement.

Both points lead to one conclusion: the whole sample spectrum cannot be reconstructed in a one-shot spin-echo experiment using only two control pulses $p_X(t)$ and $p_Y(t)$ applied through the resonator.

To analyze how the resonator impulse response affects the control pulses, we model the cavity as a RLC circuit [29, 30]. The solution for the impulse response is an exponential function with a time constant $\tau_c = 2Q/\omega_0$. The convolution of the control pulses with the impulse response of the RLC circuit results in a set of distorted control pulses. If the modelling is done correctly, the shape of these distorted pulses will match the fields the spins are expected to experience.

This pulse distortion can be overcome by using Optimal Control Theory (OCT) to engineer robust time-dependent pulses, also known as shaped pulses [10, 11, 31–33]. OCT algorithms, such as GRAPE [34], optimize over an initial pulse guess constrained by experimental parameters and functions – for instance, the transfer function of the cavity – to find an unitary that matches the target for every spin in the sample. However, when the requirements of low power, narrow bandwidth and uniform behavior over a broad spectra are included into the optimization, obtaining the same target unitary for every spin becomes increasingly difficult.

However, an optimization of x, y-controls cannot be used to overcome the filtering of the magnetic resonance signal by the resonator, for the simple reason that no x, y-control pulses can be applied during detection. In this chapter, we put forward a practical solution to this problem and support our argument with simulations in the context of ESR and experimental data obtained using an NMR system.

Since it is challenging and inefficient for OCT – given the power and bandwidth limitations – to find broad pulses when restricting the control to two components $\mathbf{p}(t) = (p_X(t), p_Y(t), 0)$, and altogether not useful when it comes to overcome the filtering of the signal by the resonator, we propose the addition of an extra control field $p_Z(t)$, i.e.,

$\mathbf{p}(t) = (p_X(t), p_Y(t), p_Z(t))$. The introduction of this extra degree of freedom in our control allows us to both broadly excite as well as detect the entire spectrum efficiently in a single-shot experiment.

The proposed solution first tackles the efficient excitation of the broad spectrum. To do so, two linear z-field sweeps are applied simultaneous to the excitation and refocusing pulses of a standard echo sequence. The linear sweeps force different parts of the spectrum to refocus at different times, generating a chirped echo instead of the traditional Hahn echo [35–37]. To then address the filtering of the magnetic resonance signal by the resonator, a third sweep is applied while the chirped echo forms. By slowly sweeping the z-field, different parts of the spectra are progressively brought into resonance with the cavity so they can be detected. The resulting echo has a Fourier Transform (FT) narrower than the transfer function of the cavity, enabling us to recover the spectrum after following some post-processing steps.

2.2 Simulations

In this section, we discuss the simulation of an ensemble of non-interacting spin-1/2 controlled by a high-Q resonator and subjected to a distribution of Zeeman Hamiltonians, whose parameter $\delta\omega$ is associated to a probability density function $p(\delta\omega)$.

We feed into our simulations a pulse sequence $\mathbf{p}(t)$ of our choice and the spectrum of the sample, $p(\delta\omega)$. The simulation output is the time evolution of the expected values of the observables S_X, S_Y, and S_Z.

The section is structured as follows: first, we present the input spectra, the pulses, and the distortion effects the control hardware has on the pulses. Then, we show the simulation outputs $\langle \mathcal{S}_X \rangle(t)$, $\langle \mathcal{S}_Y \rangle(t)$ and $\langle \mathcal{S}_Z \rangle(t)$ for both the cases of bandwidth-limited control and detection.

2.2.1 Input spectra or probability density functions

Simulation results for two different spectra $p(\delta\omega)$ will be presented in this thesis. The first one, displayed in figure 2.1 (a), corresponds to a simple Lorentzian lineshape centered around $\delta\omega = 0$, and with a full-width at half-maximum (FWHM) of 4 MHz. The second spectrum, presented in figure 2.1 (b), is a Pake pattern commonly observed in powder or glass samples arising from dipolar couplings. The dipolar coupling frequency is $\omega_{DD} = 2.29$

MHz, corresponding to a rigid biradical with nitroxide endgroups [38], commonly used to calibrate distance measurements for biological ESR [26].

The frequency simulation range for both spectra is $-\delta\omega_{max} < \delta\omega < \delta\omega_{max}$, where $\delta\omega_{max} = 5$ MHz.

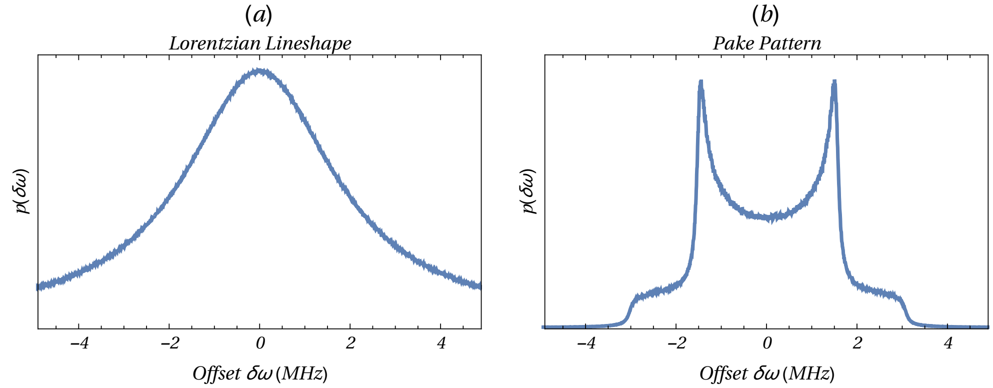

Figure 2.1: Probability density function $p(\delta\omega)$ for two different types of spectra: (a) a simple Lorentzian lineshape with a FWHM of 4 MHz and centered around $\delta\omega = 0$, and (b) a Pake pattern arising from a distribution of dipolar couplings in powder or glass samples. The vertical coordinates are proportional to the magnetization of the sample by a factor that can be calibrated using a standard.

2.2.2 Simulation parameters

The internal Hamiltonian, as described in section 1, is given by a Zeeman interaction,

$$H_{int} = \frac{1}{2}\delta\omega\sigma_Z, \tag{2.1}$$

where $\delta\omega$ is a parameter associated to $p(\delta\omega)$. To manipulate the state of our spin we employ a control Hamiltonian

$$H_{contr} = \frac{1}{2}\sum_{i=1}^{3} p_i(t)\ \sigma_i, \tag{2.2}$$

where $\mathbf{p}(t) = (p_1(t), p_2(t), p_3(t)) = (p_X(t), p_Y(t), p_Z(t))$ and $\boldsymbol{\sigma}$ is the Pauli vector $\boldsymbol{\sigma} = (\sigma_1, \sigma_2, \sigma_3) = (\sigma_X, \sigma_Y, \sigma_Z)$.

Two types of pulse sequences $\mathbf{p}(t)$ will be simulated, as shown in figure 2.2.

The sequence sketched in figure 2.2 (a) consists of two pulses, $p_X(t)$ and $p_Z(t)$. Without loss of generality, we consider $p_Y(t) = 0\ \forall\ t$. The pulse $p_X(t)$ is made up of two constant-amplitude pulses of length $t_p = 15\ \mu s$ and Rabi $\Omega_{\pi/2} = 0.25$ MHz and $\Omega_\pi = 0.5$ MHz, both applied along x with a time separation of $\tau_X = 17.5\ \mu s$. The pulse $p_Z(t)$ consists of two sweeps, with length $t_s = 20\ \mu s$, range $2\Delta\omega_s = 20$ MHz and separated from each other by a time $\tau_Z = 12.5\ \mu s$. The start of $p_X(t)$ is delayed with respect to $p_Z(t)$ by $2.5\ \mu s$, to center the sweeps with their corresponding rectangular pulses $\Omega_{\pi/2}$ and Ω_π. This type of sequence generates a chirped echo that extends from time $t_i = 2t_s + 2\tau_Z = 65\ \mu s$ to $t_f = 3t_s + 2\tau_Z = 85\ \mu s$ (not depicted in figure 2.2).

The pulse sequence shown in figure 2.2 (b) is identical to (a) with the exception of a third linear z-sweep from t_i to t_f. Matching this third sweep with the formation of the chirped echo enables us to overcome the filtering of the echo by the resonator.

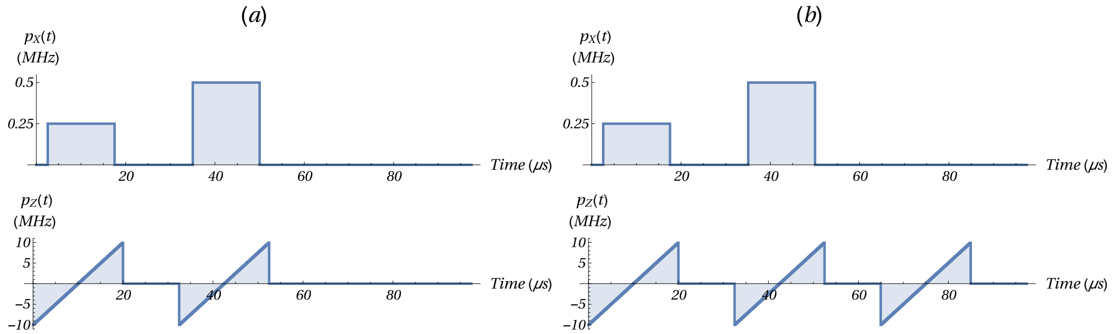

Figure 2.2: Both subplots (a) and (b) show two rectangular pulses $\Omega_{\pi/2}$ and Ω_π of length $t_p = 15\ \mu s$ applied while sweeping the z-field for a time $t_s = 20\ \mu s$. In (b), a third field sweep is added between time $t_i = 65\ \mu s$ and $t_f = 85\ \mu s$.

2.2.3 Pulse distortion

As stated in the introduction, a high-Q superconducting resonator in the linear regime can be approximately modelled as a simple RLC circuit, such as the one in figure 2.3.

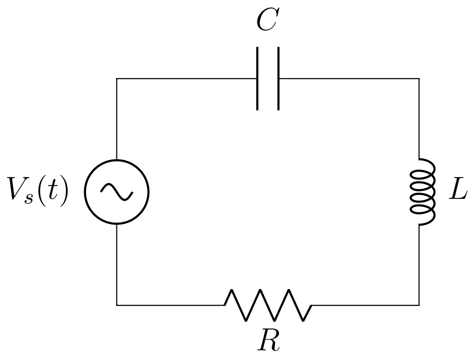

Figure 2.3: Series RLC circuit for modelling resonator transients in the linear regime.

Standard methods of transient analysis in linear circuits give us the transfer function $H(s)$ for a series RLC circuit,

$$H(s) = \frac{s}{Ls^2 + Rs + 1/C}, \tag{2.3}$$

which relates the input $V_s(t)$ to the output $I(t) \propto B_1(t)$,

$$I(s) = H(s)V_s(s). \tag{2.4}$$

We are interested in the input/output relation between the voltage $V_s(t)$ and the current in the inductor $I(t)$, since the current is proportional to the control field $B_1(t) = \gamma(p_X(t), p_Y(t))$, which governs the spin dynamics.

By taking the inverse Laplace transform, we obtain the exact form for the impulse response function $h(t) = \mathcal{L}^{-1}\{H(s)\}$,

$$h(t) = \frac{1}{L} e^{-\frac{R}{2L}t} \left\{ \cosh\left(\frac{\sqrt{-4L + R^2C}}{2L\sqrt{C}}\, t \right) - \frac{R\sqrt{C}}{\sqrt{-4L + R^2C}} \sinh\left(\frac{\sqrt{-4L + R^2C}}{2L\sqrt{C}}\, t \right) \right\}. \tag{2.5}$$

In a series RLC circuit, the variables R, L and C relate to the quality factor Q and the resonance frequency ω_c as

$$Q = \frac{1}{R}\sqrt{\frac{L}{C}} \qquad \text{and} \qquad \omega_c = \frac{1}{\sqrt{LC}}. \tag{2.6}$$

Keeping these relations in mind, we can simplify the impulse response in 2.5 by considering the quality factor Q to be very large ($Q \gg 1$), as is the case for high Q resonators (generally, $Q > 10^3$.

First, the argument in the hyperbolic cosine and sine of 2.5 becomes,

$$\frac{\sqrt{-4L + R^2C}}{2L\sqrt{C}}\, t = \frac{1}{2\sqrt{LC}}\sqrt{-4 + \frac{R^2C}{L}}\, t = \frac{\omega_c}{2}\sqrt{-4 + \frac{1}{Q^2}}\, t \approx \frac{\omega_c}{2} 2i\, t = i\omega_c t. \tag{2.7}$$

Secondly, the factor

$$\frac{R\sqrt{C}}{\sqrt{-4L + R^2C}} = \frac{R}{2L}\frac{2L\sqrt{C}}{\sqrt{-4L + R^2C}} \approx -i\frac{R}{L}\frac{1}{2\omega_c} = -i\frac{\omega_c}{Q}\frac{1}{2\omega_c} = -i\frac{1}{2Q} \tag{2.8}$$

can also be approximated to a simple expression in the limit of high Q. Therefore, equation 2.5 is reduced to

$$h(t) = \frac{1}{L} e^{-\frac{R}{2L}t} \big(\cos\omega_c t + \frac{1}{2Q} i \sin\omega_c t \big) \approx \frac{1}{L} e^{-\frac{R}{2L}t} \cos\omega_c t \tag{2.9}$$

Last, we set the transmitter frequency to match the natural resonance frequency of the RLC circuit, $\omega_t = \omega_c$. Since all our pulse analysis is performed in the rotating frame of ω_t, the circuit also has to be in the same frame. After moving to the rotating frame of ω_t and performing a standard rotating wave approximation, the impulse response becomes,

$$h^R(t) = h(t) e^{-i\omega_t t} \overset{r.w.a}{=} \frac{1}{L} e^{-\frac{R}{2L}t} \propto e^{-t/\tau_c} \tag{2.10}$$

where $\tau_c = \frac{2L}{R} = \frac{2Q}{\omega_c} = \frac{Q}{\pi f_c} = \frac{1}{\pi BW}$. As with previous rotating frame analysis, we drop the label $(\cdot)^R$ and assume all impulse responses from now on are in the rotating frame of the transmitter frequency.

It follows that the distorted pulse $\tilde{p}_X(t)$ is a simple convolution of the ideal pulse, $p_x(t)$, with the kernel, $h(t)$:

$$\tilde{p}_X(t) = p_X(t) * h(t) = p_X(t) * e^{-t/\tau_c}. \tag{2.11}$$

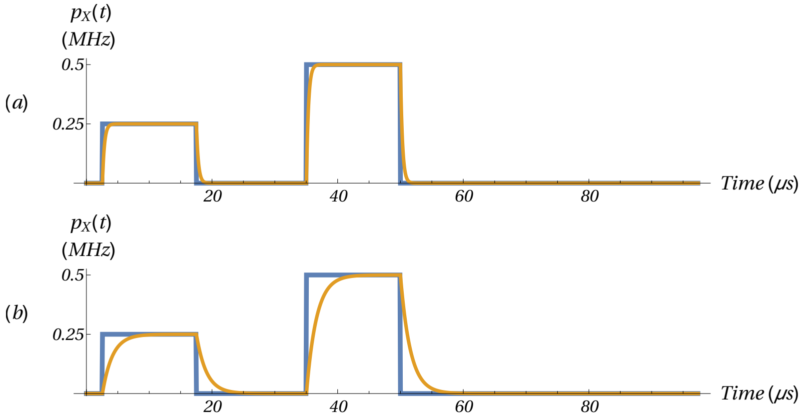

Figure 2.4: Distorted pulse (yellow) superimposed over the non-distorted pulse (blue), for a resonator with (a) Q = 10000, and (b) Q = 50000.

For $f_c = 10$ GHz and two different values for the quality factor of $Q = 10000$ and $Q = 50000$, the resulting distorted field pulse $\tilde{p}_X(t)$ is depicted in figure 2.4 together with its undistorted input voltage pulse $p_X(t)$.

In all remaining simulations presented in this chapter, the chosen quality factor is $Q = 10000$, with a corresponding bandwidth of $BW = 1$ MHz at 10 GHz (due to the prevalence of the X-band).

2.2.4 Discussion of the choice of pulse sequence parameters

The choice of the following parameters:

1. Rabi frequencies $\Omega_{\pi/2}$ and $\Omega_\pi = 2\Omega_{\pi/2}$.
2. Pulse length t_p.
3. Sweep length t_s.
4. Separation times τ_X and τ_Z.

5. Sweep width $\Delta\omega_s$.

are determined by:

1. Relaxation times T_1 and T_2.
2. Width of the spectra to recover, $\delta\omega_{max}$.
3. Control bandwidth BW, or equivalently τ_C.
4. Power limitation Ω_{max} to stay in the linear regime.

Any transient effects, such as the ones presented in section 2.2.3, are unwanted deviations from an ideal pulse sequence that can distort a spectrum when attempting to reconstruct it. Therefore, it is extremely important to design control pulses robust to any kind of transients in the spectral range $\delta\omega \in [-\delta\omega_{max}, \delta\omega_{max}]$. A way to ensure so, is to move significantly off-resonance (i.e., $|\delta\omega| \gg |\delta\omega_{max}|$) whenever transient effects are more pronounced.

Along these lines, we choose a sweep width double the spectral range: $2\Delta\omega_s = 4\delta\omega_{max}$ and a sweep length larger than the pulse length $t_s > t_p$ (in particular, $t_s = \frac{4}{3}t_p$). Additionally, we want the transient effects to have saturated when we start pulsing. Therefore, t_p has to be sufficiently long given a bandwidth of $1MHz$. For this thesis, t_p has been set to $15\mu s$ and t_s to $20\mu s$.

To simplify the analysis, we choose to remain in the linear regime. To do so, we limit the x-control amplitude to $\Omega_{max} = \delta\omega_{max}/10 = 0.5$ MHz, such that $\Omega_\pi = \Omega_{max} = 0.5$ MHz and $\Omega_{\pi/2} = \Omega_\pi/2 = 0.25$ MHz.

Pulse separation times τ_X and τ_Z are chosen to ensure that the center of the sweep matches the center of the pulses, as stated in section **??**.

Last but not least, we must satisfy the constraint that

$$3(t_p + \tau_X) = 3(t_s + \tau_Z) < T_2, \tag{2.12}$$

while still maximizing the overall length of the pulses. In this thesis, we have chosen the values for t_p, t_s, τ_X, and τ_Z assuming a T_2 of tens of μs, which has been shown for a variety of samples.

2.3 Simulations results and discussion

In this section we present the reconstruction of the two spectra $p(\delta\omega)$ of figure 2.1, a Lorentzian lineshape and a Pake pattern.

Before we continue, a few things should be noted. First, the convention for figures with two subplots (a) and (b), is that subplot (a) always shows results related to the Lorentzian lineshape of figure 2.1 (a) and subplot (b) presents results for the Pake pattern of figure 2.1 (b). Second, when referring to frequencies in units of Hz, commonly denoted as $\omega/(2\pi)$, we drop the 2π notation for convenience.

2.3.1 Bandwidth-limited control

In figure 2.5 we show a set of distorted pulses $\mathbf{p}(t) = \big(p_X(t), 0, p_Z(t)\big)$ together with their corresponding simulated observables $\langle \mathbf{O} \rangle(t) = \big(\langle S_X\rangle(t), \langle S_Y\rangle(t), \langle S_Z\rangle(t)\big)$, for a Lorentzian lineshape and a Pake pattern.

The pulse $p_X(t)$ has been distorted by convolving the original rectangular pulses $\Omega_{\pi/2}$ and Ω_π with the transfer function of an RLC circuit with a quality factor of $Q = 10000$. To implement the sweep we can either vary the resonant frequency ω_c of the cavity or use a dedicated coil that applies a z-field. Note that such a field would not be affected by a high-Q exponential distortion, since it is applied with a different device.

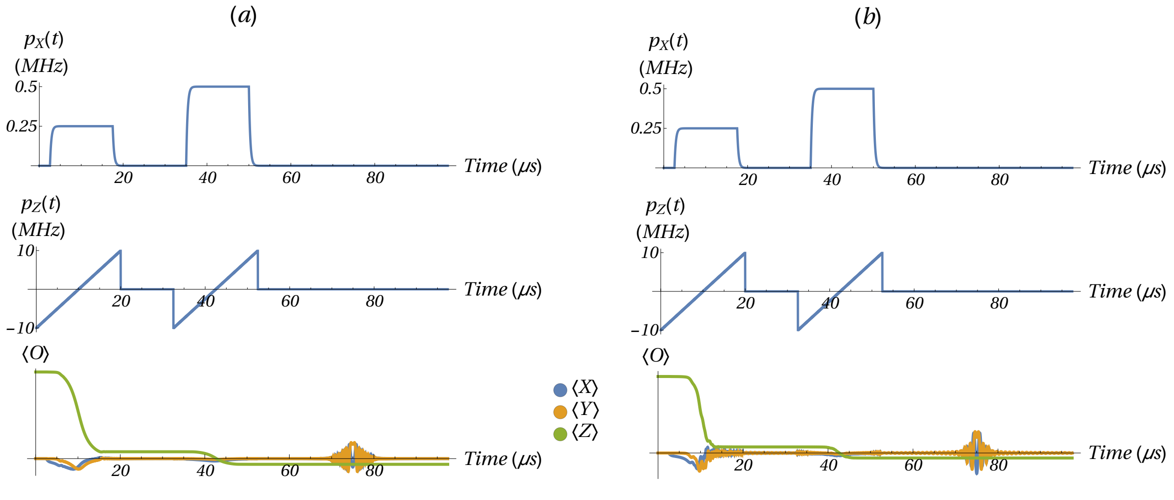

Figure 2.5: From top to bottom, $p_X(t)$, $p_Z(t)$ and $\langle S_X\rangle(t)$, $\langle S_Y\rangle(t)$ and $\langle S_Z\rangle(t)$, in (a) for the Lorentzian lineshape and in (b) for the Pake pattern.

By sweeping the field during the excitation and refocusing pulses of the echo sequence, we address the first issue imposed by the use of high Q resonators and the limited Rabi drive strength of our x, y-control: the inability to **broadly excite and refocus** all the isochromats in our sample efficiently. By slowly sweeping the z-field while pulsing, we consecutively refocus different parts of the spectra, forming a frequency-modulated signal known as chirped echo, containing all the required spectral information. In figure 2.6, we zoom into the echoes $\langle S_X^{CH}\rangle(t)$ and $\langle S_Y^{CH}\rangle(t)$ of figure 2.5 between times t_i and t_f to better appreciate the structure of the chirped echoes: a frequency modulated signal whose envelope is dictated by the form of the input spectra, $p(\delta\omega)$.

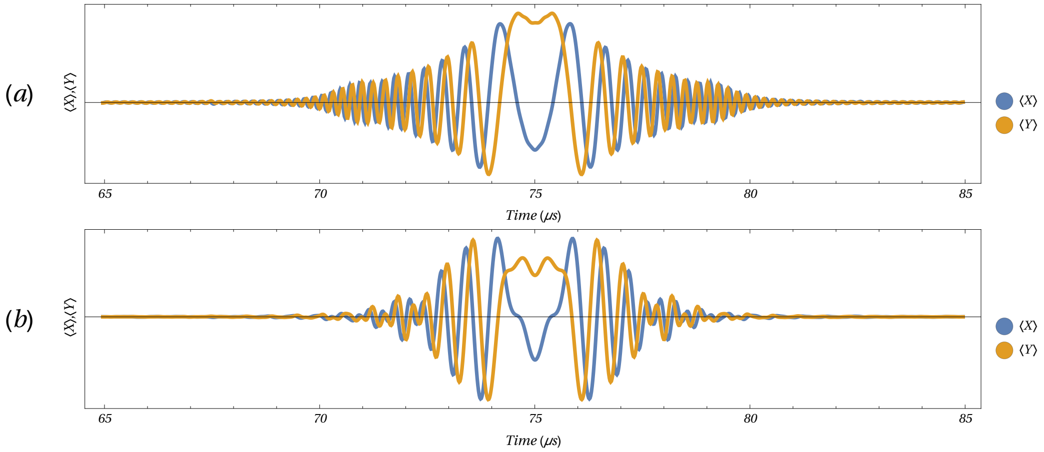

Figure 2.6: Signal $\langle S_X^{CH}\rangle(t)$ (blue) and $\langle S_Y^{CH}\rangle(t)$ (yellow) for a Lorentzian lineshape in (a), and a Pake pattern (b).

By taking the complex Fourier Transform (FT) of the chirped echoes $\langle S_X^{CH}\rangle(t)$ and $\langle S_Y^{CH}\rangle(t)$, the original spectra $p(\delta\omega)$ initially fed into the simulations is be reconstructed. Namely,

$$\mathcal{W}^{CH}(\delta\omega) = \mathcal{F}\big\{\, \langle S_X^{CH}\rangle(t) + i\, \langle S_Y^{CH}\rangle(t) \big\} \equiv p(\delta\omega). \tag{2.13}$$

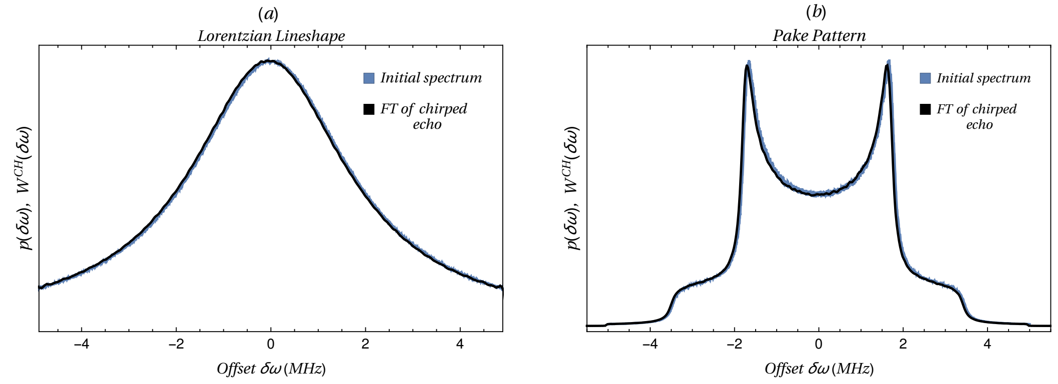

Figure 2.7: Input spectra $p(\delta\omega)$ (in blue) and $\mathcal{W}^{CH}(\delta\omega)$ (in black) superimposed for a Lorentzian lineshape in (a) and for a Pake pattern in (b).

Still left to tackle is the filtering of the magnetization signal during detection. As explained in section 1.3.1, the resonator both applies the control fields and picks up the response of the spins. Therefore, the narrow bandwidth of the resonator affects not only the control but also the detection of the spin signal. In particular, the resonator modelled after the RLC circuit of section 2.2.3 acts as a filter $H(s) = \mathcal{L}\{h(t)\} = \mathcal{L}\{e^{-t/\tau_c}\}$, which convolved with the output signal $\langle S_X^{CH}\rangle(t)$ and $\langle S_Y^{CH}\rangle(t)$, yields the filtered magnetization

$$\langle \tilde{S}_i^{CH}\rangle(t) = \langle S_i^{CH}\rangle(t) * h(t) \quad \text{for } i = X,\ Y, \tag{2.14}$$

as presented in figure 2.8.

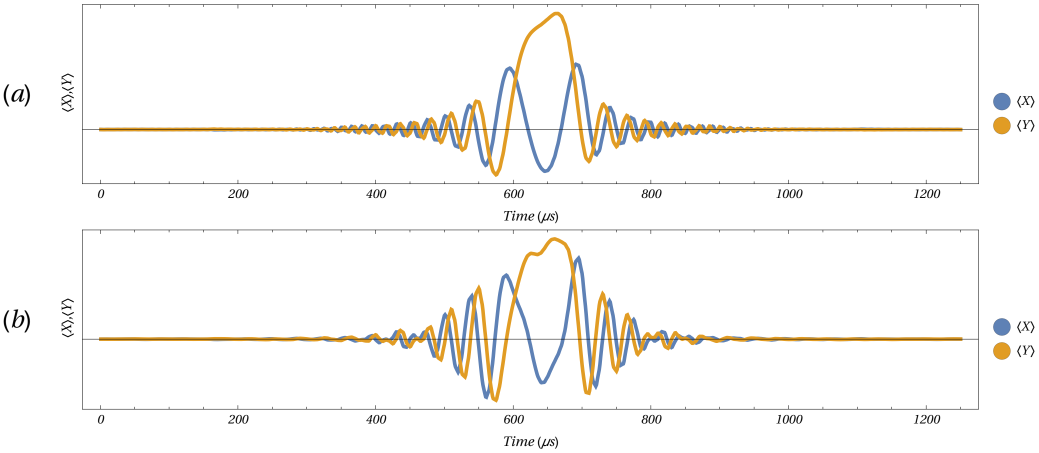

Figure 2.8: In (a) we show the chirped echo $\langle S_X^{CH}\rangle(t)$ and $\langle S_Y^{CH}\rangle(t)$ after being filtered by the resonator for a Lorentzian lineshape; and in (b), for a Pake pattern.

In figure 2.9, we show the Fourier Transform of the filtered signal

$$\tilde{\mathcal{W}}^{CH}(\delta\omega) = \mathcal{F}\big\{\, \langle \tilde{S}_X^{CH}\rangle(t) + i\, \langle \tilde{S}_Y^{CH}\rangle(t) \big\}. \tag{2.15}$$

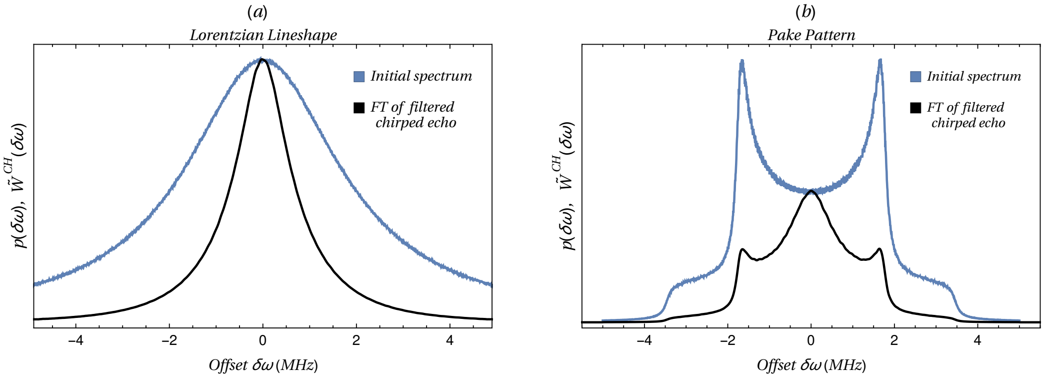

Figure 2.9: Input spectra $p(\delta\omega)$ (in blue) and $\tilde{\mathcal{W}}^{CH}(\delta\omega)$ (in black) superimposed for a Lorentzian lineshape in (a) and for a Pake pattern in (b).

In it, it becomes apparent that the magnetization components with frequencies outside the resonator bandwidth have been filtered out. Thus, a correct reconstruction is unattainable.

2.3.2 Bandwidth-limited detection

To overcome the limited resonator bandwidth in the detection step, we add a third sweep to the control pulse $p_Z(t)$ simultaneous to the formation of the chirped echo, starting at time t_i and ending at time t_f.

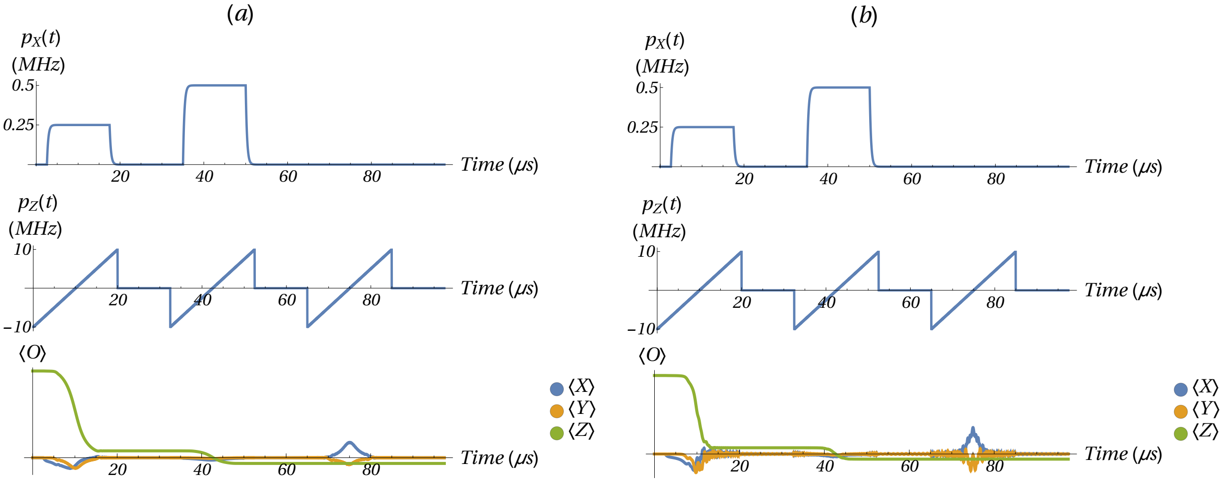

Figure 2.10: In (a), we depict pulses $p_X(t)$ and $p_Z(t)$ together with the observable evolution $\langle \mathbf{O} \rangle(t)$ for the Lorentzian lineshape of figure 2.1 (a). Similarly, in (b) we show another evolution $\langle \mathbf{O} \rangle(t)$ for the same input pulses but the spectra being the Pake pattern of figure 2.1 (b).

The first two sweeps bring different parts of the spectra sequentially on resonance with the cavity, all while applying the rectangular pulses $\Omega_{\pi/2}$ and Ω_π. Therefore, the first isochromat brought on resonance ($\Delta\omega_s$), is the first one to refocus at time t_i. It follows that if we sweep slowly enough and the sweep is linear, then the modulation frequency of the chirped echo is also a linear function in time,

$$\Delta\omega_{mod}(t) = -\Delta\omega_{3s}(t) = \frac{\Delta\omega_s}{t_f - t_i}\big((t_f + t_i) - 2t\big). \tag{2.16}$$

In order to pick up the contribution of all isochromats to the magnetization signal, we have to remove the frequency modulation from the echo to avoid cavity filtering. To "unmodulate" the chirped echo, it is sufficient to apply a linear sweep simultaneous to the formation of the echo. This third sweep is identical to the first and second sweeps. As shown in figure 2.11, the simulated echoes $\langle S_X^E\rangle(t)$ and $\langle S_Y^E\rangle(t)$ are not chirped anymore due to the third sweep.

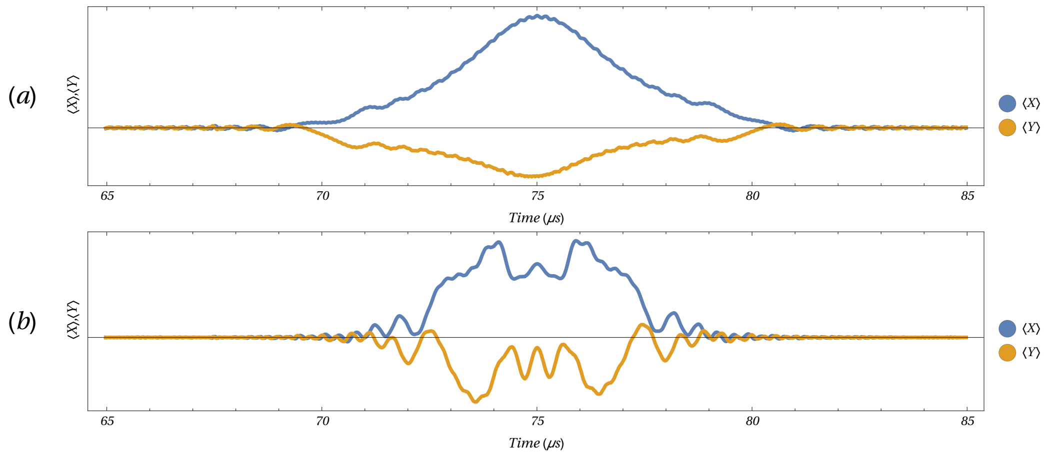

Figure 2.11: Plot (a) shows the echo of figure 2.10 (a), $\langle S_X^E\rangle(t)$ and $\langle S_Y^E\rangle(t)$, simulated for a Lorentzian lineshape; and (b), the echo of figure 2.10 (b), simulated for a Pake pattern.

To visualize how most of the frequency components of $\langle S_X^E\rangle(t)$ and $\langle S_Y^E\rangle(t)$ are centered around zero, we plot in figure 2.12 the Fourier Transforms of the echo signals $\langle S_X^E\rangle(t)$ and $\langle S_Y^E\rangle(t)$,

$$\mathcal{W}^E(\delta\omega) = \mathcal{F}\big\{\,\langle S_X^E\rangle(t) + i\,\langle S_Y^E\rangle(t)\big\}. \tag{2.17}$$

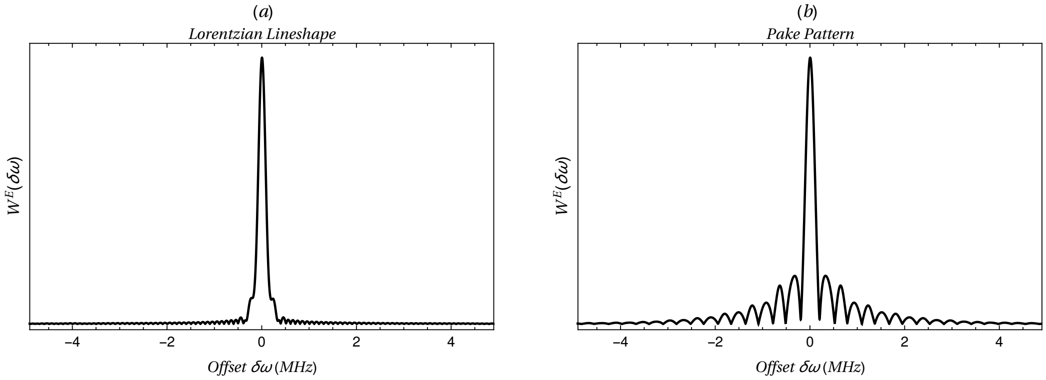

Figure 2.12: Fourier Transform $\mathcal{W}^E(\delta\omega)$ for a Lorentzian lineshape in (a) and a Pake pattern in (b).

To mimic the detection of the signal through a high-Q resonator, we convolve the output spin signal $\langle S_X^E\rangle(t)$ and $\langle S_Y^E\rangle(t)$ with the resonator impulse response $h(t)$. Moreover, we assume that there is some noise, arising from the electronics of the detection system. Hence, we add some white noise $w(t)$ with an SNR of 100,

$$\langle \tilde{S}_i^E \rangle(t) = \langle S_i^E \rangle(t) * h(t) + w(t), \tag{2.18}$$

In this case, the definition of SNR used is the peak height (A_{s_p}) divided by the root-mean-square value of the noise ($A_{n_{RMS}}$),

$$SNR = A_{s_p}/A_{n_{RMS}}. \tag{2.19}$$

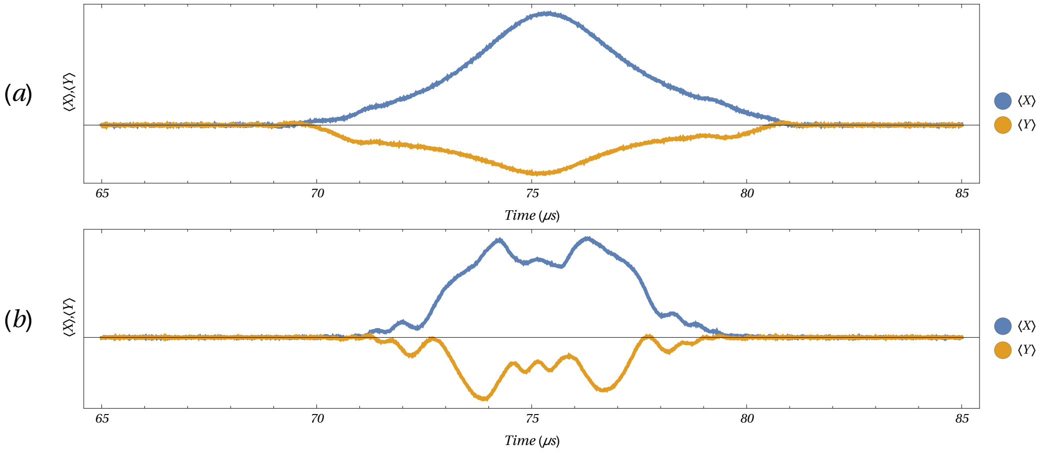

Figure 2.13: Filtered echoes with added white noise $\langle \tilde{S}_X^E \rangle(t)$ and $\langle \tilde{S}_Y^E \rangle(t)$ for a Lorentzian lineshape in (a) and a Pake pattern in (b).

To check whether detection through a high-Q cavity affects the "un-modulated" echo, we take the FT of $\langle \tilde{S}_X^E \rangle(t)$ and $\langle \tilde{S}_Y^E \rangle(t)$,

$$\tilde{\mathcal{W}}^E(\delta\omega) = \mathcal{F}\{\, \langle \tilde{S}_X^E \rangle(t) + i\, \langle \tilde{S}_Y^E \rangle(t) \},\tag{2.20}$$

and compare it to $\mathcal{W}^E(\delta\omega)$ in figure 2.14.

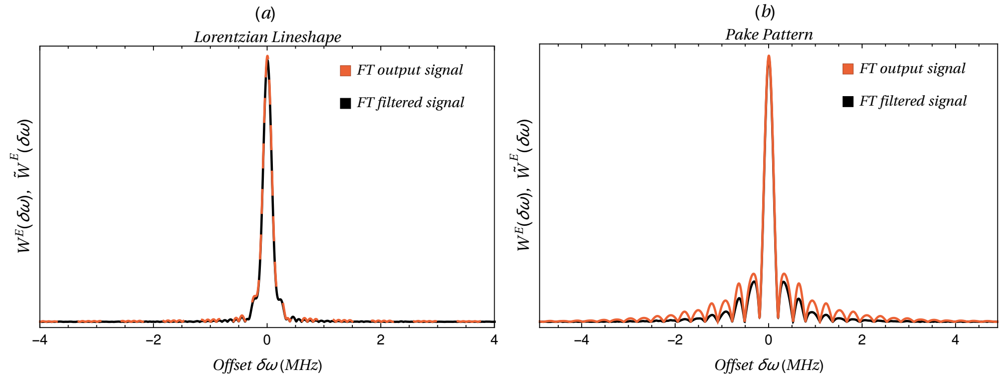

Figure 2.14: In black, $\tilde{\mathcal{W}}^E(\delta\omega)$. In orange, $\mathcal{W}^E(\delta\omega)$ as shown in 2.12. As mentioned before, (a) shows the results for a Lorentzian lineshape and (b) for a Pake pattern.

The Lorentzian lineshape is barely distorted. More noticeable, however, is the dampening of the lobes of the Pake pattern.

To now reconstruct the spectra, we multiply the filtered signal $\langle \tilde{S}_i^E \rangle(t)$ with a frequency modulated (FM) function $FM(t)$ whose frequencies vary linearly from $-\Delta\omega_s = -10$ MHz to $\Delta\omega_s = 10$ MHz. Namely,

$$\langle \tilde{S}_X^M \rangle(t) = \mathrm{Re}\Big[\langle \tilde{S}_X^E \rangle(t) \cdot FM(t)\Big] + \mathrm{Im}\Big[\langle \tilde{S}_Y^E \rangle(t) \cdot FM(t)\Big], \tag{2.21}$$

and

$$\langle \tilde{S}_Y^M \rangle(t) = \mathrm{Re}\Big[\langle \tilde{S}_Y^E \rangle(t) \cdot FM(t)\Big] + \mathrm{Im}\Big[\langle \tilde{S}_X^E \rangle(t) \cdot FM(t)\Big], \tag{2.22}$$

where

$$FM(t) = \exp\Big\{2\pi i \int \Delta\omega_{mod}(t)dt\Big\} = \exp\Big\{-2\pi i \frac{\Delta\omega_s}{t_f - t_i}\big(t^2 - (t_f + t_i)t\big)\Big\}. \tag{2.23}$$

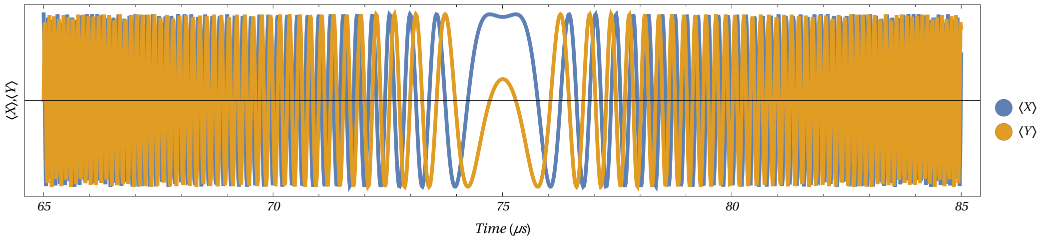

Figure 2.15: Real and imaginary parts of the FM function of equation 2.23.

The reconstructed functions $\langle \tilde{S}_X^M \rangle(t)$ and $\langle \tilde{S}_Y^M \rangle(t)$ are shown in the following figure 2.16:

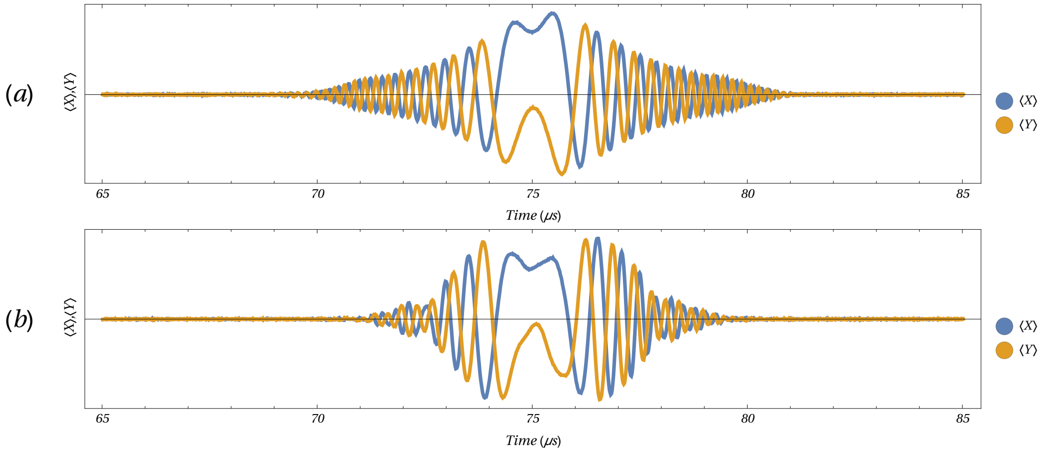

Figure 2.16: Reconstructed chirped echo $\langle \tilde{S}_X^M \rangle(t)$ and $\langle \tilde{S}_Y^M \rangle(t)$ for a Lorentzian lineshape in (a) and a Pake pattern in (b).

By taking the FT of the signals displayed above, i.e.,

$$\tilde{\mathcal{W}}^M(\delta\omega) = \mathcal{F}\Big\{\langle \tilde{S}_X^M \rangle(t) + i\,\langle \tilde{S}_Y^M \rangle(t)\Big\} \tag{2.24}$$

we obtain the results of figure 2.17. Subplot 2.17 (a) shows a Lorentzian lineshape shifted in frequency. The reason behind it is a slight time delay introduced by the transfer function when filtering the echo signal. If we do not account for this time shift when multiplying the filtered echo with the FM signal, it translates into a frequency shift. That does not seem to be too problematic in the case of 2.17 (a), but substantially distorts the reconstructed Pake pattern in subplot 2.17 (b).

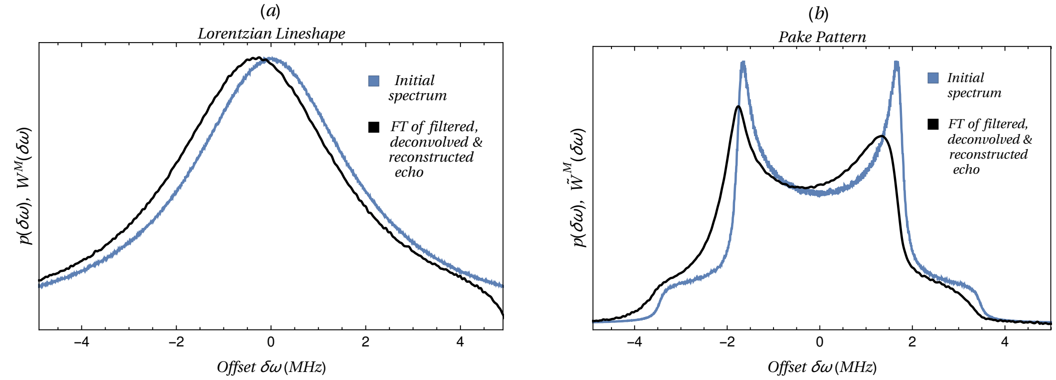

Figure 2.17: Input spectra $p(\delta\omega)$ (in blue) and $\tilde{\mathcal{W}}^M(\delta\omega)$ (in black) superimposed in (a) for a Lorentzian lineshape and in (b) for a Pake pattern.

This issue can be easily resolved by deconvolving the filtered signal with the resonator transfer function in an additional post-processing step. Namely,

$$\langle S_i^D \rangle(t) = \mathcal{L}^{-1}\left\{ \langle \tilde{S}_i^E \rangle(t) \right\} \quad \text{for } i = X, Y. \tag{2.25}$$

The deconvolved functions $\langle S_X^D \rangle(t)$ and $\langle S_Y^D \rangle(t)$ are shown in figure 2.18.

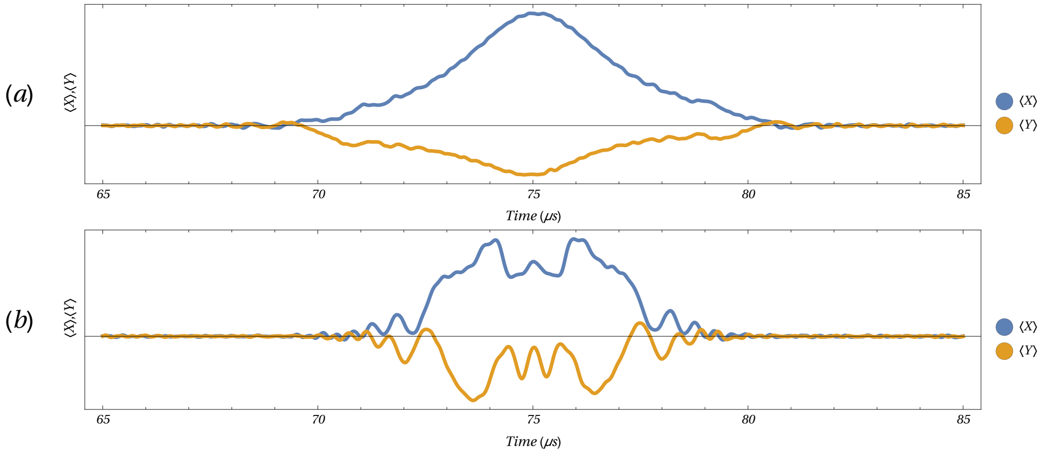

Figure 2.18: Deconvolved echoes $\langle S_X^D \rangle(t)$ and $\langle S_Y^D \rangle(t)$ for a Lorentzian lineshape in (a) and a Pake pattern in (b).

If we take the FT of the deconvolved echoes of figure 2.18

$$\mathcal{W}^D(\delta\omega) = \mathcal{F}\big\{ \langle S_X^D \rangle(t) + i\, \langle S_Y^D \rangle(t) \big\}, \tag{2.26}$$

we obtain a spectral profile very close to the one of figure 2.12. Both $\mathcal{W}^E(\delta\omega)$ and $\mathcal{W}^D(\delta\omega)$ are compared in figure 2.19.

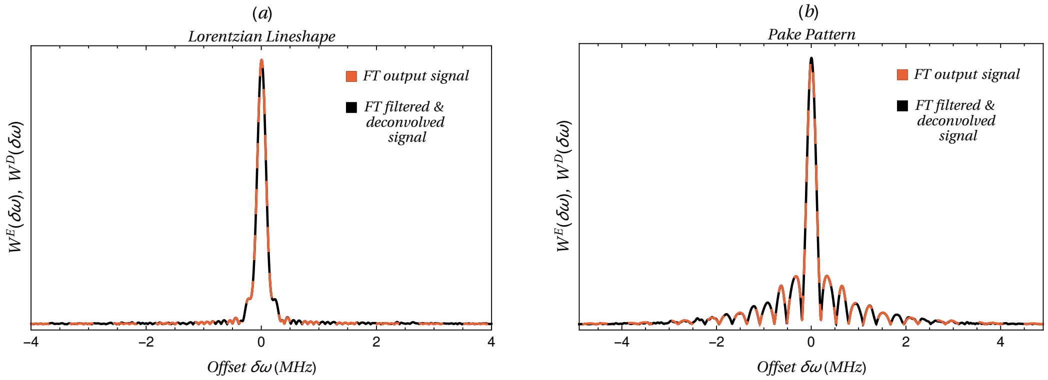

Figure 2.19: The spectra $\mathcal{W}^E(\delta\omega)$ (in orange), superimposed to the FT of the deconvolved signal $\mathcal{W}^D(\delta\omega)$ (in black), for a Lorentzian lineshape in (a) and a Pake pattern in (b).

By multiplying the deconvolved echoes with the frequency-modulated function $FM(t)$,

$$\langle S_X^M \rangle(t) = \mathrm{Re}\left[\langle S_X^D \rangle(t) \cdot FM(t) \right] + \mathrm{Im}\left[\langle S_Y^D \rangle(t) \cdot FM(t) \right], \tag{2.27}$$

and

$$\langle S_Y^M \rangle(t) = \mathrm{Re}\left[\langle S_Y^D \rangle(t) \cdot FM(t) \right] + \mathrm{Im}\left[\langle S_X^D \rangle(t) \cdot FM(t) \right], \tag{2.28}$$

we retrieve the two frequency modulated echoes of figure 2.20.

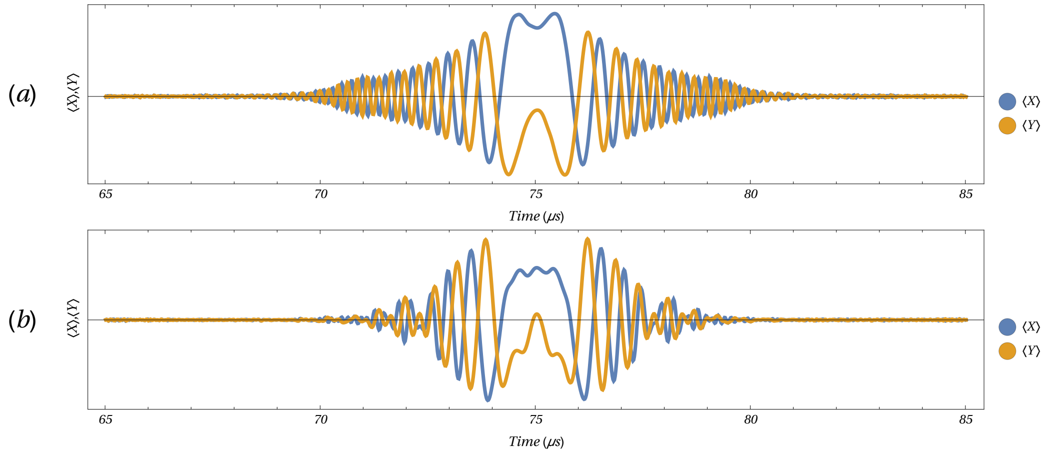

Figure 2.20: Reconstructed echoes $\langle S_X^M \rangle(t)$ and $\langle S_Y^M \rangle(t)$ for a Lorentzian lineshape in (a) and a Pake pattern in (b).

Finally, in figure 2.22 we compare the FT of the reconstructed chirped echoes

$$\mathcal{W}^M(\delta\omega) = \mathcal{F}\{\,\langle S_X^M\rangle(t) + i\,\langle S_Y^M\rangle(t)\},\tag{2.29}$$

with the input spectra of our simulations, $p(\delta\omega)$.

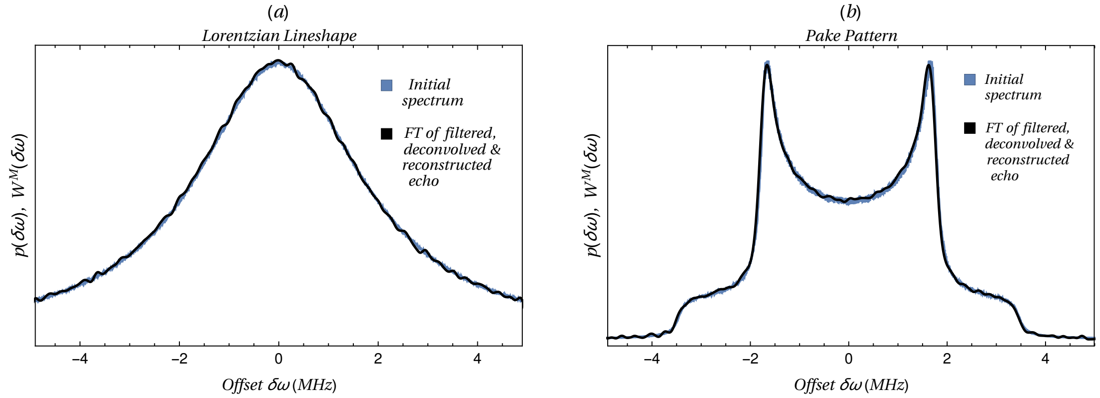

Figure 2.21: Input spectra $p(\delta\omega)$ (in blue) superimposed with $\mathcal{W}^M(\delta\omega)$ (in black) for a Lorentzian lineshape in (a) and a Pake pattern in (b).

The slight deviations in both spectra of figure 2.22 arise due to the noise added before the deconvolution step. The smaller the SNR the more pronounced these deviations become.

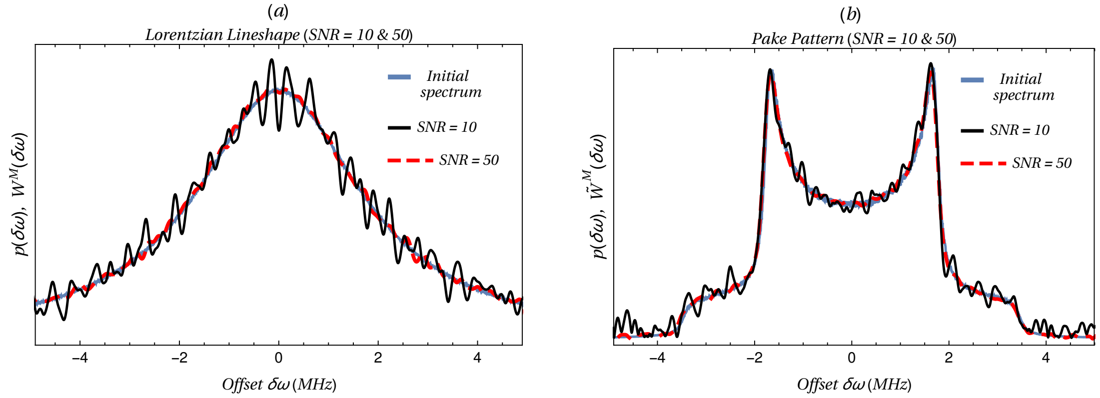

Figure 2.22: Figure showing the deviations in the spectra recovery due to a noise increase. In solid blue, the original input spectra. In dashed red, the reconstructed spectra after introducing white noise with $SNR = 50$. In solid black, the reconstructed spectra for $SNR = 10$. Subplot (a) presents the results for a Lorentzian lineshape and subplot (b) for a Pake pattern.

2.3.3 Summary

To conclude this section, let us summarize the reconstruction steps for our spectra:

1. Apply a pulse sequence as described in figure 2.2 (b). Namely, a $\pi/2$ and a π pulse about the $\hat{x}$ axis, simultaneous to linear sweeps, plus a third linear sweep simultaneous to the formation of the chirped echo.

2. Deconvolve the measured echo with the filter function of the resonator.

3. Modulate the echo by multiplying it with a frequency-modulated function whose frequency profile is the same but opposite in sign to the sweep function $\Delta\omega_{3s}(t)$.

4. Take the Fourier Transform of the modulated echo $\langle S_X^M\rangle(t) + i\,\langle S_Y^M\rangle(t)$.

2.4 NMR implementation

The system of choice to test the proposal described in the previous section was liquid-state Nuclear Magnetic Resonance, due to its broad use as a testbed for quantum control [39]. Despite it being broadband, the conditions imposed by the high-Q of the resonator can be emulated by adapting some pulse parameters and employing the shim coils already present in the design to artificially broaden the spectrum and apply the z-field sweeps.

In this section, we first describe the sample and system used for our experiments. Then, we argue how the challenges we are trying to address in the ESR simulations can be emulated using liquid NMR. Finally, we present the obtained results and discuss them.

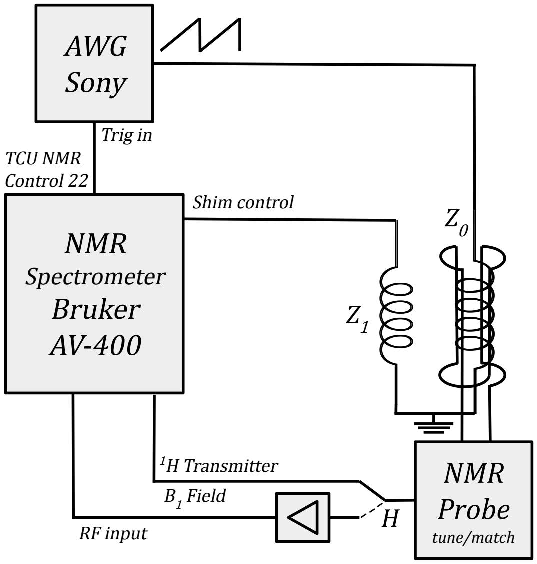

Figure 2.23: Diagram of the NMR setup used to pulse and simultaneously sweep the z-field with the Z_0 shim coil.

The chosen sample is D_2O with very low proton concentration. The T_2 was measured to be approximately 2.015 s through a standard echo experiment. The system is a 9.4T Brucker magnet and 400 MHz (proton resonance at 9.4T) spectrometer. The Z_1 shim is employed to artificially broaden the sample spectrum to 1.23 kHz (figure 2.26). Transmission of the x, y-controls by a high Q resonator is emulated by using long control pulses of 50 ms, which have a limited operation bandwidth of approximately 20 Hz $\ll$ 1.23 kHz. The z-control is applied using the Z_0 shim coil of the NMR apparatus connected through the spectrometer to an arbitrary waveform generator (AWG 2021 Sony Tektronix).

Voltage	Frequency shift
0.5V	1.23 kHz
1V	2.46 kHz
1.5V	3.69 kHz
2V	4.92 kHz

Figure 2.24: Table showing the frequency shift induced by applying some voltage to the Z_0 shim coil.

Substituting the AWG with a constant voltage source (BK PRECISION 9121A), we calibrated the input power v.s. the shift in frequency produced by the Z_0 coil. The obtained results are presented in table 2.24.

With this information we can now choose a proper sweep range that covers the measured linewidth of our sample. In our case, we sweep from -0.3 V to 0.3 V, which translates into a frequency range of approximately 1.4 kHz.

The first step is to measure the sample spectrum. To do so, we perform a standard Hahn echo experiment with hard pulses of length $t_{p_{\pi/2}} = 11$ μs and $t_{p_\pi} = 22$ μs to excite and refocus the magnetization. The result is the Hahn echo of figure 2.25, and its spectrum, with a linewidth of 1.23 kHz is shown in figure 2.25.

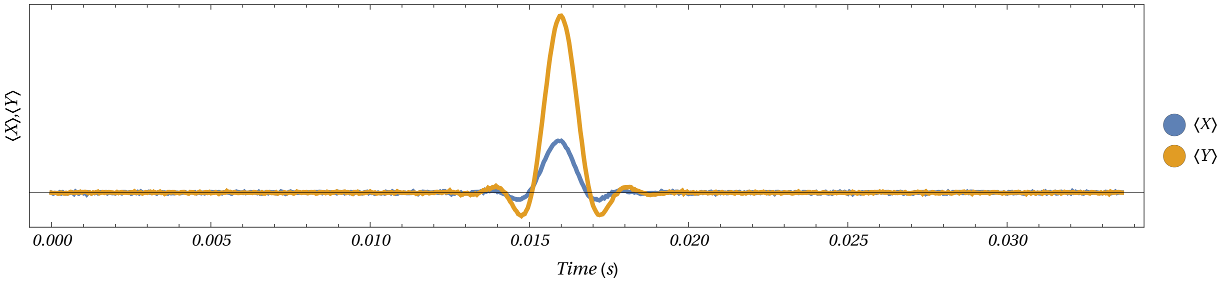

Figure 2.25: Hahn echo obtained after applying two hard broadband pulses of length $t_{p_{\pi/2}} = 11$ μs and $t_{p_\pi} = 22$ μs, inducing a $\pi/2$ and π rotation, respectively. In blue, we show the evolution of $\langle S_X\rangle(t)$, and in yellow, $\langle S_Y\rangle(t)$.

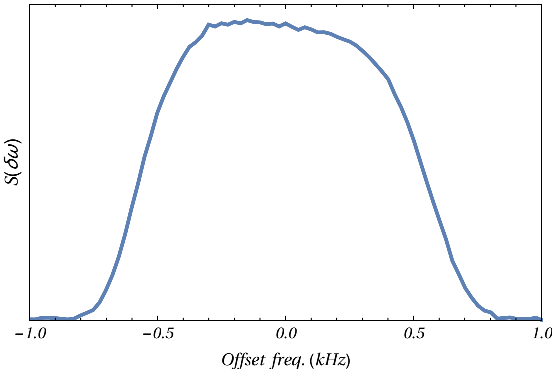

Figure 2.26: Spectrum to recover, obtained by applying a Fourier Transform to the Hahn echo of figure 2.25.

Next, two 50 ms pulses are applied while sweeping the z-field with the Z_0 shim coil. The range of the linear z-sweep is of 1.4 kHz (as shown in figure 2.27 (a)).

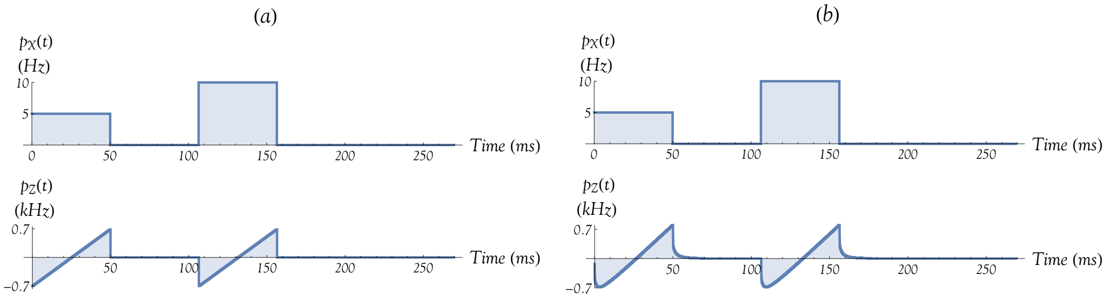

Figure 2.27: Subplot (a) shows the x and z controls pre-distortion and (b) post-distortion applied to generate the chirped echo of figure 2.29.

In contrast with the RLC circuit model of the ESR simulations, the NMR coil does not have a high-Q and thus does not significantly distort the x-control pulses. However, the z control applied through the Z_0 shim coil will be affected by several components of the control hardware, such as the coil itself, the AWG, the spectrometer, etc. To model such a distortion, we first apply a step function. Immediately after, we measure the response signal generated by the spins when applying a constant z field using a the BK controllable power supply. From the response signal of the spins, we extract the phase. Its derivative will be the frequency of the spins as a function of time, which is fitted to obtain an approximate model for the transfer function of the hardware responsible for the z-field sweep. The impulse response function turns out to be a weighted sum of three exponentials, each with a different decay constant,

$$h(t) = \exp\{-t/\tau_1\} + \frac{1}{2}\exp\{-t/\tau_2\} + \frac{1}{4}\exp\{-t/\tau_3\}, \tag{2.30}$$

where $\tau_1 = 0.858$ ms, $\tau_2 = 15$ ms and $\tau_3 = 71.4$ms. It is likely that these different time constants are due to Eddy currents arising from copper-based materials surrounding the sample. We hypothesize that the gradient coil is responsible for τ_1, the shielding of the probe for τ_2 and the magnetic bore for τ_3. Given this measured impulse response, the distorted z-control pulse becomes,

$$\tilde{p}_Z(t) = p_Z(t) * h(t). \tag{2.31}$$

In the plots displayed in the following figure 2.28, we show both $p_Z(t)$ and $\tilde{p}_Z(t)$.

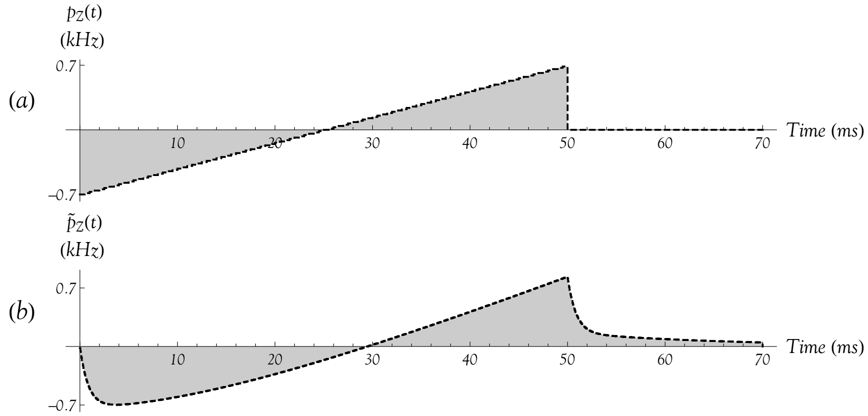

Figure 2.28: We show the undistorted linear z-field sweep in (a) and the distorted sweep $\tilde{p}_Z(t)$ in (b).

By applying the control sequences of figure 2.27 we detect, as expected, a chirped echo of 50 ms length, shown in figure 2.29. Its Fourier Transform is shown in figure 2.30.

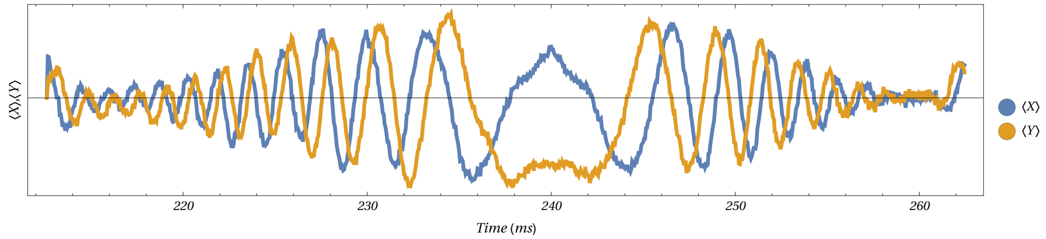

Figure 2.29: Chirped echo of 50 ms length. As in previous images, in blue we show the evolution of $\langle S_X \rangle(t)$, and in yellow, $\langle S_Y \rangle(t)$.

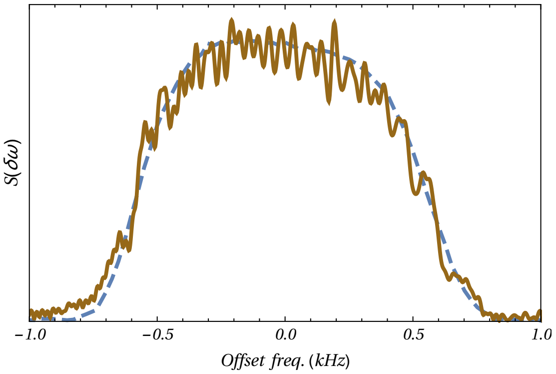

Figure 2.30: Fourier Transform of chirped echo in dark yellow, compared in blue with the spectrum of figure 2.26.

From 2.30 we can appreciate that the SNR of the chirped echo is lower than the SNR of the Hahn echo. It should be expected, since for each isochromat the tip angle is smaller than the rotation experienced when applying a hard pulse.

After measuring the spectrum obtained through FT of a chirped echo, we next add the third linear z-sweep during echo formation.

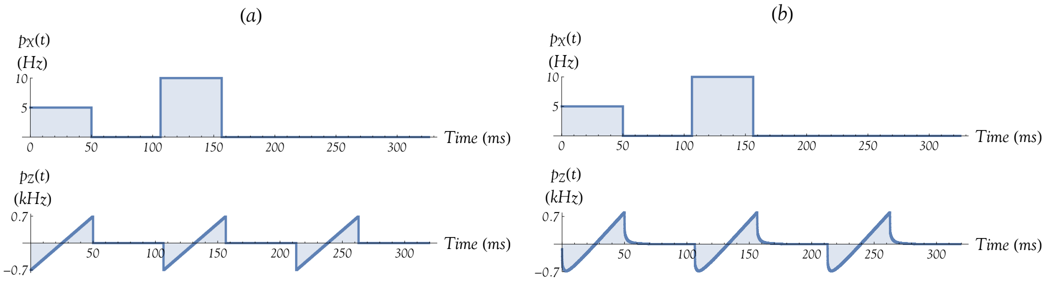

Figure 2.31: Subplot (a) shows the undistorted x and z controls and (b) shows the distorted pulses the spin ensemble experiences according to our model.

The resulting echo spans 50 ms and is shown in figure 2.32. As can be appreciated from the FT shown in figure 2.33, its modulation has been effectively removed by applying the third sweep.

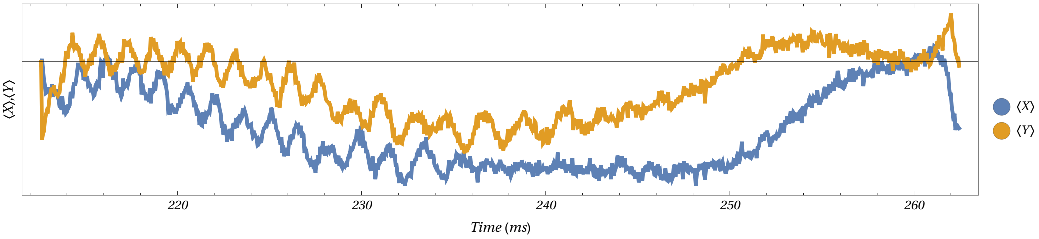

Figure 2.32: Echo obtained by applying the pulses of figure 2.31 where, in blue, we show the evolution of $\langle S_X\rangle(t)$ and, in yellow, $\langle S_Y\rangle(t)$.

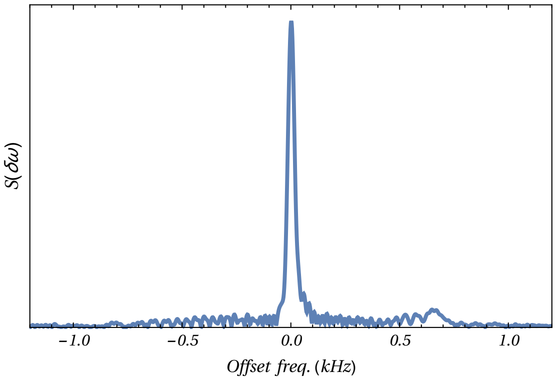

Figure 2.33: Fourier Transform of echo of figure 2.32.

The next step is to modulate the detected echo of figure 2.32. To do so, we multiply the echo with the frequency-modulated function ($FM(t)$) shown in figure 2.34. Note that since the field sweeps applied to the sample are distorted, the modulation of the function $FM(t)$ will also be distorted. Namely, $\Delta\omega_{mod} = -\Delta\omega_{3s}$, as established in equation 2.16.

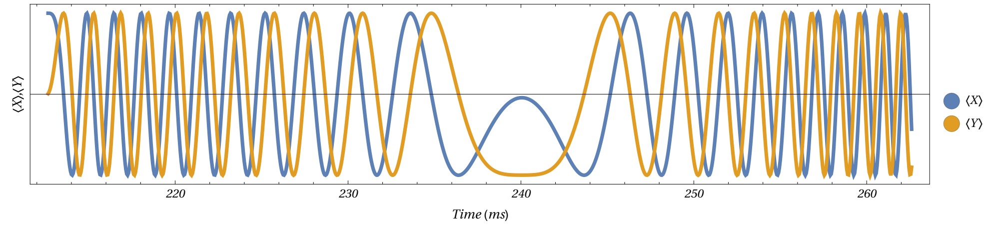

Figure 2.34: Frequency modulated (FM) function whose frequency profile is $\Delta\omega_{mod} = -\Delta\omega_{3s}$, where $\Delta\omega_{3s}$ is the function of figure 2.28. In blue, the real part of the FM function and in yellow, the imaginary part.

The multiplication of the FM function with the detected echo is shown in figure 2.35.

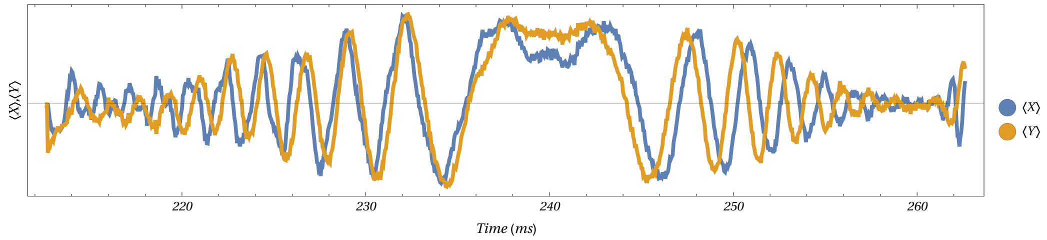

Figure 2.35: Reconstructed echo obtained after multiplying a FM function with the detected echo of figure 2.32.

If we take the Fourier Transform of the reconstructed chirped echo, we obtain the spectrum presented in green in figure 2.36.

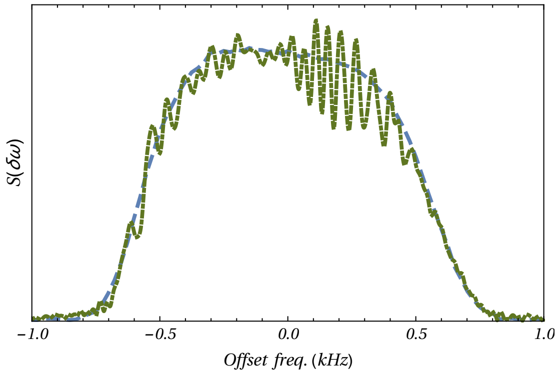

Figure 2.36: Reconstructed spectrum in dot-dashed green superimposed to the spectrum measured using hard pulses, in dashed blue.

2.5 Conclusions

In this chapter we presented detailed numerical simulations confirming that sweeping a z-control during the excitation, refocusing and formation of a chirped echo allows us to reconstruct the spectrum of our sample. This demonstrates a practical method for detecting broad spectra of samples in pulsed ESR when using bandwidth-limited high Q resonators.

Moreover, we have shown a successful implementation of our pulse sequence in an NMR platform. While there are some inherent differences between a broadband NMR setup and high-Q ESR resonators, our results constitute a good proof-of-principle demonstration of our scheme.

Chapter 3

k-space Analysis

3.1 Introduction

The main objective of this chapter is to present a complete analytical description of the $\delta\omega$-frequency dependent magnetization at any point in time, applicable to the multiple situations where inhomogeneities introduce a spatial distribution in the sample.

Conventionally, this problem has been studied for the case of hard RF pulses applied in the transverse plane $x - y$ and external field gradients [13, 14, 40]. Based on this previous and well established work, we build up our theory describing the effect of soft pulses on the evolution of the $\delta\omega$-frequency dependent magnetization. This dependence on the precession frequency can be caused not only by external field gradients but also by inhomogeneous fields, different chemical environments or orientation-dependent effects such as g-anisotropy in ESR.

The magnetization as a function of the precession offset $\delta\omega$ can be expressed as a linear combination of basis functions with two sets of coefficients $A^n_m(\delta\omega)$ and $A^n_{z,m}(\delta\omega)$. This decomposition enables us to study the transformation of the magnetization due to soft RF pulses in terms of the transformation of the basis functions [14]. Through lengthy but straightforward calculations we derive three different sets of coupled recursive formulas, each one for a different initial state $\rho_0 = \sigma_X,\ \sigma_Y$ and σ_Z. The coupled equations relate the set of coefficients describing the magnetization evolution after $n-1$ soft pulses with the state of the magnetization after the nth pulse.

Next, we highlight the correspondence between these coefficients and the paths in the reciprocal space or k-space grating [12, 13].

Last, we tackle continuous arbitrarily shaped pulses. By discretizing the control pulses and thus, treating them as a multipulse sequence, we use the coupled recursive formulas to compute the $\delta\omega$-dependent magnetization at any point in time. Afterwards, we compute the limit of the pulse length t_p approaching zero. Through an analysis of the paths in the k-space grating, and by grouping them in terms of their smaller order, we rederive non-linear response theory, also known as the Volterra series or Kubo's formula [15–17].

Note that throughout this analysis relaxation and distant dipolar effects have been neglected.

3.2 Basic definitions and basis functions

The relevant internal and control Hamiltonians are

$$H_{int} = \frac{1}{2}\delta\omega\sigma_Z, \tag{3.1}$$

and

$$H_{contr} = \frac{1}{2}\omega_1(t)\sigma_X - \frac{1}{2}\Delta\omega(t)\sigma_Z, \tag{3.2}$$

where $\delta\omega = \omega_0 - \omega_t$ is the detuning between the precession frequency of the strong magnetic field ω_0 and the transmitter frequency ω_t (both Hamiltonians are in the rotating frame of the transmitter frequency ω_t).

Control pulses $p_X(t) = \omega_1(t)$ and $p_Z(t) = \Delta\omega(t)$ in 3.2 are of a particular type: a series of rectangular equispaced pulses of length t_p, each one with arbitrary Rabi frequency $0 \leq \omega_{1_n} \leq \omega_{1_{max}}$ and offset $-\Delta\omega_s \leq \Delta\omega_n \leq \Delta\omega_s$ (see figure 3.1).

The signal detected is a combination of the X and Y components of the magnetization vector, i.e., the transverse magnetization $M_{trans}(t) = M_x(t) + iM_Y(t)$, where $M_x(t) \equiv \langle S_X\rangle(t)$ and $M_y(t) \equiv \langle S_Y\rangle(t)$. The orthogonal component to the transverse magnetization is the longitudinal magnetization and is defined as $M_{long}(t) = M_Z(t) = \langle S_Z\rangle(t)$.

As stated in 1.13, the total magnetization components $M_X(t)$, $M_Y(t)$ and $M_Z(t)$ are made up from the individual contributions of each isochromat $M_i(t;\delta\omega) \equiv \langle\sigma_i\rangle(t;\delta\omega)$ and can therefore be understood as a weighted average over the ensemble,

$$M_i(t) \equiv \langle S_i\rangle(t) = \int p(\delta\omega)\ M_i(t;\delta\omega)\ \mathrm{d}(\delta\omega). \tag{3.3}$$

where $p(\delta\omega)$ is a probability density function associated to the parameter $\delta\omega$.

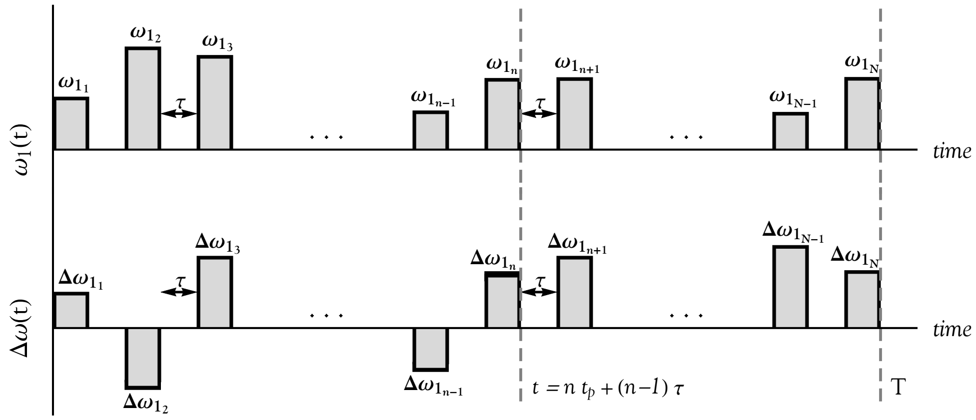

Figure 3.1: Plot corresponding to the X and Z control pulses (top and bottom) chosen to elaborate on our theory. Both the pulse length t_p as well as the time separation τ are chosen to be constant over all the sequence.

Assuming an initially uncorrelated state (a state that does not initially depend on the parameter $\delta\omega$), the individual contributions of each isochromat to the transverse and longitudinal magnetizations can be decomposed [14] as

$$M_{trans}(t;\delta\omega) = \sum_{m=-n+1}^{n-1} A_m^n(\delta\omega) e^{im\tau\delta\omega}, \tag{3.4}$$

and

$$M_{long}(t;\delta\omega) = \mathrm{Re}\left[\sum_{m=0}^{n-1} A_{z,m}^n(\delta\omega) e^{im\tau\delta\omega}\right], \tag{3.5}$$

where the parameter τ is defined as the time interval between each rectangular pulse, $\{A_{z,m}^n(\delta\omega)\}_{m=0}^{n-1}$ and $\{A_m^n(\delta\omega)\}_{m=-n+1}^{n-1}$ are two sets of functions that depend on the variable $\delta\omega$ and n is an integer that counts the number of pulses applied, i.e. $n = (t+\tau)/(t_p+\tau)$. The coefficients $A_{z,m}^n(\delta\omega)$ and $A_m^n(\delta\omega)$ introduced above are functions that take real numbers and yield complex values. Namely, $A_{z,m}^n : \mathbb{R} \longrightarrow \mathbb{C}$ and $A_m^n : \mathbb{R} \longrightarrow \mathbb{C}$. They can thus be written in polar coordinates as $A_{z,m}^n(\delta\omega) = |A_{z,m}^n|\; e^{i\varphi_{z,m}^n}$ and $A_m^n(\delta\omega) = |A_m^n|\; e^{i\varphi_m^n}$, where we have dropped the notation specifying the dependence on $\delta\omega$ for convenience in both the modulus and the phase. Then, 3.4 and 3.5 can be rewritten as

$$M_{trans}(t;\delta\omega) = \sum_{m=-n+1}^{n-1} |A_m^n|\; e^{i(m\tau\delta\omega+\varphi_m^n)}, \tag{3.6}$$

and

$$M_{long}(t;\delta\omega) = \sum_{m=0}^{n-1} |A_{z,m}^n|\;\; \cos{(m\tau\delta\omega + \varphi_{z,m}^n)}. \tag{3.7}$$

Note from 3.6 and 3.7 that the three functions

$$\cos\left(|m|\tau\delta\omega + \varphi^{n}_{z,m}\right) \qquad e^{i(|m|\tau\delta\omega+\varphi^{n-1}_{|m|})} \qquad e^{i(-|m|\tau\delta\omega+\varphi^{n-1}_{-|m|})} \tag{3.8}$$

form a complete basis: any modulation of either the transverse or longitudinal magnetization can be decomposed in terms of these functions over different values of m. They are depicted in figure 3.2.

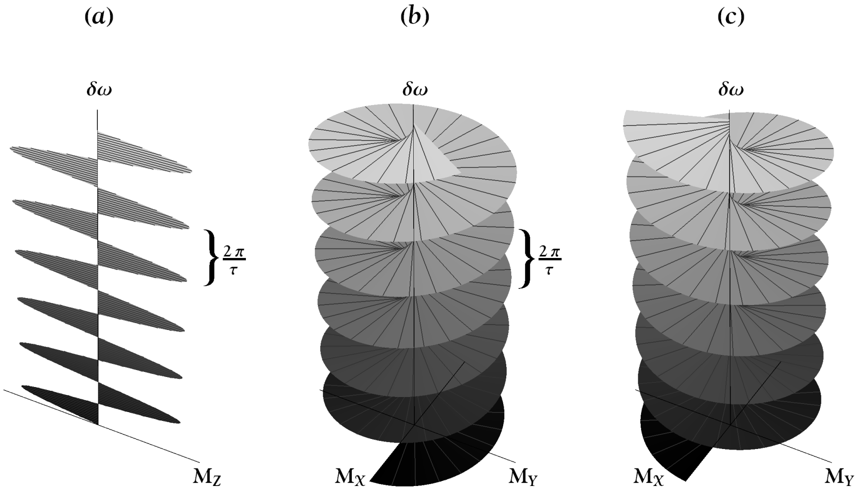

Figure 3.2: (a) Basis function of the longitudinal magnetization, a sinusoidal modulation $\cos\left(|m|\tau\delta\omega + \varphi^{n}_{z,|m|}\right)$ with $\varphi^{n}_{z,|m|} = 0$. (b), (c) Depiction of right-handed and left-handed helix, respectively.

Thus, if we want to understand how the internal and control Hamiltonians affect the magnetization vector, it is sufficient to analyze how the basis functions are transformed under the influence of 3.1 and 3.2.

3.3 Basis transformations

If no control pulses are applied to the system for a time τ, the system will exclusively be under the influence of the internal Hamiltonian in 3.1. It follows that the longitudinal magnetization will remain invariant and the transverse magnetization will acquire an additional phase of $\tau\delta\omega$ (table 3.1).

$e^{i(\lvert m\rvert\tau\delta\omega+\varphi^n_{\lvert m\rvert})}$	$\xrightarrow{H_{int} \text{ for time } \tau}$	$e^{i((\lvert m\rvert+1)\tau\delta\omega+\varphi^n_{(\lvert m\rvert+1)})}$
$e^{i(-\lvert m\rvert\tau\delta\omega+\varphi^n_{-\lvert m\rvert})}$	$\xrightarrow{H_{int} \text{ for time } \tau}$	$e^{i((-\lvert m\rvert+1)\tau\delta\omega+\varphi^n_{(-\lvert m\rvert+1)})}$
$\cos(\lvert m\rvert\tau\delta\omega+\varphi^n_{z,\lvert m\rvert})$	$\xrightarrow{H_{int} \text{ for time } \tau}$	$\cos(\lvert m\rvert\tau\delta\omega+\varphi^n_{z,\lvert m\rvert})$

Table 3.1: Table representing the evolution of the basis functions under the influence of the internal Hamiltonian for a time τ [14].

If we turn on a control Hamiltonian

$$H^n_{contr} = \frac{1}{2}\omega_{1_n}\ \sigma_X - \frac{1}{2}\Delta\omega_n\ \sigma_Z \tag{3.9}$$

for a time t_p during which both ω_{1_n} and $\Delta\omega_n$ are constant values, there will be a mixing of the magnetization components. In particular, time-independent pulses of length t_p, resonance offset $\delta\omega - \Delta\omega_n$, and a nominal nutation angle of $\alpha_{0_n} = \omega_{1_n} t_p$ can be represented as a rotation in three-dimensional space of an angle,

$$\alpha_n(\delta\omega) = \alpha_{0_n}\sqrt{1 + \left(\frac{\delta\omega - \Delta\omega_n}{\omega_{1_n}}\right)^2}, \tag{3.10}$$

about an effective axis tilted at an angle

$$\Delta_n(\delta\omega) = \tan^{-1}\left(\frac{\delta\omega - \Delta\omega_n}{\omega_{1_n}}\right) \tag{3.11}$$

with respect to the transverse plane. Note how both angles 3.10 and 3.11 are functions of $\delta\omega$. Hence, each isochromat will experience a different rotation about a different angle with respect to the transverse plane. The label n is used to keep count of how many pulses have been applied. Keeping 3.10 and 3.11 in mind, we can now map into a table 3.2 how the RF pulses act on the basis functions.

	$+\delta\omega$ Transverse, $\lvert A^n_{\lvert m\rvert}\rvert e^{i(\lvert m\rvert\delta\omega\tau+\varphi^n_{\lvert m\rvert})}$		$-\delta\omega$ Transverse, $\lvert A^n_{-\lvert m\rvert}\rvert e^{i(-\lvert m\rvert\delta\omega\tau+\varphi^n_{-\lvert m\rvert})}$		$+\delta\omega$ Longitudinal, $\lvert A^n_{z,\lvert m\rvert}\rvert\cos(\lvert m\rvert\delta\omega\tau+\varphi^n_{z,\lvert m\rvert})$	
	Ampl., $\lvert A^n_{\lvert m\rvert}\rvert$	Ph., $\varphi^n_{\lvert m\rvert}$	Ampl., $\lvert A^n_{-\lvert m\rvert}\rvert$	Ph., $\varphi^n_{-\lvert m\rvert}$	Ampl., $\lvert A^n_{z,\lvert m\rvert}\rvert$	Ph., $\varphi^n_{z,\lvert m\rvert}$
$+\delta\omega$ Trans., $\lvert A^{n-1}_{\lvert m\rvert}\rvert e^{i(\lvert m\rvert\delta\omega\tau+\varphi^{n-1}_{\lvert m\rvert})}$	$\lvert T_n\rvert\lvert A^{n-1}_{\lvert m\rvert}\rvert$	$\varphi^{n-1}_{\lvert m\rvert}+\phi_{T_n}$	$\sin^2(\alpha_n/2)\cos^2\Delta_n\lvert A^{n-1}_{\lvert m\rvert}\rvert$	$-\varphi^{n-1}_{-\lvert m\rvert}+2\phi$	$\lvert L_n\rvert\cos\Delta_n\lvert A^{n-1}_{\lvert m\rvert}\rvert$	$\varphi^{n-1}_{\lvert m\rvert}-\phi+\phi_{L_n}$
$-\delta\omega$ Trans., $\lvert A^{n-1}_{-\lvert m\rvert}\rvert e^{i(-\lvert m\rvert\delta\omega\tau+\varphi^{n-1}_{-\lvert m\rvert})}$	$\sin^2(\alpha_n/2)\cos^2\Delta_n\lvert A^{n-1}_{-\lvert m\rvert}\rvert$	$-\varphi^{n-1}_{\lvert m\rvert}+2\phi$	$\lvert T_n\rvert\lvert A^{n-1}_{-\lvert m\rvert}\rvert$	$\varphi^{n-1}_{-\lvert m\rvert}+\phi_{T_n}$	$\lvert L_n\rvert\cos\Delta_n\lvert A^{n-1}_{-\lvert m\rvert}\rvert$	$-\varphi^{n-1}_{\lvert m\rvert}+\phi+\pi-\phi_{L_n}$
$+\delta\omega$ Long., $\lvert A^{n-1}_{z,\lvert m\rvert}\rvert\cos(\lvert m\rvert\delta\omega\tau+\varphi^{n-1}_{z,\lvert m\rvert})$	$\frac{1}{2}\lvert L_n\rvert\cos\Delta_n\lvert A^{n-1}_{z,\lvert m\rvert}\rvert$	$\varphi^{n-1}_{z,\lvert m\rvert}+\phi+\pi+\phi_{L_n}$	$\frac{1}{2}\lvert L_n\rvert\cos\Delta_n\lvert A^{n-1}_{z,\lvert m\rvert}\rvert$	$-\varphi^{n-1}_{z,\lvert m\rvert}+\phi+\phi_{L_n}$	$(\cos\alpha_n\cos^2\Delta_n+\sin^2\Delta_n)\lvert A^{n-1}_{z,\lvert m\rvert}\rvert$	$\varphi^{n-1}_{z,\lvert m\rvert}$

Table 3.2: Basis functions transformations when the nth RF pulse $\alpha_{0_n})_\phi$ is applied at an offset frequency $\delta\omega-\Delta\omega_n$ during a time t_p and transverse phase ϕ. Table adapted from [14].

$$\begin{aligned}
|T_n| &= \sqrt{T_{r_n}^2+T_{i_n}^2},\\
\phi_{T_n} &= \tan^{-1}(T_{i_n}/T_{r_n}),\\
T_{r_n} &= \cos^2(\alpha_n/2)\cos^2\Delta_n+\cos\alpha_n\sin^2\Delta_n,\\
T_{i_n} &= \sin(\alpha_n/2)\sin\Delta_n,\\
|L_n| &= \sqrt{L_{r_n}^2+L_{i_n}^2},\\
\phi_{L_n} &= \tan^{-1}(L_{i_n}/L_{r_n}),\\
L_{r_n} &= \sin\alpha_n,\\
L_{i_n} &= 2\sin^2(\alpha_n/2)\sin\Delta_n
\end{aligned} \tag{3.12}$$

To exemplify how one would use table 3.2, let us consider the case where our ensemble is fully polarized ($M_0 = 1$) along the $\hat{z}$ direction. Such an initial state $M_0\hat{z} = \hat{z} = \sin(\pi/2)\hat{z}$ can be described with a longitudinal basis function of number $m = 0$, phase $\varphi^0_{z,0} = \pi/2$ and amplitude $|A^0_{z,0}| = M_0 = 1$. If we immediately apply one rectangular RF pulse ($n = 1$) of the characteristics described above, the magnetization vector will be modified, according to table 3.2 as,

$$\begin{aligned}
|A^0_{z,0}|\sin(\varphi^0_{z,0})\hat{z} \quad \xrightarrow{n=1} \quad & |A^1_0|e^{i\varphi^1_0} + |A^1_0|e^{i\varphi^1_0} + |A^1_{z,0}|\cos(\varphi^1_{z,0})\hat{z} = \\
&= \frac{1}{2}|L_1|\cos\Delta_1\ e^{i(\frac{\pi}{2}+\pi+\phi_{L_1})} + \frac{1}{2}|L_1|\cos\Delta_1\ e^{i(-\frac{\pi}{2}+\phi_{L_1})} + \\
&+\ (\cos\alpha_1\cos^2\Delta_1 + \sin^2\Delta_1)\sin(\pi/2)\ \hat{z} = \\
&= |L_1|\cos\Delta_1\ e^{i(-\frac{\pi}{2}+\phi_{L_1})} + (\cos\alpha_1\cos^2\Delta_1 + \sin^2\Delta_1)\ \hat{z}, \qquad (3.13)
\end{aligned}$$

where to distinguish the longitudinal from the transverse terms, we labeled the former with a unitary vector $\hat{z}$. It follows that the new amplitude and phase coefficients are,

$$\begin{aligned}
|A^1_0| &= |L_1|\cos\Delta_1 & \varphi^1_0 &= -\tfrac{\pi}{2} + \phi_{L_1} \\
|A^1_{z,0}| &= (\cos\alpha_1\cos^2\Delta_1 + \sin^2\Delta_1) & \varphi^1_{z,0} &= \pi/2
\end{aligned}$$

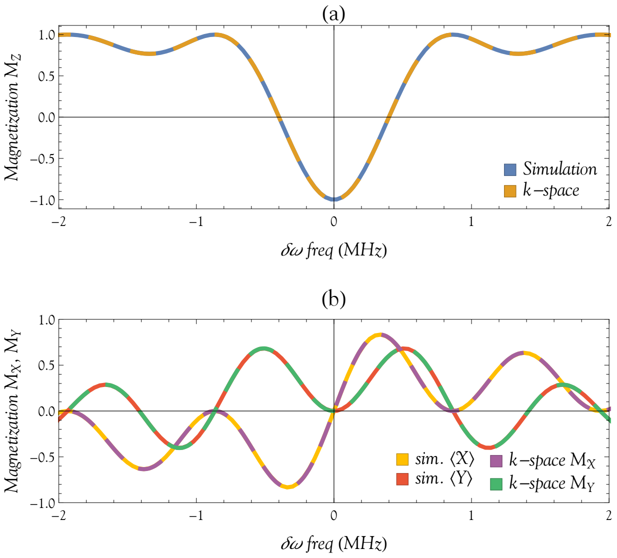

Figure 3.3: Subplot (a) shows $M_Z(\delta\omega)$, and subplot (b) $M_X(\delta\omega)$ and $M_Y(\delta\omega)$. In each plot we compare functions 3.14 and 3.15, to the simulations of $M_x(\delta\omega)$, $M_y(\delta\omega)$, and $M_z(\delta\omega)$ based on full Hamiltonian dynamics.

Thus, after one RF pulse of duration t_p, the transverse and longitudinal magnetization at $T = t_p$ will be

$$M_{trans}(t_p;\delta\omega) = |L_1|\cos\Delta_1\ e^{-\frac{\pi}{2}+\phi_{L_1}}, \qquad (3.14)$$

and

$$M_{long}(t_p;\delta\omega) = (\cos\alpha_1\cos^2\Delta_1 + \sin^2\Delta_1). \qquad (3.15)$$

A plot of these functions for a pulse of length $t_p = 1\mu s$, offset $\Delta\omega_1 = 0$ and Rabi $\omega_{1_1} = 0.5\ MHz$ is displayed in figure 3.3.

If we were to allow next for our system to evolve under the internal Hamiltonian for a time τ, the indexing of our coefficients and basis functions would have to be modified according to table 3.1. If after that we wanted to apply another time-independent pulse with a different Rabi frequency and offset, we would use again table 3.2. Such transformations would occur as follows,

$$
\begin{aligned}
|A^0_{z,0}|\sin(\varphi^0_{z,0})\hat{z} &\xrightarrow{n=1} 2|A^1_0|e^{i\varphi^1_0} + |A^1_{z,0}|\cos(\varphi^1_{z,0})\hat{z} \xrightarrow{H_{int}} \\
&\xrightarrow{H_{int}} 2|A^1_1|e^{i(\delta\omega\tau+\varphi^1_1)} + |A^1_{z,0}|\cos(\varphi^1_{z,0})\hat{z} \xrightarrow{n=2} \\
&\xrightarrow{n=2} 2|A^2_1|e^{i(\delta\omega\tau+\varphi^2_1)} + 2|A^2_{-1}|e^{i(-\delta\omega\tau+\varphi^2_{-1})} + 2|A^2_0|e^{i\varphi^2_0} + \\
&\quad + 2|A^2_{z,1}|\cos(\delta\omega\tau+\varphi^2_{z,1})\hat{z} + |A^2_{z,0}|\cos(\varphi^2_0)\hat{z}. \qquad (3.16)
\end{aligned}
$$

3.4 k-space grating and magnetization paths in the reciprocal space

The magnetization mixing between basis functions and their evolution due to the internal and control Hamiltonians can be better understood when represented as paths in a reciprocal space.

By considering the special case of fixed pulse spacing τ, we can define a 2D rectangular lattice $\boldsymbol{R} = n\boldsymbol{a} + m\boldsymbol{b}$, $n, m \in \mathbb{Z}$, with axial distances $|\boldsymbol{a}| = \tau$, $|\boldsymbol{b}| = 1$ and an axial angle of $\theta = \pi/2$ (see figure 3.4). In it we will draw the reciprocal paths describing the evolution of the magnetization.

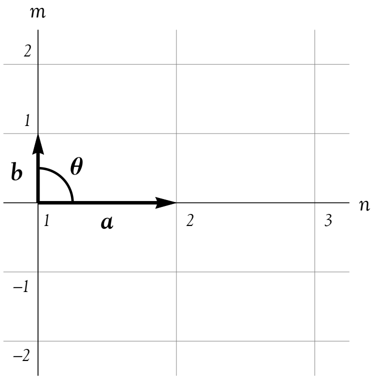

Figure 3.4: 2D rectangular lattice, with the lattice vectors $\boldsymbol{a}$ and $\boldsymbol{b}$ drawn.

The next step is to define the notion of a node in the reciprocal space.

Definition (node): A node in the lattice consists of an array composed by two integers, n and m, i.e. $\boldsymbol{N}_{n,m} = (n, m)$.

For the problem at hand, m corresponds to the wrapping number of the basis functions and n is a time-label associated to the number of pulses applied.

Through the definition of a node $\boldsymbol{N}_{n,m}$ we can introduce the notion of a reciprocal path.

Definition (path) : A path in the reciprocal space is defined as a string of nodes of the form

$$\boldsymbol{P}_{(m_1,m_2,\ldots,m_j,\ldots,m_n)} = \{\boldsymbol{N}_{1,m_1}, \boldsymbol{N}_{2,m_2}, \ldots, \boldsymbol{N}_{j,m_j}, \ldots, \boldsymbol{N}_{n,m_n}\} \qquad (3.17)$$

Not all paths in the reciprocal space describe paths that are physically possible. Only paths drawn employing table 3.1 and 3.2 describe the evolution of magnetization and thus, they receive the name of **magnetization paths**.

The origin of the magnetization paths for an initial state that does not depend on $\delta\omega$ is always the node $\boldsymbol{N}_{1,0}$. As described in 3.13, if one pulse is applied at $n = 1$, that generates two new coefficients, $A_0^1(\delta\omega)$ and $A_{z,0}^1(\delta\omega)$. Accordingly, two paths emerge from the node $\boldsymbol{N}_{1,0}$ (see figure 3.5 (a)), and if no more pulses are applied, they evolve according to 3.1,

$$\boldsymbol{P}_{(0,1,2,3)} = \{\boldsymbol{N}_{1,0}, \boldsymbol{N}_{2,1}, \boldsymbol{N}_{3,2}, \boldsymbol{N}_{4,3}\},$$
$$\boldsymbol{P}_{(0,0,0,0)} = \{\boldsymbol{N}_{1,0}, \boldsymbol{N}_{2,0}, \boldsymbol{N}_{3,0}, \boldsymbol{N}_{4,0}\}.$$

We can thus think of coefficients $A_0^1(\delta\omega)$ and $A_{z,0}^1(\delta\omega)$ as weights associated to the path **sections** between node $\boldsymbol{N}_{1,0}$ and nodes $\boldsymbol{N}_{2,1}$ and $\boldsymbol{N}_{2,0}$, respectively.

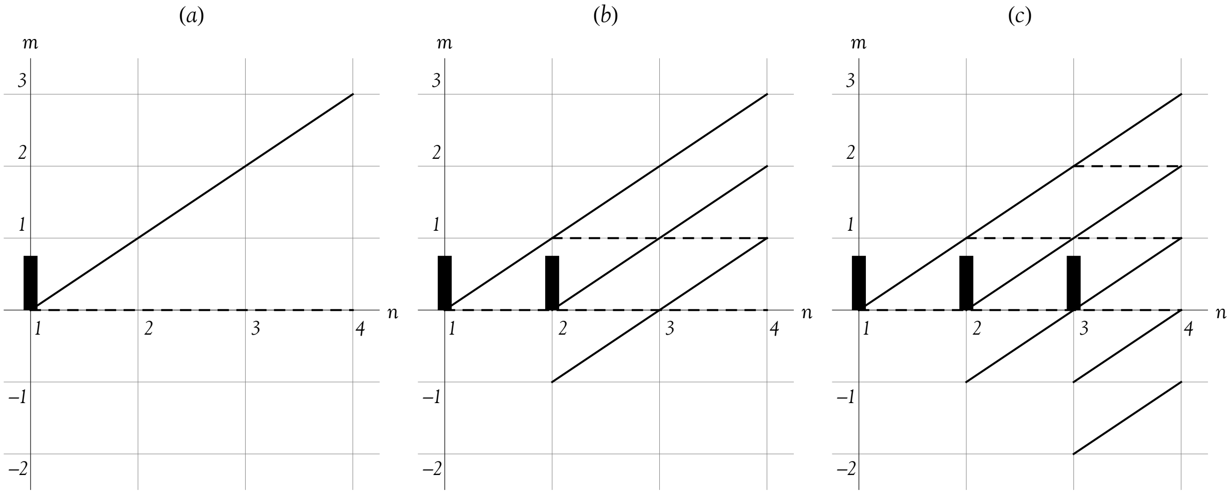

Figure 3.5: Subfigure (a) shows the k-space grating after applying just one pulse. Subfigure (b) is the k-space grating modified to account for a second pulse. Subfigure (c) shows a third pulse, which increases the number of paths and hence makes the k-space grating more complex.

It follows from table 3.1 that straight lines in the lattice with a slope of $1/\tau$ (solid lines in figure 3.5) contribute to the transverse magnetization, and horizontal lines (dashed black in figure 3.5), with their number m not affected by the action of the internal Hamiltonian, contribute to the longitudinal magnetization. For instance, in figure 3.5 (a), $\boldsymbol{P}_{(0,1,2,3)}$ is the only path contributing to the transverse magnetization and $\boldsymbol{P}_{(0,0,0,0)}$ is the only path contributing to the longitudinal magnetization.

If a second pulse is applied at $n = 2$, the simple k-space grating of figure 3.5 (a) becomes more complex (see figure 3.5 (b)). It follows from table 3.2 that three path branches associated to coefficients $A_1^2(\delta\omega)$, $A_{z,1}^2(\delta\omega)$ and $A_{-1}^2(\delta\omega)$ emerge from node $\boldsymbol{N}_{2,1}$, and two additional path directions with weight functions $A_0^2(\delta\omega)$ and $A_{z,0}^2(\delta\omega)$ originate from $\boldsymbol{N}_{2,0}$. That increases the total number of paths to five,

$$\begin{aligned}
\boldsymbol{P}_{(0,1,2,3)} &= \{\boldsymbol{N}_{1,0}, \boldsymbol{N}_{2,1}, \boldsymbol{N}_{3,2}, \boldsymbol{N}_{4,3}\},\\
\boldsymbol{P}_{(0,1,1,1)} &= \{\boldsymbol{N}_{1,0}, \boldsymbol{N}_{2,1}, \boldsymbol{N}_{3,1}, \boldsymbol{N}_{4,1}\},\\
\boldsymbol{P}_{(0,-1,0,1)} &= \{\boldsymbol{N}_{1,0}, \boldsymbol{N}_{2,-1}, \boldsymbol{N}_{3,0}, \boldsymbol{N}_{4,1}\},\\
\boldsymbol{P}_{(0,0,1,2)} &= \{\boldsymbol{N}_{1,0}, \boldsymbol{N}_{2,0}, \boldsymbol{N}_{3,1}, \boldsymbol{N}_{4,2}\},\\
\boldsymbol{P}_{(0,0,0,0)} &= \{\boldsymbol{N}_{1,0}, \boldsymbol{N}_{2,0}, \boldsymbol{N}_{3,0}, \boldsymbol{N}_{4,0}\}.
\end{aligned}$$

Finally, if a third pulse is applied (figure 3.5 (c)), new paths are added to the ones above and the total number of paths increases to thirteen. Namely,

$$\begin{aligned}
\boldsymbol{P}_{(0,1,2,3)} &= \{\boldsymbol{N}_{1,0}, \boldsymbol{N}_{2,1}, \boldsymbol{N}_{3,2}, \boldsymbol{N}_{4,3}\},\\
\boldsymbol{P}_{(0,1,2,2)} &= \{\boldsymbol{N}_{1,0}, \boldsymbol{N}_{2,1}, \boldsymbol{N}_{3,2}, \boldsymbol{N}_{4,2}\},\\
\boldsymbol{P}_{(0,1,-2,-1)} &= \{\boldsymbol{N}_{1,0}, \boldsymbol{N}_{2,1}, \boldsymbol{N}_{3,-2}, \boldsymbol{N}_{4,-1}\},\\
\boldsymbol{P}_{(0,1,1,2)} &= \{\boldsymbol{N}_{1,0}, \boldsymbol{N}_{2,1}, \boldsymbol{N}_{3,1}, \boldsymbol{N}_{4,1}\},\\
\boldsymbol{P}_{(0,1,1,1)} &= \{\boldsymbol{N}_{1,0}, \boldsymbol{N}_{2,1}, \boldsymbol{N}_{3,1}, \boldsymbol{N}_{4,1}\},\\
\boldsymbol{P}_{(0,1,-1,0)} &= \{\boldsymbol{N}_{1,0}, \boldsymbol{N}_{2,1}, \boldsymbol{N}_{3,1}, \boldsymbol{N}_{4,1}\},\\
\boldsymbol{P}_{(0,-1,0,1)} &= \{\boldsymbol{N}_{1,0}, \boldsymbol{N}_{2,-1}, \boldsymbol{N}_{3,0}, \boldsymbol{N}_{4,1}\},\\
\boldsymbol{P}_{(0,-1,0,0)} &= \{\boldsymbol{N}_{1,0}, \boldsymbol{N}_{2,-1}, \boldsymbol{N}_{3,0}, \boldsymbol{N}_{4,1}\},\\
\boldsymbol{P}_{(0,0,1,2)} &= \{\boldsymbol{N}_{1,0}, \boldsymbol{N}_{2,0}, \boldsymbol{N}_{3,1}, \boldsymbol{N}_{4,2}\},\\
\boldsymbol{P}_{(0,0,1,1)} &= \{\boldsymbol{N}_{1,0}, \boldsymbol{N}_{2,0}, \boldsymbol{N}_{3,1}, \boldsymbol{N}_{4,2}\},\\
\boldsymbol{P}_{(0,0,-1,0)} &= \{\boldsymbol{N}_{1,0}, \boldsymbol{N}_{2,0}, \boldsymbol{N}_{3,1}, \boldsymbol{N}_{4,2}\},\\
\boldsymbol{P}_{(0,0,0,1)} &= \{\boldsymbol{N}_{1,0}, \boldsymbol{N}_{2,0}, \boldsymbol{N}_{3,0}, \boldsymbol{N}_{4,0}\},\\
\boldsymbol{P}_{(0,0,0,0)} &= \{\boldsymbol{N}_{1,0}, \boldsymbol{N}_{2,0}, \boldsymbol{N}_{3,0}, \boldsymbol{N}_{4,0}\}.
\end{aligned}$$

Let us take a minute to discuss how the coefficients $A^n_m(\delta\omega)$ and $A^n_{z,m}(\delta\omega)$ relate to paths and how they do not. Generally, more than one path contribute to the value of a coefficient. Hence, it is a misrepresentation to talk of coefficients $A^n_m(\delta\omega)$ and $A^n_{z,m}(\delta\omega)$ as weight functions associated to paths. Rather, we should think of them as functions associated to certain path sections. The reason behind that might not be easy to spot in the simpler cases of figures 3.5 (a) and (b) but it becomes more evident in 3.5 (c). Indeed, for figure 3.5 (a) one would be correct to associate $A^1_0(\delta\omega)$ to path $\boldsymbol{P}_{(0,1,2,3)}$. Or in the case of figure 3.5 (b), to think of $A^2_{-1}(\delta\omega)$ as a weight associated to path $\boldsymbol{P}_{(0,-1,0,1)}$. However, this reasoning starts to crumble in more complex k-space gratings such as the one represented in figure 3.5 (c). At $n = 3$, unlike in figures (a) and (b), more than one path (in this case, two) merge into nodes $\boldsymbol{N}_{3,1}$ and $\boldsymbol{N}_{3,0}$. Thus, to which path do coefficients $A_1^3(\delta\omega)$ and $A_{z,1}^3(\delta\omega)$ act as weight functions for? Path $\boldsymbol{P}_{(0,1,1,2)}$, $\boldsymbol{P}_{(0,1,1,1)}$, $\boldsymbol{P}_{(0,0,1,2)}$ or $\boldsymbol{P}_{(0,0,1,1)}$? These are questions that cannot be answered because their formulation is inherently wrong. Coefficients $A_m^n(\delta\omega)$ and $A_{z,m}^n(\delta\omega)$ are not weight functions of paths, but they do allow us to fully describe the $\delta\omega$ dependent magnetization at any time. Indeed, note how after the third pulse, the decomposition in basis functions of the transverse and longitudinal magnetizations require only eight coefficients but the k-space grating has, in total, thirteen paths.

To fully appreciate the level of intricacy a k-space grating can achieve, let us consider the example sketched in figure 3.6. For an uncorrelated initial state, we considered a sequence of six evenly-spaced pulses of length t_p with arbitrary Rabi frequencies and offsets. The arbitrariness in the amplitudes of the pulses is not explicit in any of the images in this section. The reason is to emphasize that, even though the values of the Rabi frequency, pulse length and offset $\Delta\omega$ directly affect the coefficients $A_m^n(\delta\omega)$ and $A_{z,m}^n(\delta\omega)$, they play no role in drawing the grating.

The sum over all the paths in black in figure 3.6 yields the magnetization at time $T = 6t_p + 5\tau$. Namely,

$$M_{long}(T;\delta\omega) = \mathrm{Re}\left[\sum_{m=0}^{5} A_{z,m}^6(\delta\omega)e^{im\tau\delta\omega}\right] \tag{3.18}$$

$$M_{trans}(T;\delta\omega) = \sum_{m=-5}^{5} A_m^6(\delta\omega)e^{im\tau\delta\omega} \tag{3.19}$$

where the set of coefficients $\{A_m^6\}$ and $\{A_{z,|m|}^6\}$, for $m = -5, -4, \ldots,\ -1, 0, 1, \ldots, 4, 5$ depend on all the previous coefficients, as seen in table 3.2. They thus fully characterize the map for the magnetization at time T.

In dashed grey we have extended the negative pitched paths for times larger than T to highlight that when negative trajectories cross the $m = 0$ horizontal axis, an echo forms due to the partial refocusing of the magnetization. In particular, for a sequence with the characteristics described above, five echos of varying intensities will form.

One might notice that, when a pulse is applied at some n and different paths branch out of the nodes $\mathbf{N}_{n,m}$ for $-(n-1) \leq m \leq n-1$, the associated coefficients $A_m^n(\delta\omega)$ and $A_{z,m}^n(\delta\omega)$ depend on previous functions $A_m^{n-1}(\delta\omega)$ and $A_{z,m}^{n-1}(\delta\omega)$. It can thus be shown by simple but lengthy algebraic calculations (see appendix [??]) that two coupled recursive expressions relate the two sets of functions.

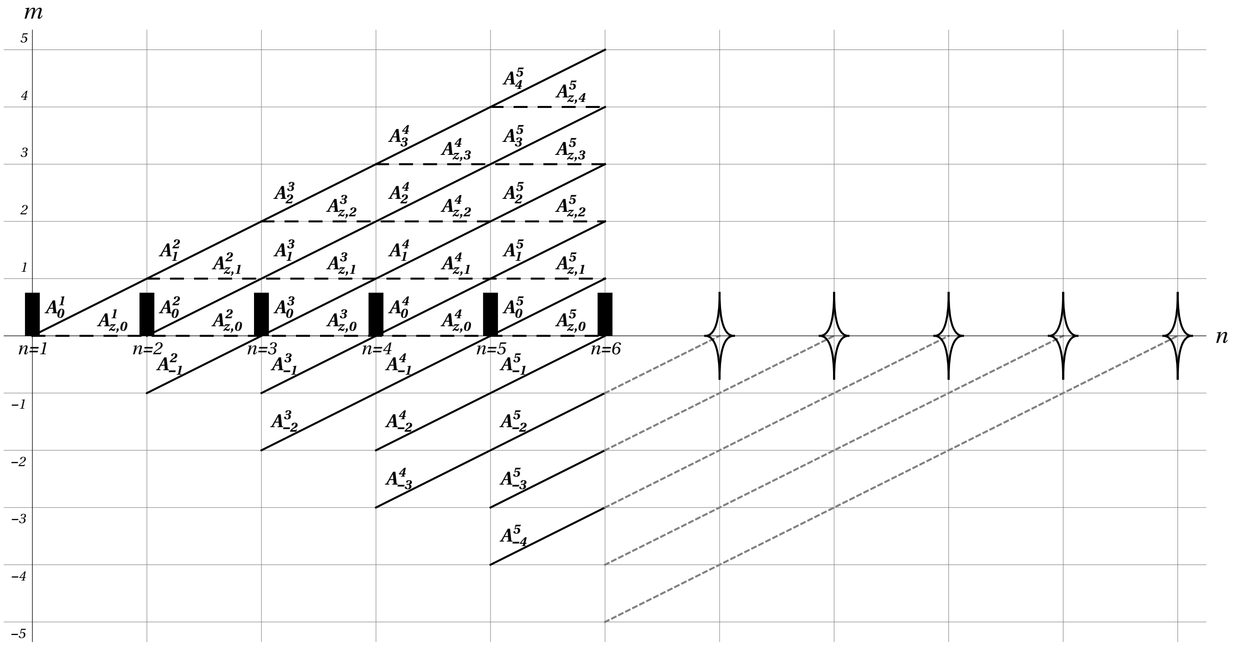

Figure 3.6: Representation of the evolution of the magnetization as paths in the reciprocal space. The horizontal axis corresponds to time (or number n), the vertical axis is the wrapping number of the basis functions m. Each pulse (represented as a black rectangle) has the same length t_p and is separated from the next one by a time τ. We allow each pulse to have a different Rabi frequency and offset even though we have not specifically showed it in the graphic. In solid black we draw the trajectories contributing to the transverse magnetization all the way up to the last applied pulse ($n = 6$) at time T. In black dashed lines, we draw the paths contributing to the longitudinal magnetization. In dashed grey, we have extended the transverse paths with negative pitch to show where the echo formations will occur. We have written on top of each path section the weight function associated to the new path branch.

3.5 Recursive formulas

In this section we present the two coupled recursive formulas for the set of coefficients $\{A^n_m(\delta\omega)\}$ and $\{A^n_{z,m}(\delta\omega)\}$ given uncorrelated initial states $\rho_0 = \sigma_Z$, $\rho_0 = \sigma_X$, and $\rho_0 = \sigma_Y$. Let us first define some useful parameters to write down the equations,

$$\delta_m = \begin{cases} 1, \text{ if } m = 0 \\ 0, \text{ if } m \neq 0 \end{cases} \qquad \epsilon_m = 1 + \delta_m \qquad \kappa_m = 1 - \delta_m$$

$$\theta_m = \begin{cases} 1, \text{ if } m > 0 \\ 1/2, \text{ if } m = 0 \\ 0, \text{ if } m < 0 \end{cases} \qquad f_m^n = \kappa_m^{-\frac{(-1)^n-1}{2}} \qquad g_m^n = \kappa_m^{\frac{(-1)^n+1}{2}}$$

Now, if the initial state is $\rho_0 = \sigma_Z$,

$$\boldsymbol{A^{0}_{m}} = 0,\ \forall m,\ \ \boldsymbol{A^{0}_{z,m}} = \delta_m,\ \forall m, \tag{3.20}$$

$$\begin{aligned} \boldsymbol{A^{n}_{m}} &= |T_n| e^{i\phi_{T_n}}\ \boldsymbol{A^{n-1}_{m-1}} + \sin^2\frac{\alpha_n}{2}\cos^2\Delta_n\ \left(\boldsymbol{A^{n-1}_{-m-1}}\right)^* \\ &- i|L_n|\cos\Delta_n e^{i\phi_{L_n}}\Big(\theta_m\ \boldsymbol{A^{n-1}_{z,|m|}} + (1-\theta_m)\big(\boldsymbol{A^{n-1}_{z,|m|}}\big)^*\Big)\frac{\epsilon_m}{2},\ \text{for } n \geq 1 \text{ and } \forall m, \end{aligned} \tag{3.21}$$

$$\begin{aligned} \boldsymbol{A^{n}_{z,m}} &= \big(\cos\alpha_n\cos^2\Delta_n + \sin^2\Delta_n\big)\ \boldsymbol{A^{n-1}_{z,m}} - i|L_n|\cos\Delta_n e^{i\phi_{L_n}}\ \boldsymbol{A^{n-1}_{m-1}}\ f^n_m \\ &- \big(i|L_n|\cos\Delta_n e^{i\phi_{L_n}}\big)^*\ \big(\boldsymbol{A^{n-1}_{-m-1}}\big)^* g^n_m,\ \text{for } n \geq 1 \text{ and } \forall m. \end{aligned} \tag{3.22}$$

If the initial state is $\rho_0 = \sigma_X$,

$$\boldsymbol{A^{0}_{m}} = \delta_m,\ \forall m,\ \ \boldsymbol{A^{0}_{z,m}} = 0,\ \forall m, \tag{3.23}$$

$$\boldsymbol{A^{1}_{m}} = |T_1| e^{i\phi_{T_1}}\ \boldsymbol{A^{0}_{m}} + \sin^2\frac{\alpha_1}{2}\cos^2\Delta_1\ (\boldsymbol{A^{0}_{m}})^*,\ \forall m, \tag{3.24}$$

$$\boldsymbol{A^{1}_{z,m}} = -i|L_1|\cos\Delta_1 e^{i\phi_{L_1}}\ \boldsymbol{A^{0}_{m}},\ \forall m, \tag{3.25}$$

$$\begin{aligned} \boldsymbol{A^{n}_{m}} &= |T_n| e^{i\phi_{T_n}}\ \boldsymbol{A^{n-1}_{m-1}} + \sin^2\frac{\alpha_n}{2}\cos^2\Delta_n\ \left(\boldsymbol{A^{n-1}_{-m-1}}\right)^*, \\ &- i|L_n|\cos\Delta_n e^{i\phi_{L_n}}\Big(\theta_m\ \boldsymbol{A^{n-1}_{z,|m|}} + (1-\theta_m)\big(\boldsymbol{A^{n-1}_{z,|m|}}\big)^*\Big)\frac{\epsilon_m}{2},\ \text{for } n \geq 2 \text{ and } \forall m, \end{aligned} \tag{3.26}$$

$$\begin{aligned} \boldsymbol{A^{n}_{z,m}} &= \big(\cos\alpha_n\cos^2\Delta_n + \sin^2\Delta_n\big)\ \boldsymbol{A^{n-1}_{z,m}} - i|L_n|\cos\Delta_n e^{i\phi_{L_n}}\ \boldsymbol{A^{n-1}_{m-1}}\ f^n_m \\ &- \big(i|L_n|\cos\Delta_n e^{i\phi_{L_n}}\big)^*\ \big(\boldsymbol{A^{n-1}_{-m-1}}\big)^* g^n_m,\ \text{for } n \geq 2 \text{ and } \forall m. \end{aligned} \tag{3.27}$$

Finally, if the initial state is $\rho_0 = \sigma_Y$,

$$\boldsymbol{A^{0}_{m}} = i\delta_m,\ \forall m,\ \ \boldsymbol{A^{0}_{z,m}} = 0,\ \forall m, \tag{3.28}$$

$$\boldsymbol{A^{1}_{m}} = |T_1| e^{i\phi_{T_1}}\ \boldsymbol{A^{0}_{m}} + \sin^2\frac{\alpha_1}{2}\cos^2\Delta_1\ (\boldsymbol{A^{0}_{m}})^*,\ \forall m, \tag{3.29}$$

$$\boldsymbol{A^{1}_{z,m}} = -i|L_1|\cos\Delta_1 e^{i\phi_{L_1}}\ \boldsymbol{A^{0}_{m}},\ \forall m, \tag{3.30}$$

$$\begin{aligned} \boldsymbol{A^{n}_{m}} &= |T_n| e^{i\phi_{T_n}}\ \boldsymbol{A^{n-1}_{m-1}} + \sin^2\frac{\alpha_n}{2}\cos^2\Delta_n\ \left(\boldsymbol{A^{n-1}_{-m-1}}\right)^* \\ &- i|L_n|\cos\Delta_n e^{i\phi_{L_n}}\Big(\theta_m\ \boldsymbol{A^{n-1}_{z,|m|}} + (1-\theta_m)\big(\boldsymbol{A^{n-1}_{z,|m|}}\big)^*\Big)\frac{\epsilon_m}{2},\ \text{for } n \geq 2 \text{ and } \forall m, \end{aligned} \tag{3.31}$$

$$\begin{aligned} \boldsymbol{A^{n}_{z,m}} &= \big(\cos\alpha_n\cos^2\Delta_n + \sin^2\Delta_n\big)\ \boldsymbol{A^{n-1}_{z,m}} - i|L_n|\cos\Delta_n e^{i\phi_{L_n}}\ \boldsymbol{A^{n-1}_{m-1}}\ f^n_m \\ &- \big(i|L_n|\cos\Delta_n e^{i\phi_{L_n}}\big)^*\ \big(\boldsymbol{A^{n-1}_{-m-1}}\big)^* g^n_m,\ \text{for } n \geq 2 \text{ and } \forall m. \end{aligned} \tag{3.32}$$

Note how for $n \geq 2$, all coefficients obey the same recursive formula independently of the initial state. The difference in initial state is manifested through the recursive definitions of the initial coefficients $\{A_m^0\}$, $\forall m$ and $\{A_m^1\}$, $\forall m$.

Such sets of coupled recursive formulas allow us to compute coefficients $A_m^n(\delta\omega)$ and $A_{z,m}^n(\delta\omega)$ more effectively for an arbitrarily large number of pulses n given a previous knowledge of coefficients $A_m^{n-1}(\delta\omega)$ and $A_{z,m}^{n-1}(\delta\omega)$.

3.6 Analysis of continuous pulses

Even though this formalism has been introduced as an analytical description of the response of evenly-spaced rectangular pulses, we can use it to also describe continuous sequences.

To do so, we first set all time intervals between pulses to zero, i.e., $\tau = 0$. The control pulses become then a series of n rectangular pulses back to back, each of length t_p (see figure 3.7 (a) and (b)). The magnetization at time $t = n \cdot t_p$ can thus be written as,

$$M_{trans}(t; \delta\omega) = \sum_{m=-n+1}^{n-1} A_m^n(\delta\omega), \tag{3.33}$$

and

$$M_{long}(t; \delta\omega) = \mathrm{Re}\left[\sum_{m=0}^{n-1} A_{z,m}^n(\delta\omega)\right]. \tag{3.34}$$

If the length of these rectangular pulses t_p is small enough, it describes continuous sequences with sufficient accuracy. Not surprisingly, time discretization is an essential tool in the simulation of continuous pulses based on Hamiltonian dynamics, since it avoids the evaluation of time-ordered exponentials.

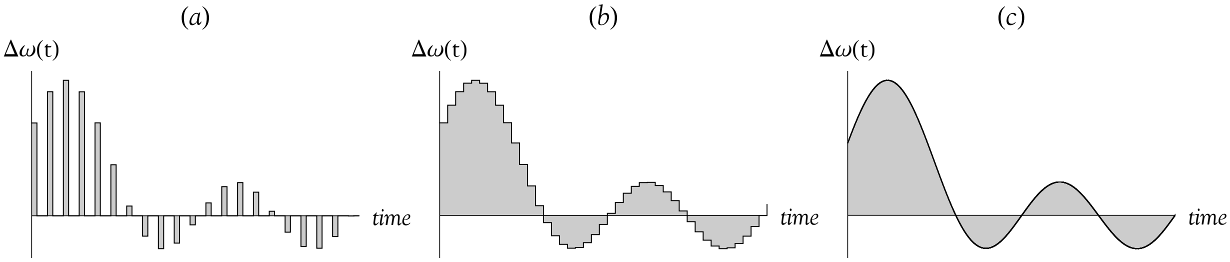

Figure 3.7: Subplot (a) shows a series of evenly-spaced rectangular pulses. Subplot (b) is (a) when setting $\tau = 0$. Subplot (c) shows (b) after taking the limit of t_p tending to zero.

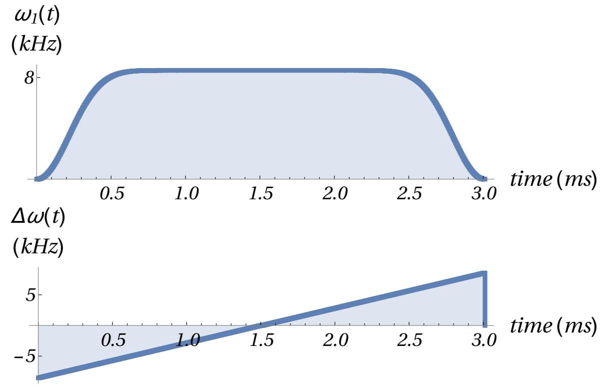

Figure 3.8: Pulse profile for the x and z control fields of a WURST pulse.

We can use the WURST sequence as an example of how the discretization of pulses into steps of length t_p allows us to compute their response. For a WURST pulse of 3ms, we discretize it with a time-step of 6μs. The resulting pulses are depicted in figure 3.8.

By then computing all the coefficients $A^n_m(\delta\omega)$ and $A^n_{z,m}(\delta\omega)$ for each time-step and each isochromat employing the recursive equations in 3.21 and 3.22, we obtain the frequency profile of figure 3.9 at time $T = 3$ms.

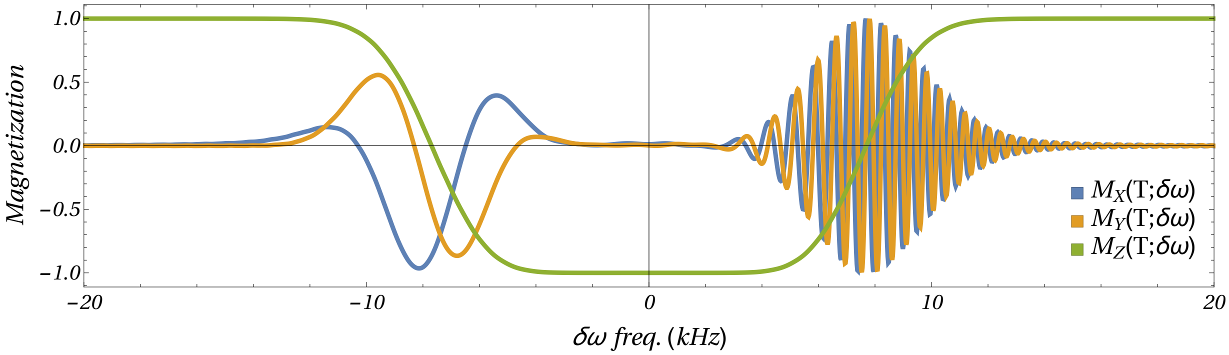

Figure 3.9: In blue, yellow and green the expectation values for observables σ_X, σ_Y and σ_Z, respectively.

Once τ has been set to zero, we can go a bit further and consider the limit of t_p approaching zero (figure 3.7 (c)). Taking the limit of $t_p \to 0$ is equivalent to computing the limit of the nominal nutation angle α_{0_n} approaching zero $\forall n$, since $\alpha_{0_n} = \omega_{1_n} t_p$ (note that ω_{1_n} is finite). Computing this limit allows us to give a complete and rigorous analysis of the response of our system under continuous pulses.

The first step towards achieving this goal is to write the Taylor series of each basis transformation up to the smallest order in α_{0_n} (see table 3.3).

Notation L, T_+, and T_- stand for longitudinal basis function, transverse basis function with positive pitch (right-handed helix), and transverse basis function with negative pitch (left-handed helix). Hence, a term such as $(L \to T_-)$ represents a transformation from a longitudinal basis function to a transverse basis function with negative pitch. Terms $(T_\pm \to T_\pm)_n$ and $(T_\pm \to T_\mp)_n$ correspond to cases when the sign of the winding number either stays invariant or flips.

$(L \to L)_n$	$=$	$\cos\alpha_n \cos^2\Delta_n + \sin^2\Delta_n$	$\sim$	1
$(L \to T_+)_n$	$=$	$-\frac{1}{2}\lvert L_n\rvert \cos\Delta_n e^{i\phi_{L_n}}$	$\sim$	$-\frac{1}{2}\alpha_{0_n}$
$(L \to T_-)_n$	$=$	$\frac{1}{2}\lvert L_n\rvert \cos\Delta_n e^{i\phi_{L_n}} e^{i\boldsymbol{P}}$	$\sim$	$\frac{1}{2}\alpha_{0_n} e^{i\boldsymbol{P}}$
$(T_\pm \to T_\pm)_n$	$=$	$\lvert T_{r_n}\rvert e^{i\phi_{T_{r_n}}}$	$\sim$	$e^{i\phi_{T_{r_n}}}$
$(T_\pm \to T_\mp)_n$	$=$	$\sin^2\frac{\alpha_n}{2}\cos^2\Delta_n$	$\sim$	$\frac{1}{4}\alpha_{0_n}^2 e^{i\boldsymbol{P}}$
$(T_+ \to L)_n$	$=$	$\lvert L_n\rvert \cos\Delta_n e^{i\phi_{L_n}}$	$\sim$	α_{0_n}
$(T_- \to L)_n$	$=$	$-\lvert L_n\rvert \cos\Delta_n e^{i\phi_{L_n}} e^{i\boldsymbol{P}}$	$\sim$	$-\alpha_{0_n} e^{i\boldsymbol{P}}$

Table 3.3: Basis transformations to the smallest order in t_p.

This might be new notation, but it is simply another way of representing the results displayed in table 3.2. In addition, in the third column of table 3.3 we present the Taylor expansion up to the smallest order in t_p of all the transformation terms, with the exception of $(T_\pm \to T_\pm)_n$. In that instance, we expanded its modulus $|T_{r_n}|$ and phase ϕ_{T_n}, keeping the exponential form. Namely,

$$(T_\pm \to T_\pm)_n = |T_{r_n}| e^{i\phi_{T_{r_n}}} \sim \left(1 - \frac{1}{4}\alpha_{0_n}^2\right) e^{i\phi_{T_{r_n}}} \sim e^{i\phi_{T_{r_n}}}, \tag{3.35}$$

and

$$\phi_{T_{r_n}} \sim \phi_{T_{r_n}} = (\delta\omega - \Delta\omega_n)\, t_p. \tag{3.36}$$

For convenience, we kept the symbol $\phi_{T_{r_n}}$ to denote the approximated phase $(\delta\omega - \Delta\omega_n)\, t_p$. Furthermore, we introduce the operator $e^{i\boldsymbol{P}}$ in table 3.3 to account for the sign change in the wrapping number m for transformations $(T_- \to L)_n$, $(L \to T_-)_n$ and $(T_\pm \to T_\mp)$.

By inspection of table 3.3 we easily notice that basis transformations from the longitudinal axis to the transverse plane and vice-versa are first order in α_{0_n}. Similarly, changing the pitch sign for transverse basis functions comes with an $\alpha_{0_n}^2$ cost. Finally, the smallest order for staying invariant under the action of any pulse is zero (i.e., 1 or multiplicative factor $e^{i\phi_{T_{r_n}}}$, which if expanded its smallest order is still zeroth).

Since we are taking the limit of t_p tending to zero, we will only consider transformations up to first order and discard the second order transformation $(T_\pm \to T_\mp)_n$. Thus, an infinitely short pulse either:

- Modifies the trajectory of our paths from the longitudinal axis to the transverse plane or vice-versa to first order in α_{0_n}.
- Leaves the trajectory unchanged, with a multiplicative factor of either 1 or $e^{i\phi_{T_n}}$

Through these observations we can define some useful concepts, such as kth order paths, kth order path sum and kth order magnetization contribution. This concepts will help us identify which paths contribute (and how much) to the transverse and longitudinal magnetization.

Definition (kth order path): path in the reciprocal space to which k pulses have affected its trajectory and thus carries a $\alpha_{0_n}^k$ weight.

Figure 3.10 helps visualize what a kth order path is: every time a path changes trajectory due to the action of a pulse, it acquires an additional order in α_{0_n}. Moreover, due to the geometry of the k-space grating and the restriction in path trajectories, only odd paths can contribute to the transverse magnetization and only even paths can contribute to the longitudinal.

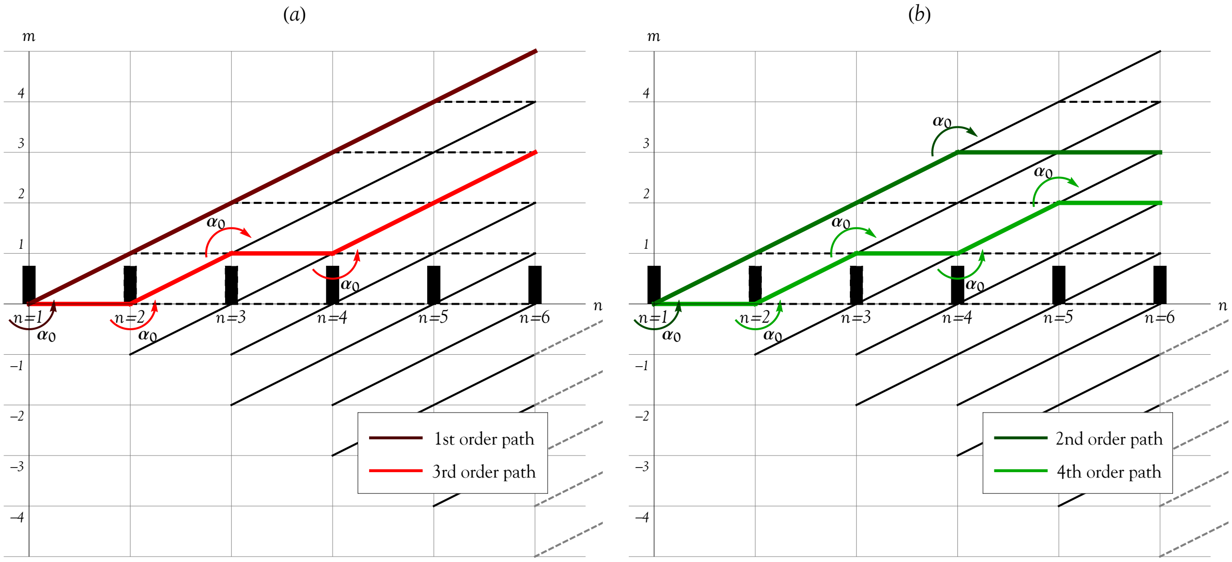

Figure 3.10: (a) Odd order paths contributing to the transverse magnetization at time $T = 6t_p$ are depicted in red. In dark red a first order path, in light red, a third order path. (b) Even order paths in green contribute to the longitudinal magnetization at time $T = 6t_p$. In dark green, second order path, and in light green, forth order path. Note we have kept the distance τ between pulses for visualization purposes only. For the whole of this section, $\tau = 0$.

Definition (kth order path sum): sum over all the kth order paths in a k-space grating, denoted as $\mathcal{S}^k(t; \delta\omega)$.

Definition (kth order magnetization contribution): limit of a kth order path sum $\mathcal{S}^k(t; \delta\omega)$ for t_p approaching zero, i.e. $\mathcal{M}^k(t; \delta\omega) = \lim_{t_p \to 0} \mathcal{S}^k(t; \delta\omega)$.

In turn, summing over all kth order magnetization contributions gives us the complete response of the system at time t,

$$M_{trans}(t;\delta\omega) = \sum_{i=1}^{\infty} \mathcal{M}^{(2i-1)}(t;\delta\omega), \tag{3.37}$$

and

$$M_{long}(t;\delta\omega) = \sum_{i=1}^{\infty} \mathcal{M}^{(2i)}(t;\delta\omega). \tag{3.38}$$

We can give an example of this for the case of $\boldsymbol{M} = M_0\hat{z}$, with $M_0 = 1$ (that is, initial state fully polarized along the longitudinal axis). The first order path sum $\mathcal{S}^1(t;\delta\omega)$ after applying $n = t/t_p$ pulses is,

$$\mathcal{S}^1(t;\delta\omega) = \sum_{j=1}^{n} \left(i \left[\prod_{r=1}^{j-1} (L \to L)_r \right] \left[(L \to T_+)_j + (L \to T_-)_j \right] \left[\prod_{\ell=j+1}^{n} (T_\pm \to T_\pm)_\ell \right] \right), \tag{3.39}$$

with j indexing over the nodes $\boldsymbol{N}_{j,0}$, where the longitudinal magnetization nutates to the transverse plane.

By substituting the first order Taylor approximations of table 3.3 to equation 3.39 we obtain,

$$\begin{aligned} \mathcal{S}^1(t;\delta\omega) &= \sum_{j=1}^{n} \left(\left[\prod_{r=1}^{j-1} 1 \right] \left[-i\frac{1}{2}\alpha_{0_j} + i\frac{1}{2}\alpha_{0_j} e^{i\boldsymbol{P}} \right] \left[\prod_{\ell=j+1}^{n} e^{i\phi_{T_{r_\ell}}} \right] \right) = \\ &= -i \sum_{j=1}^{n} \left(\omega_{1_j} t_p \exp\left[i \sum_{\ell=j+1}^{n} (\delta\omega - \Delta\omega_\ell) t_p \right] \right). \end{aligned} \tag{3.40}$$

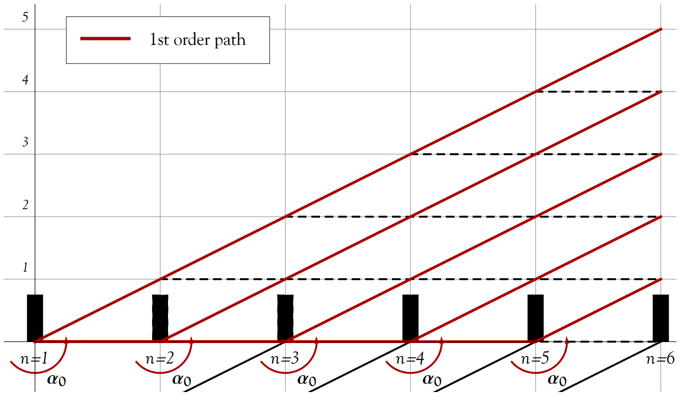

Figure 3.11: First order paths in dark red for a sequence of six pulses. The distance τ between pulses has been kept for visualization convenience.

If now we take the limit of t_p tending to zero,

$$\begin{aligned} \mathcal{M}^1_{trans}(t;\delta\omega) &= \lim_{t_p \to 0} \mathcal{S}^1(t;\delta\omega) = \\ &= -i \int_0^t \omega_1(t_1)\; e^{i(\phi(t)-\phi(t_1))}\; dt_1 = \\ &= -i e^{i\delta\omega t} \int_0^t \omega_1(t_1) e^{-i\int_{t_1}^{t} \Delta\omega(\tau) d\tau} e^{-i\delta\omega t_1} dt_1, \end{aligned} \tag{3.41}$$

with $\phi(t_a) - \phi(t_b) = \int_{t_b}^{t_a} (\delta\omega - \Delta\omega(\tau)) d\tau$, we retrieve the linear response theory (the Fourier transform of the pulse).

Even though linear response theory is a good approximation in the case of weak control pulses (see figure 3.12 (a)), it easily breaks down as stronger Rabi frequencies or longer pulses are considered (see figure 3.12 (b)). The reason behind this is the number of higher-order paths.

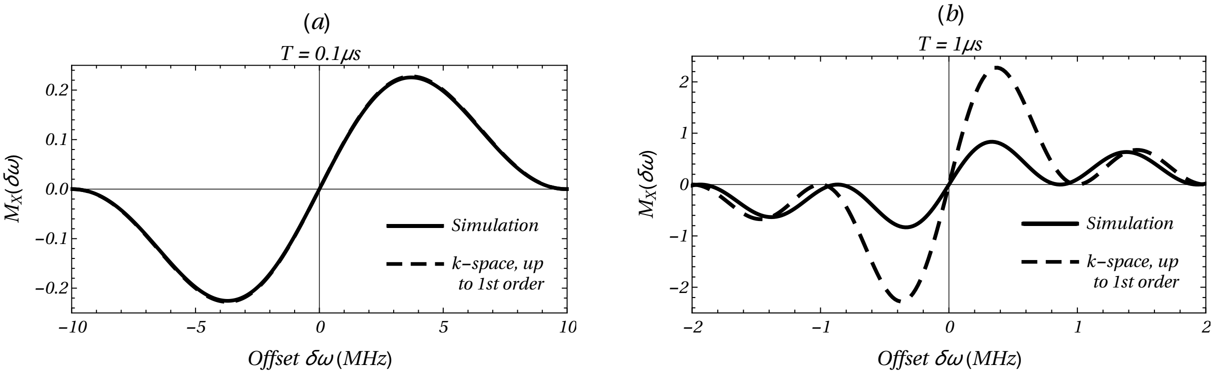

Figure 3.12: Both (a) and (b) are plots of the function $M_X(\delta\omega)$ for a rectangular pulse applied along the x-axis, with a Rabi $\omega_1 = 0.5$ MHz and with zero offset $\Delta\omega(t) = 0$. The difference is in the pulse length, of 0.1 μs in (a) and of 1 μs in (b). The solid lines represent data obtained by simulating the complete Hamiltonian dynamics and the dashed lines correspond to the linear response theory approximation.

path order	number of paths
*1*st	$\binom{n}{1}$
*3*rd	$\binom{n}{3}$
*5*th	$\binom{n}{5}$
⋮	⋮
kth	$\binom{n}{k}$

Table 3.4: Table counting the number of first, third, fifth and k*th* order paths in a k-space grating when applying n pulses.

Whereas the contribution of **one** higher-order path might be negligible compared to the contribution of **one** first order path, the **number** of higher-order paths is much larger than of first order paths. Consequently, for some pulses, higher-order paths amount to a significant contribution to the magnetization. In table 3.4 we present how many paths of first, third, fifth and in general, k*th* order are present in a grating of n pulses. Not surprisingly, the number of k*th* order paths is a k-combination of a set with n elements, $C(n, k)$.

After establishing the importance of higher-order paths to the total magnetization, let us derive an expression for higher-order magnetization contributions. We will start with the third and fifth order magnetization contributions, i.e. $\mathcal{M}^3_{trans}(T;\delta\omega)$ and $\mathcal{M}^5_{trans}(T;\delta\omega)$. Once those have been derived, we will try to extrapolate and give a general form for $\mathcal{M}^k_{trans}(T;\delta\omega)$.

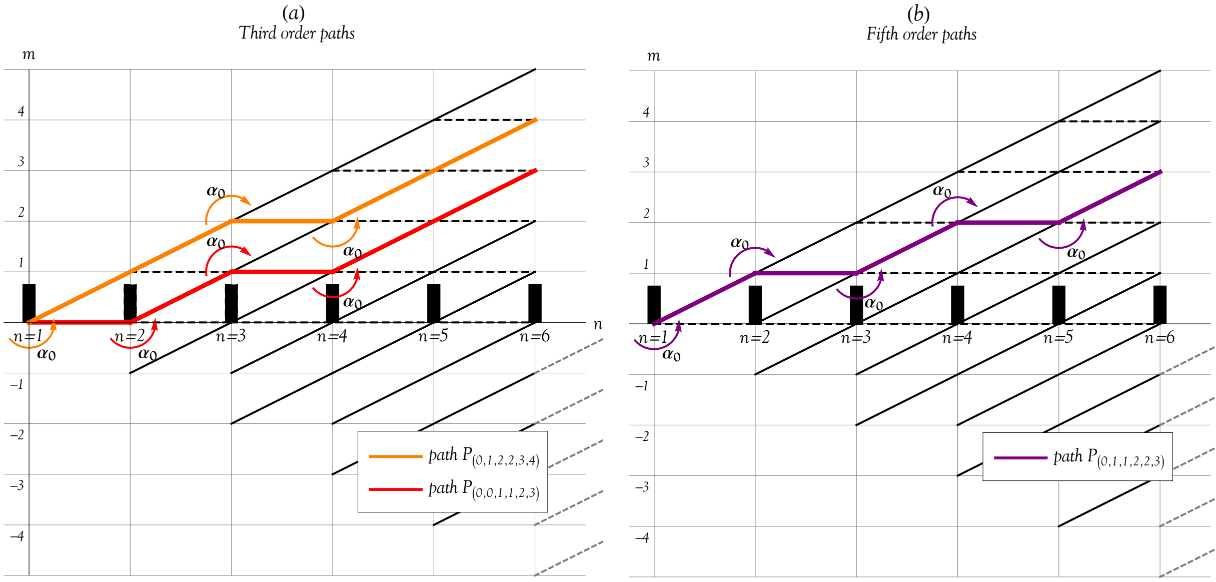

Figure 3.13: Figures (a) and (b) show the same k-space gratings. In (a) we highlight two different third order paths and in (b) a fifth order path.

As before, the first step is to sum over all third order paths (some examples of third order paths are sketched in figure 3.13 (a)),

$$
\begin{aligned}
\mathcal{S}^3(t;\delta\omega) &= \sum_{j=1}^{n}\sum_{m=j+1}^{n}\sum_{p=m+1}^{n}\left(i\left[\prod_{r=1}^{j-1}(L\to L)_r\right]\left[(L\to T_+)_j+(L\to T_-)_j\right]\cdot\right.\\
&\quad\cdot\left[\prod_{\ell=j+1}^{m-1}(T_\pm\to T_\pm)_\ell\right](T_+\to L)_m\left[\prod_{q=m+1}^{p-1}(L\to L)_q\right]\cdot\\
&\quad\left.\cdot\left[(L\to T_+)_p+(L\to T_-)_p\right]\left[\prod_{t=p+1}^{n}(T_\pm\to T_\pm)_t\right]\right)=\\
&=\sum_{j=1}^{n}\sum_{m=j+1}^{n}\sum_{p=m+1}^{n}\left(\left[\prod_{r=1}^{j-1}1\right](-i\alpha_{0_j})\left[\prod_{\ell=j+1}^{m-1}e^{i\phi_{T_{r_\ell}}}\right]\alpha_{0_m}\left[\prod_{q=m+1}^{p-1}1\right]\cdot\right.\\
&\quad\left.\cdot\left[-\frac{1}{2}\alpha_{0_p}+\frac{1}{2}\alpha_{0_p}e^{i\boldsymbol{P}}\right]\left[\prod_{t=p+1}^{n}e^{i\phi_{T_{r_t}}}\right]\right)=\\
&=i\sum_{j=1}^{n}\alpha_{0_j}\sum_{m=j+1}^{n}\alpha_{0_m}\cos\left(\sum_{\ell=j+1}^{m-1}\phi_{T_{r_\ell}}\right)\sum_{p=m+1}^{n}\alpha_{0_p}\exp\left(i\sum_{t=p+1}^{n}\phi_{T_{r_t}}\right),
\end{aligned}
\tag{3.42}
$$

and then take the limit of t_p approaching zero,

$$\begin{aligned} &\mathcal{M}^3(t;\delta\omega) = \lim_{t_p\to 0} \mathcal{S}^3(t;\delta\omega) = \\ &= i\int_0^t\int_{t_1}^t\int_{t_2}^t \omega_1(t_1)\;\omega_1(t_2)\;\cos\big(\phi(t_2)-\phi(t_1)\big)\;\omega_1(t_3)\;e^{i(\phi(t)-\phi(t_3))}dt_3\;dt_2\;dt_1 \end{aligned} \tag{3.43}$$

with $\phi(t_a)-\phi(t_b)=\int_{t_b}^{t_a}(\delta\omega-\Delta\omega(\tau))d\tau$.

Reproducing the analysis above for the fifth order term is a bit trickier but it can be done by introducing the following Heaviside function,

$$\theta[\kappa-p+j-m] = \begin{cases} 1, & \text{if } \kappa-p+j-m\geq 0 \\ 0, & \text{if } \kappa-p+j-m< 0 \end{cases} \tag{3.44}$$

which counts the position in the n axis when the transverse paths with negative pitch become positive.

Then,

$$\begin{aligned} \mathcal{S}^5_{trans}(t;\delta\omega) = &\sum_{j=1}^{n}\sum_{m=j+1}^{n}\sum_{p=m+1}^{n}\sum_{\kappa=p+1}^{n}\sum_{s=\kappa+1}^{n}\Bigg(i\Bigg[\prod_{r=1}^{j-1}(L\to L)_r\Bigg]\Bigg[(L\to T_+)_j+ \\ &+(L\to T_-)_j\Bigg]\Bigg[\prod_{\ell=j+1}^{m-1}(T_\pm\to T_\pm)_\ell\Bigg](T_+\to L)_m\Bigg[\prod_{q=m+1}^{p-1}(L\to L)_q\Bigg]\cdot \\ &\cdot\Bigg\{(L\to T_+)_p\Bigg[\prod_{t=p+1}^{\kappa-1}(T_\pm\to T_\pm)_t\Bigg](T_+\to L)_\kappa\Bigg[\prod_{x=\kappa+1}^{s-1}(L\to L)_x\Bigg]\cdot \\ &\cdot\Bigg[(L\to T_+)_s+(L\to T_-)_s\Bigg]\Bigg[\prod_{y=s+1}^{n}(T_\pm\to T_\pm)_y\Bigg]+ \\ &+(L\to T_-)_p\Bigg[\prod_{t=p+1}^{\kappa-1}(T_\pm\to T_\pm)_t\Bigg]\Bigg[(1-\theta[\kappa-p+j-m])(T_+\to L)_\kappa+ \\ &+\theta[\kappa-p+j-m](T_-\to L)_\kappa\Bigg]\Bigg[\prod_{x=\kappa+1}^{s-1}(L\to L)_x\Bigg]\Bigg[(L\to T_+)_s+ \\ &+(L\to T_-)_s\Bigg]\Bigg[\prod_{y=s+1}^{n}(T_\pm\to T_\pm)_y\Bigg]\Bigg\}\Bigg). \end{aligned} \tag{3.45}$$

After performing lengthy but straightforward calculations, expression 3.45 is simplified to,

$$\mathcal{S}^5(t;\delta\omega) = -i\sum_{j=1}^{n}\alpha_{0_j}\sum_{m=j+1}^{n}\alpha_{0_m}\cos\left(\sum_{\ell=j+1}^{m-1}\phi_{T_{r_\ell}}\right)\sum_{p=m+1}^{n}\alpha_{0_p}\cdot$$
$$\cdot\sum_{\kappa=p+1}^{n}\alpha_{0_\kappa}\cos\left(\sum_{t=p+1}^{\kappa-1}\phi_{T_{r_t}}\right)\sum_{s=\kappa+1}^{n}\alpha_{0_s}\exp\left(i\sum_{y=s+1}^{n}\phi_{T_{r_y}}\right) \tag{3.46}$$

Last but not least, we take the limit of t_p tending to zero, and obtain

$$\mathcal{M}^5(t;\delta\omega) = \lim_{t_p\to 0}\mathcal{S}^5(t;\delta\omega) =$$
$$-i\int_0^t\int_{t_1}^t\int_{t_2}^t\int_{t_3}^t\int_{t_4}^t \omega_1(t_1)\,\omega_1(t_2)\,\cos\big(\phi(t_2)-\phi(t_1)\big)\,\omega_1(t_3)\,\omega_1(t_4)\cdot$$
$$\cdot\cos\big(\phi(t_4)-\phi(t_3)\big)\,\omega_1(t_5)\,e^{i(\phi(t)-\phi(t_5))}dt_5\,dt_4\,dt_3\,dt_2\,dt_1, \tag{3.47}$$

where $\phi(t_a)-\phi(t_b) = \int_{t_b}^{t_a}(\delta\omega-\Delta\omega(\tau))d\tau$. With the knowledge provided by $\mathcal{M}^1(t;\delta\omega)$, $\mathcal{M}^3(t;\delta\omega)$, and $\mathcal{M}^5(t;\delta\omega)$ we can extrapolate an expression for $\mathcal{M}^k(t;\delta\omega)$,

$$\mathcal{M}^k(t;\delta\omega) = \lim_{t_p\to 0}\mathcal{S}^k(t;\delta\omega) =$$
$$= (-i)^k\int_0^t\!\!\cdots\int_{t_{k-1}}^t\left(\prod_{j=1}^{k}\omega_1(t_j)\right)\cos\left(\sum_{j=1}^{\frac{k-1}{2}}\big(\phi(t_{2j})-\phi(t_{2j-1})\big)\right)e^{i(\phi(t)-\phi(t_k))}dt_k\;\ldots\;dt_1, \tag{3.48}$$

where

$$\phi(t_{2j})-\phi(t_{2j-1}) = \int_{t_{2j-1}}^{t_{2j}}(\delta\omega-\Delta\omega(\tau))d\tau. \tag{3.49}$$

Then, given continuous pulses $p_X(t)=\omega_1(t)$ and $p_Z(t)=\Delta\omega(t)$, the transverse magnetization for any isochromat $\delta\omega$ as a function of time is,

$$M_{trans}(t;\delta\omega) = \sum_{i=1}^{\infty}\mathcal{M}^{(2i-1)}(t;\delta\omega) = \mathcal{M}^1(t;\delta\omega)+\mathcal{M}^3(t;\delta\omega)+\mathcal{M}^5(t;\delta\omega)+\cdots =$$
$$= \sum_{\substack{k=1\\k\ odd}}^{\infty}(-i)^k\int_0^t\!\!\cdots\int_{t_{k-1}}^t\left(\prod_{j=1}^{k}\omega_1(t_j)\right)\cos\left(\sum_{j=1}^{\frac{k-1}{2}}\big(\phi(t_{2j})-\phi(t_{2j-1})\big)\right)e^{i(\phi(t)-\phi(t_k))}dt_k\;\ldots\;dt_1, \tag{3.50}$$

Thus, in general, there is not an exact solution for the magnetization. Rather, the solution is an infinite sum of terms. However, if we truncate the infinite sum at any cutoff order κ_{cutoff}, we know the series is well behaved such that no magnetization is introduced.

That is, the infinite sum in 3.50 eventually converges to the exact result $M_{trans}(t;\delta\omega)$. Hence, for cutoff order κ_{cutoff}, the quantity

$$M_{trans}^{\kappa_{cutoff}}(t;\delta\omega) = \sum_{i=1}^{\kappa_{cutoff}} \mathcal{M}^{(2i-1)}(t;\delta\omega), \tag{3.51}$$

describes the complete response of our system, i.e. $M_{trans}^{\kappa_{cutoff}}(t;\delta\omega) \equiv M_{trans}(t;\delta\omega)$. In the case of figure 3.14, that cut-off order is $\kappa_{cutoff} = 9$.

In figure 3.14 we show in blue $M_Y(T;\delta\omega)$ obtained through the full simulation of the Hamiltonian dynamics for a rectangular pulse applied along the x-axis, of length $T = 1\mu$s, Rabi $\omega_1 = 0.5$MHz, and $\Delta\omega(t) = 0$. This is the same pulse whose response and first order approximation were presented in figure 3.12 (b). We compare it to the imaginary part of quantity 3.51 at time $t = T$, and for $\kappa_{cutoff} = 3,\ 5,\ 7$, and 9. Through this comparison we can appreciate how, for the particular case described above, a finite sum of nine orders is sufficient to describe the response of our system.

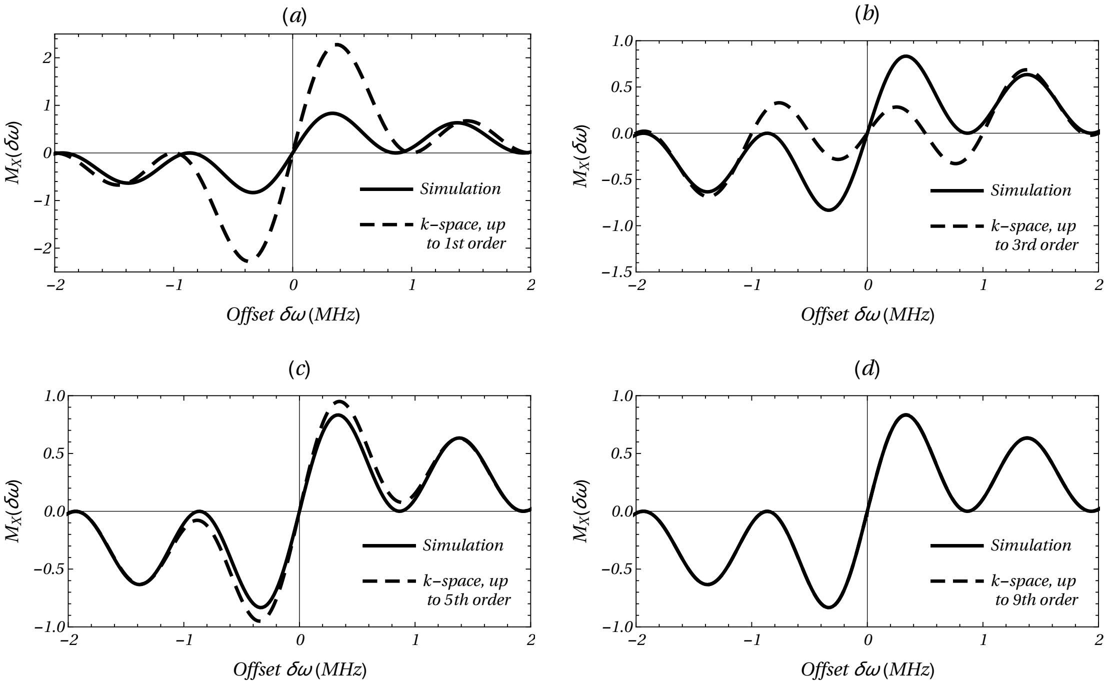

Figure 3.14: In solid black and common to all subplots, the magnetization $M_X(T;\delta\omega)$, obtained through a full simulation of the Hamiltonian dynamics for a pulse $\mathbf{p}(t) = (p_X(t), p_Y(t), p_Z(t)) = (\omega_1, 0, 0)$, of length $T = 1$ μs and $\omega_1 = 0.5$ MHz. In dashed black, $M_{trans}^{\kappa_{cutoff}}(t;\delta\omega)$ for $\kappa_{cutoff} = 1$ in (a), $\kappa_{cutoff} = 3$ in (b), $\kappa_{cutoff} = 5$ in (c) and $\kappa_{cutoff} = 9$ in (d).

3.7 Volterra series

It will not be astonishing for the reader that the results derived in the previous section match the non-linear response theory as developed by Kubo [15–17], in close analog to the classical non-linear theory or Volterra series.

The first step is to introduce the Liouville-von Neumann equation

$$\dot{\rho} = -i[H(t), \rho], \tag{3.52}$$

with

$$H(t) = H_0 + \Delta\omega(t)B + \omega_1(t)A, \tag{3.53}$$

where H_0 is an internal Hamiltonian that commutes with B and ρ_0, ($[B, H_0] = 0$ and $[\rho_0, H_0] = 0$), $\omega_1(t)$ and $\Delta\omega(t)$ are two input pulses, and A and B two operators that do not commute with each other. If we write A in the rotating frame of $H_0 + \Delta\omega(t)B$,

$$A(t) = \exp\left\{ i\int_0^t H_0 + \Delta\omega(\tau)B\ d\tau \right\} A\ \exp\left\{ -i\int_0^t H_0 + \Delta\omega(\tau)B\ d\tau \right\} \tag{3.54}$$

The response $\langle O\rangle(t)$ can then be expressed as

$$\begin{aligned}\langle O\rangle(t) &= \mathrm{Tr}\left(\rho(t)\mathcal{O}\right) = \mathrm{Tr}\left(\rho_0\mathcal{O}\right) + \\ &+ \sum_{k=1}^{\infty}(-i)^k\int_0^t\int_{t_1}^t\ldots\int_{t_{k-1}}^t \omega_1(t_1)\ldots\omega_1(t_k)\,\mathrm{Tr}\left([A(t_1), [A(t_2), [\ldots[A(t_k), \rho_0]\ldots]]]\mathcal{O}\right)dt_k\ldots dt_1\end{aligned} \tag{3.55}$$

If $H_0 = \frac{1}{2}\delta\omega\sigma_Z$, $B = \frac{1}{2}\sigma_Z$, $A = \frac{1}{2}\sigma_X$ and $\mathcal{O} = \frac{1}{2}\sigma_X + i\frac{1}{2}\sigma_Y$, then,

$$\begin{aligned}\langle O\rangle(t) &= \mathrm{Tr}\left(\rho_0\mathcal{O}\right) + \\ &+ \sum_{k=1}^{\infty}(-i)^k\int_0^t\int_{t_1}^t\ldots\int_{t_{k-1}}^t \omega_1(t_1)\ldots\omega_1(t_k)\cos\left(\sum_{j=1}^{\frac{k-1}{2}}\left(\phi(t_{2j}) - \phi(t_{2j-1})\right)\right)e^{i(\phi(t)-\phi(t_k))}dt_k\ldots dt_1\end{aligned} \tag{3.56}$$

which is exactly the same series as the one derived through k-space theory in 3.50.

3.8 Conclusions

In this chapter we presented three sets of coupled recursive formulas for the uncorrelated initial states $\rho_0 = \sigma_X,\ \sigma_Y$, and σ_Z relating the set of coefficients $\{A_m^{n-1}(\delta\omega)\}$ and

$\{A^{n-1}_{z,m}(\delta\omega)\}$ with $\{A^{n}_{m}(\delta\omega)\}$ and $\{A^{n}_{z,m}(\delta\omega)\}$. The sum of the coefficients $A^{n}_{m}(\delta\omega)$ and $A^{n}_{z,m}(\delta\omega)$ fully characterizes the $\delta\omega$-dependent magnetization after applying n soft pulses back to back. Given that computing the coefficients after n pulses requires knowledge of all previous coefficients $\{A^{i}_{m}(\delta\omega)\}_{i=0}^{n-1}$ and $\{A^{i}_{z,m}(\delta\omega)\}_{i=0}^{n-1}$, it automatically implies that we have a complete and analytical map describing the $\delta\omega$-dependent magnetization at any point in time.

We verified that this formalism can also be used to analyze the evolution of magnetization under the action of continuous pulses. To do so, either we time-slice them and assume each individual slice t_p to be small enough, or formally compute the limit of t_p approaching to zero. The result of taking such a limit is a rederivation of an infinite sum of terms describing the non-linear response of the system to an external perturbation $\mathbf{p}(t)$.

Chapter 4

Conclusions

In Chapter 2 we have shown through numerical simulations how to, in principle, overcome several obstacles limiting the use of superconducting high-Q resonators to improve the sensitivity of pulsed ESR.

In particular, the addition of z-control allowed us to work around the bandwidth limitation introduced by the high Q factor of the resonator. The simulation of a Hahn echo experiment simultaneous to z-field sweeps during the excitation, refocusing and formation of the chirped echo, gave solid proof that the proposed pulse sequence would yield the desired results.

To further support our argument, we reproduced the reconstruction procedure of the spectra experimentally, using a broadband NMR setup. Despite the inherent differences between a broadband NMR system and a superconducting high-Q resonator, the NMR experiment provided the first proof-of-principle test.

In Chapter 3 we expanded the k-space formalism to describe multipulse sequences of soft pulses applied around any axis $\hat{x}$, $\hat{y}$ or $\hat{z}$, and acting on a k-space grating generated by a variety of inhomogeneous effects.

The three sets of coupled recursive formulas summarize the effect soft pulses have on the grating, yielding a complete and analytical mapping of the $\delta\omega$-dependent magnetization at any point in time. Moreover, an order analysis of the k-space grating and its paths in the reciprocal space enabled us to rederive non-linear response theory, an infinite sum of magnetization terms also known as Volterra series or Kubo's formula [15–17].

4.1 Future Work

The next step regarding the work of Chapter 2 is to implement the proposed control sequence in a high-Q ESR platform, for which these pulses where initially devised. There is a clear one-to-one correspondence with the ESR simulations, since we have used parameters which are experimentally motivated.

There is also some theoretical aspects that need to be given some more thought. In particular, how reducing the length of the pulse sequence affects the pulse reconstruction. We have noticed that reducing the length of the control pulses translates into a distortion in the reconstructed spectrum, which we believe is related to the adiabatic factor of the sweep. However, not enough work has been done in that direction to properly support such a statement. An in-depth analysis of the relation between pulse length and the adiabatic factor would hopefully inform us how to further decrease the overall length of the pulse sequence, hence enabling us to implement it for samples with smaller relaxation constants T_2.

In Chapter 3, the sets of coupled recursive formulas were derived for an uncorrelated initial state (in other words, independent of the variable $\delta\omega$). It is possible to derive similar formulas for correlated initial states, in particular for $\sin(\delta\omega)\rho_0$ and $\cos(\delta\omega)\rho_0$. In turn, that would automatically provide us with a map for any correlated initial state $f(\delta\omega)\rho_0$ that could be written as a Fourier series of $\sin(\delta\omega)\rho_0$ and $\cos(\delta\omega)\rho_0$.

More interesting, though, would be to tackle the inverse problem described in Chapter 3. Instead of focusing on how a pulse sequence $\mathbf{p}(t)$ yields the magnetization state $\mathbf{M}(T;\delta\omega)$ at a time T, we could ask what pulse sequence $\mathbf{p}(t)$ yields a particular target state $\mathbf{M}_{target}(T;\delta\omega)$. This could be done numerically in the lines of the GRAPE algorithm [34], or in other ways that we have not yet explored. Certainly, other optimization problems exploiting the intrinsic correspondence of this formalism with an easy and visual reciprocal description could be posed, which we believe would constitute a much more interesting approach than simply attempting a redo of an already existing (and very efficient) algorithm.

References

[1] I. I. Rabi, J. R. Zacharias, S. Millman, and P. Kusch. A New Method of Measuring Nuclear Magnetic Moment. *Physical Review*, 53(4):318–318, feb 1938.

[2] A. Abragam. *The principles of nuclear magnetism.* International series of monographs on physics. Clarendon Press, 1983.

[3] E.M. Fortunato, M.A. Pravia, N. Boulant, G. Teklemariam, T.F. Havel, and D.G. Cory. Design of strongly modulating pulses to implement precise effective Hamiltonians for quantum information processing. *The Journal of Chemical Physics*, 116(17):7599–7606, may 2002.

[4] T.W. Borneman, M.D. Hürlimann, and D.G. Cory. Application of optimal control to CPMG refocusing pulse design. *Journal of Magnetic Resonance*, 207(2):220–233, dec 2010.

[5] N. Boulant, J. Emerson, T.F. Havel, D.G. Cory, and S. Furuta. Incoherent noise and quantum information processing. *The Journal of Chemical Physics*, 121(7):2955–2961, aug 2004.

[6] M. Mehring. *Principles of High Resolution NMR in Solids.* Springer Berlin Heidelberg, 2012.

[7] E.M. Haacke, R.W. Brown, M.R. Thompson, and R. Venkatesan. *Magnetic Resonance Imaging: Physical Principles and Sequence Design.* Wiley, 1999.

[8] O.W.B. Benningshof, H.R. Mohebbi, I.A.J. Taminiau, G.X. Miao, and D.G. Cory. Superconducting microstrip resonator for pulsed ESR of thin films. *Journal of Magnetic Resonance*, 230:84–87, may 2013.

[9] A. Bienfait, J. J. Pla, Y. Kubo, M. Stern, X. Zhou, C. C. Lo, C. D. Weis, T. Schenkel, M. L. W. Thewalt, D. Vion, D. Esteve, B. Julsgaard, K. Mølmer, J. J. L. Morton,

and P. Bertet. Reaching the quantum limit of sensitivity in electron spin resonance. *Nature Nanotechnology*, 11(3):253–257, mar 2016.

[10] T.W. Borneman and D.G. Cory. Bandwidth-limited control and ringdown suppression in high-Q resonators. *Journal of Magnetic Resonance*, 225:120–129, dec 2012.

[11] S. Probst, V. Ranjan, Q. Ansel, R. Heeres, B. Albanese, E. Albertinale, D. Vion, D. Esteve, S.J. Glaser, D. Sugny, and P. Bertet. Shaped pulses for transient compensation in quantum-limited electron spin resonance spectroscopy. *Journal of Magnetic Resonance*, 303:42–47, jun 2019.

[12] P. Mansfield and P. K. Grannell. Diffraction and microscopy in solids and liquids by nmr. *Phys. Rev. B*, 12:3618–3634, nov 1975.

[13] J. Hennig. Multiecho imaging sequences with low refocusing flip angles. *Journal of Magnetic Resonance (1969)*, 78(3):397–407, jul 1988.

[14] A. Sodickson and D.G. Cory. A generalized k-space formalism for treating the spatial aspects of a variety of NMR experiments. *Progress in Nuclear Magnetic Resonance Spectroscopy*, 33(2):77–108, aug 1998.

[15] R. Kubo and K. Tomita. A General Theory of Magnetic Resonance Absorption. *Journal of the Physical Society of Japan*, 9(6):888–919, nov 1954.

[16] R. Kubo. Statistical-Mechanical Theory of Irreversible Processes. I. General Theory and Simple Applications to Magnetic and Conduction Problems. *Journal of the Physical Society of Japan*, 12(6):570–586, jun 1957.

[17] R.R. Ernst, G. Bodenhausen, and A. Wokaun. *Principles of Nuclear Magnetic Resonance in One and Two Dimensions*. International series of monographs on chemistry. Clarendon Press, 1987.

[18] C.P. Slichter. *Principles of Magnetic Resonance*. Springer Series in Solid-State Sciences. Springer Berlin Heidelberg, 2013.

[19] N. Bloembergen and R. V. Pound. Radiation Damping in Magnetic Resonance Experiments. *Physical Review*, 95(1):8–12, jul 1954.

[20] C. Wood, I. Hincks, and C. Granade. Quantumutils for mathematica.

[21] E. L. Hahn. Spin Echoes. *Physical Review*, 80(4):580–594, nov 1950.

[22] J.A. Weil, J.R. Bolton, and J.E. Wertz. *Electron Paramagnetic Resonance: Elementary Theory and Practical Applications.* Wiley, 1994.

[23] T. W. Borneman, C. E. Granade, and D. G. Cory. Parallel Information Transfer in a Multinode Quantum Information Processor. *Physical Review Letters*, 108(14):140502, apr 2012.

[24] Yingjie Zhang, Colm A. Ryan, Raymond Laflamme, and Jonathan Baugh. Coherent Control of Two Nuclear Spins Using the Anisotropic Hyperfine Interaction. *Physical Review Letters*, 107(17):170503, oct 2011.

[25] J. S. Hodges, J. C. Yang, C. Ramanathan, and D. G. Cory. Universal control of nuclear spins via anisotropic hyperfine interactions. *Physical Review A*, 78(1):010303, jul 2008.

[26] A. Schweiger and G. Jeschke. *Principles of pulse electron paramagnetic resonance.* Oxford University Press, 2001.

[27] H. Malissa, D. I. Schuster, A. M. Tyryshkin, A. A. Houck, and S. A. Lyon. Superconducting coplanar waveguide resonators for low temperature pulsed electron spin resonance spectroscopy. *Review of Scientific Instruments*, 84(2):025116, feb 2013.

[28] A. J. Sigillito, H. Malissa, A. M. Tyryshkin, H. Riemann, N. V. Abrosimov, P. Becker, H.-J. Pohl, M. L. W. Thewalt, K. M. Itoh, J. J. L. Morton, A. A. Houck, D. I. Schuster, and S. A. Lyon. Fast, low-power manipulation of spin ensembles in superconducting microresonators. *Applied Physics Letters*, 104(22):222407, jun 2014.

[29] M. Mehring and J. S. Waugh. Phase Transients in Pulsed NMR Spectrometers. *Review of Scientific Instruments*, 43(4):649–653, apr 1972.

[30] K. Takeda, Y. Tabuchi, M. Negoro, and M. Kitagawa. Active compensation of rf-pulse transients. *Journal of Magnetic Resonance*, 197(2):242–244, apr 2009.

[31] F. Motzoi, J. M. Gambetta, S. T. Merkel, and F. K. Wilhelm. Optimal control methods for rapidly time-varying Hamiltonians. *Physical Review A*, 84(2):022307, aug 2011.

[32] P.E. Spindler, Y. Zhang, B. Endeward, N. Gershernzon, T.E. Skinner, S.J. Glaser, and T.F. Prisner. Shaped optimal control pulses for increased excitation bandwidth in EPR. *Journal of Magnetic Resonance*, 218:49–58, may 2012.

[33] I.N. Hincks, C.E. Granade, T.W. Borneman, and D.G. Cory. Controlling Quantum Devices with Nonlinear Hardware. *Physical Review Applied*, 4(2):024012, aug 2015.

[34] N. Khaneja, T. Reiss, C. Kehlet, T. Schulte-Herbrüggen, and S.J. Glaser. Optimal control of coupled spin dynamics: design of NMR pulse sequences by gradient ascent algorithms. *Journal of Magnetic Resonance*, 172(2):296–305, feb 2005.

[35] J.M. Böhlen, M. Rey, and G. Bodenhausen. Refocusing with chirped pulses for broadband excitation without phase dispersion. *Journal of Magnetic Resonance (1969)*, 84(1):191–197, aug 1989.

[36] J.M. Böhlen, I. Burghardt, M. Rey, and G. Bodenhausen. Frequency-modulated "Chirp" pulses for broadband inversion recovery in magnetic resonance. *Journal of Magnetic Resonance (1969)*, 90(1):183–191, oct 1990.

[37] J.M. Böhlen and G. Bodenhausen. Experimental Aspects of Chirp NMR Spectroscopy. *Journal of Magnetic Resonance, Series A*, 102(3):293–301, may 1993.

[38] M. Pannier, S. Veit, A. Godt, G. Jeschke, and H.W. Spiess. Dead-Time Free Measurement of Dipole–Dipole Interactions between Electron Spins. *Journal of Magnetic Resonance*, 142(2):331–340, feb 2000.

[39] C. Negrevergne, T.S. Mahesh, C.A. Ryan, M. Ditty, F. Cyr-Racine, W. Power, N. Boulant, T. Havel, D.G. Cory, and R. Laflamme. Benchmarking Quantum Control Methods on a 12-Qubit System. *Physical Review Letters*, 96(17):170501, may 2006.

[40] D.B. Twieg. The <i>k</i> -trajectory formulation of the NMR imaging process with applications in analysis and synthesis of imaging methods. *Medical Physics*, 10(5):610–621, sep 1983.

Appendix A

Mathematical definitions

A.1 Time-ordered exponential

For two operators $H(t_1)$ and $H(t_2)$ such that,

$$\mathcal{T}\Big\{H(t_1)H(t_2)\Big\} = \begin{cases} H(t_1)H(t_2), & \text{if } \ t_1 > t_2 \\ H(t_2)H(t_1), & \text{if } \ t_1 < t_2, \end{cases} \tag{A.1}$$

a mathematical operation known as ordered exponential can be defined. Namely,

$$\begin{aligned} \mathrm{OE}[H](t) = \mathcal{T}\{e^{-i\int_0^t H(\tau)d\tau}\} &= \sum_{n=0}^{\infty} \frac{1}{n!} \int_0^t \int_0^t \dots \int_0^t \mathcal{T}\{H(t'_1)\dots H(t'_n)\}\ \mathrm{d}t'_1 \dots \mathrm{d}t'_n = \\ &= \sum_{n=0}^{\infty} \int_0^t \int_0^{t'_n} \int_0^{t'_{n-1}} ots \int_0^{t'_2} H(t'_n)\dots H(t'_1)\ \mathrm{d}t'_1 \dots \mathrm{d}t'_{n-2}\mathrm{d}t'_{n-1}\mathrm{d}t'_n, \end{aligned} \tag{A.2}$$

where the term $n = 0$ equates to the identity $\mathbb{1}$. We can also perform a time discretization to redefine A.2 as an ordered product of n exponentials in the limit of n tending to infinity. Namely,

$$\mathrm{OE}[H](t) = \lim_{n\to\infty} \left(e^{-iH(t_n)\Delta t} e^{-iH(t_{n-1})\Delta t} \dots\ e^{-iH(t_0)\Delta t} \right) = \lim_{n\to\infty} \left(\prod_{m=n}^{0} e^{-iH(t_m)\Delta t} \right), \tag{A.3}$$

where $t_i \equiv i\Delta t$, and $\Delta t \equiv t/N$.

A.2 The dynamics of an ensemble of non-interacting spin-1/2 particles

A.2.1 Factorization of the time evolution operator into tensor products

By employing the definition of ordered exponential stated in equation A.3, the Hamiltonian introduced in section 1.1, as well as identities

$$e^{A\oplus B} = e^{A}\otimes e^{B}, \tag{A.4}$$

and

$$(A\otimes B)(C\otimes D) = AC\otimes BD, \tag{A.5}$$

we can show that

$$\begin{aligned} U_T(t) &= \mathcal{T}\left\{e^{-i\int_0^t H_T(\tau)d\tau}\right\} \overset{A.3}{=} \mathrm{OE}[H_T](t) = \lim_{n\to\infty}\left(\prod_{m=n}^{0} e^{-iH_T(t_m)\Delta t}\right) \overset{1.1}{=} \\ &= \lim_{n\to\infty}\left(\prod_{m=n}^{0} e^{-i\bigoplus_{k=1}^{N} H_k(t_m)\Delta t}\right) \overset{A.4}{=} \lim_{n\to\infty}\left(\prod_{m=n}^{0}\left(\bigotimes_{k=1}^{N} e^{-iH_k(t_m)\Delta t}\right)\right) \overset{A.5}{=} \\ &= \bigotimes_{k=1}^{N}\left(\lim_{n\to\infty}\left(\prod_{m=n}^{0} e^{-iH_k(t_m)\Delta t}\right)\right) = \bigotimes_{k=1}^{N}\mathcal{T}\left\{e^{-i\int_0^t H_k(\tau)d\tau}\right\} = \bigotimes_{k=1}^{N} U_k(t) \end{aligned} \tag{A.6}$$

where $U_k(t) \equiv \mathcal{T}\left\{e^{-i\int_0^t H_k(\tau)d\tau}\right\}$.

A.2.2 Factorization of the state into tensor products

It trivially follows from A.6 and 1.2 that

$$\rho_T(t) = U_T(t)\rho_T(0)U_T^{\dagger}(t) = \left(\bigotimes_{k=1}^{N} U_k(t)\right)\rho_0^{\otimes N}\left(\bigotimes_{k=1}^{N} U_k^{\dagger}(t)\right) \overset{A.5}{=} \bigotimes_{k=1}^{N} U_k(t)\rho_0 U_k^{\dagger}(t) = \bigotimes_{k=1}^{N} \rho_k(t). \tag{A.7}$$

A.2.3 Expected values of observables

It follows from the definition of NMR observables in 1.8 and from the previously derived expression A.7, that the expectation values for $\mathcal{S}_X$, $\mathcal{S}_Y$ and $\mathcal{S}_Z$ can be written in the form

$$
\begin{aligned}
\langle \mathcal{S}_i \rangle(t) &= \mathrm{Tr}\left[\rho_T(t)\mathcal{S}_i\right] \overset{1.8}{\underset{A.7}{=}} \mathrm{Tr}\left[\sum_{k=1}^{N} \rho_k(t)^{\otimes(k-1)} \otimes \rho_k(t) S_i \otimes \rho_k(t)^{\otimes(N-k)}\right] = \\
&= \sum_{k=1}^{N} \left(\prod_{j=1}^{k-1} \mathrm{Tr}\left[\rho_j(t)\right]\right) \mathrm{Tr}\left[\rho_k(t) S_i\right] \left(\prod_{j=k}^{N} \mathrm{Tr}\left[\rho_j(t)\right]\right) \overset{\mathrm{Tr}(\rho)=1}{=} \\
&= \sum_{k=1}^{N} \mathrm{Tr}\left[\rho_k(t) S_i\right] = \sum_{k=1}^{N} \langle S_i \rangle_k(t),
\end{aligned}
\tag{A.8}
$$

where we used elemental properties of the Kronecker product and the trace.

A.3 Rotating Wave Approximation

Let $H(t)$ be the total Hamiltonian that describes the system dynamics. The state of the system is characterized by a density operator $\rho(t)$ and its time evolution obeys the Liouville-Von Neuman equation of motion (if we assume no interaction with the environment). Namely,

$$\dot{\rho}(t) = -i\big[H(t), \rho(t)\big], \tag{A.9}$$

whose formal solution is written as

$$\rho(t) = U(t)\rho(0)U^{\dagger}(t), \tag{A.10}$$

where

$$U(t) = \mathcal{T}\Big\{e^{-i\int_0^t H(\tau)d\tau}\Big\}. \tag{A.11}$$

Let us denote the sum of the Hamiltonians introduced in 1.17 and 1.18 as the lab frame Hamiltonian for a spin-1/2,

$$H_L(t) = H_0 + H_{contr} = \frac{1}{2}\,\omega_0\ \sigma_Z + \frac{1}{2}\ 2\omega_1(t)\cos\left(\omega_t t + \phi\right)\ \sigma_X \tag{A.12}$$

and the state of the system in that frame as $\rho_L(t)$. The transformation to the rotating frame of ω_t is given by

$$\rho_L(t) = e^{-iH_t t}\rho_R(t)e^{iH_t t} \tag{A.13}$$

where

$$H_t = \frac{1}{2}\omega_t\sigma_Z \tag{A.14}$$

Let us now find how the Von-Neumann equation in the lab frame

$$\dot{\rho}_L(t) = -i[H_L(t), \rho_L(t)] \tag{A.15}$$

relates to the rotating frame of ω_t. To do so, let us substitute the equation in A.13 into A.15,

$$\frac{d}{dt}\Big(e^{-iH_t t}\rho_R(t)e^{iH_t t}\Big) = -i[H_L(t)\ ,\ e^{-iH_t t}\rho_R(t)e^{iH_t t}]. \tag{A.16}$$

The time derivative can be expanded into three terms,

$$\frac{d}{dt}\Big(e^{-iH_t t}\rho_R(t)e^{iH_t t}\Big) = -iH_t e^{-iH_t t}\rho_R(t)e^{iH_t t} + e^{-iH_t t}\dot{\rho}_R(t)e^{iH_t t} + e^{-iH_t t}\rho_R(t)\ iH_t e^{iH_t t} \tag{A.17}$$

and the right hand side of A.16 is, of course,

$$-i[H_L(t)\ ,\ e^{-iH_t t}\rho_R(t)e^{iH_t t}] = -i\ H_L(t)\ e^{-iH_t t}\rho_R(t)e^{iH_t t} + i\ e^{-iH_t t}\rho_R(t)e^{iH_t t}\ H_L(t). \tag{A.18}$$

Then, by substituting the expanded terms into A.16 and rearranging them, we retrieve

$$\dot{\rho}_R(t) = -i\ [e^{iH_t t}H_L(t)e^{-iH_t t} - H_0\ ,\ \rho_R(t)] \tag{A.19}$$

where the Hamiltonian in the rotating frame then is,

$$H_R(t) = e^{iH_t t}H_L(t)e^{-iH_t t} - H_t \tag{A.20}$$

The last step is to perform a Rotating Wave Approximation to the term

$$e^{iH_t t}H_L(t)e^{-iH_t t} \tag{A.21}$$

in A.20. Since $H_t = \frac{1}{2}\omega_t\sigma_Z$, its exponential commutes with the Zeeman term H_0. It does not commute, however, with the σ_X and σ_Y terms of the control Hamiltonian. In particular, due to Pauli commutation relations,

$$e^{i\frac{1}{2}\omega_t t\ \sigma_Z}\ \sigma_X\ e^{-i\frac{1}{2}\omega_t t\ \sigma_Z} = \cos{(\omega_t t)}\sigma_X - \sin{(\omega_t t)}\sigma_Y \tag{A.22}$$

$$e^{i\frac{1}{2}\omega_t t\ \sigma_Z}\ \sigma_Y\ e^{-i\frac{1}{2}\omega_t t\ \sigma_Z} = \cos{(\omega_t t)}\sigma_Y + \sin{(\omega_t t)}\sigma_X \tag{A.23}$$

If we then multiply A.22 by $\cos{(\omega_t t + \phi)}$, we retrieve

$$\begin{aligned}\cos{(\omega_t t + \phi)}e^{i\frac{1}{2}\omega_t t\ \sigma_Z}\ \sigma_X\ e^{-i\frac{1}{2}\omega_t t\ \sigma_Z} &= \frac{1+\cos 2\omega_t t}{2}\cos\phi\ \sigma_X - \frac{\sin 2\omega_t t}{2}\sin\phi\ \sigma_X + \\ -\frac{\sin 2\omega_t t}{2}\cos\phi\ \sigma_Y + \frac{1-\cos 2\omega_t t}{2}\sin\phi\ \sigma_Y &\overset{rwa}{=} \frac{1}{2}\cos\phi\ \sigma_X + \frac{1}{2}\sin\phi\ \sigma_Y\end{aligned} \tag{A.24}$$

where in the last step we have gotten rid of higher order frequency terms.

Therefore, the Hamiltonian after performing the Rotating Wave Approximation (RWA) becomes,

$$H_R(t) = \frac{1}{2}\delta\omega + \frac{1}{2}\omega_1(t)\cos\phi\ \sigma_X + \frac{1}{2}\omega_1(t)\sin\phi\ \sigma_Y \tag{A.25}$$

where $\delta\omega = \omega_0 - \omega_t$. The RWA is a good approximation when $\omega_1 \ll \omega_0$ and $|\delta\omega| \ll \omega_0$, a regime where most ESR and NMR experiments are performed.

Appendix B

Code

Relevant code for this thesis can be found at `https://github.com/jabamoros/ThesisSimulations`, and the software library QuantumUtils [20] used in the simulations is available at `https://github.com/QuantumUtils/quantum-utils-mathematica`.